UC Berkeley
UC Berkeley Previously Published Works

Title

Blueprint for a High-Performance Fluxonium Quantum Processor

Permalink

https://escholarship.org/uc/item/02q5c0px

Journal

PRX Quantum, 3(3)

ISSN

2691-3399

Authors

Nguyen, LB
Koolstra, G
Kim, Y
et al.

Publication Date

2022-07-01

DOI

10.1103/PRXQuantum.3.037001

Peer reviewed

Roadmap

Blueprint for a High-Performance Fluxonium Quantum Processor

Long B. Nguyen[1,2,*] Gerwin Koolstra,[1,2] Yosep Kim,[1,2,‡] Alexis Morvan,[1,2,§] Trevor Chistolini,[2]
Shraddha Singh,[3,4] Konstantin N. Nesterov,[5] Christian Jünger,[1,2] Larry Chen,[2] Zahra Pedramrazi,[1,2]
Bradley K. Mitchell,[1,2] John Mark Kreikebaum,[2,6] Shruti Puri,[3,4] David I. Santiago,[1,2] and
Irfan Siddiqi[1,2,6,†]

[1] *Computational Research Division, Lawrence Berkeley National Laboratory, Berkeley, California 94720, USA*
[2] *Department of Physics, University of California, Berkeley, California 94720, USA*
[3] *Department of Applied Physics, Yale University, New Haven, Connecticut 06511, USA*
[4] *Yale Quantum Institute, Yale University, New Haven, Connecticut 06511, USA*
[5] *Bleximo Corp., Berkeley, California 94720, USA*
[6] *Materials Science Division, Lawrence Berkeley National Laboratory, Berkeley, California 94720, USA*

Transforming stand-alone qubits into a functional, general-purpose quantum processing unit requires an architecture where many-body quantum entanglement can be generated and controlled in a coherent, modular, and measurable fashion. Electronic circuits promise a well-developed pathway for large-scale integration once a mature library of quantum-compatible elements have been developed. In the domain of superconducting circuits, fluxonium has recently emerged as a promising qubit due to its high-coherence and large anharmonicity, yet its scalability has not been systematically explored. In this work, we present a blueprint for a high-performance fluxonium-based quantum processor that addresses the challenges of frequency crowding, and both quantum and classical crosstalk. The main ingredients of this architecture include high-anharmonicity circuits, multipath couplers to entangle qubits where spurious longitudinal coupling can be nulled, circuit designs that are compatible with multiplexed microwave circuitry, and strongly coupled readout channels that do not require complex, frequency-sculpted elements to maintain coherence. In addition, we explore robust and resource-efficient protocols for quantum logical operations, then perform numerical simulations to validate the expected performance of this proposed processor with respect to gate fidelity, fabrication yield, and logical error suppression. Lastly, we discuss practical considerations to implement the architecture and achieve the anticipated performance.

I. INTRODUCTION

Quantum computation and quantum information processing has opened a new frontier in science and technology, with recent advances validating our understanding of the quantum world and revealing the potential for

* longbnguyen@berkeley.edu
† irfan_siddiqi@berkeley.edu
‡ Current address: Center for Quantum Information, Korea Institute of Science and Technology (KIST), Seoul 02792, Korea.
§ Current address: Google Quantum AI, Mountain View, CA 94043, USA.

novel applications [1–4]. Among various platforms, superconducting qubits has emerged as a promising candidate for the implementation of fault-tolerant universal quantum computing [5], with the power of quantum information processing [6,7] and novel quantum error correction schemes [8–17] having been demonstrated. In addition, quantum simulation [18–26] and optimization algorithms [27,28] have been implemented using noisy intermediate-scale quantum (NISQ) devices [29].

Despite recent mitigation techniques [30,31], approaching large-scale universal quantum computation requires further suppression of errors resulting from control imprecision and decoherence due to unwanted interaction with the noisy environment [29,32,33]. The theory of quantum error correction (QEC) provides a promising path to reach this goal [34–37]. The essence of the QEC strategy is to encode quantum information in nonlocal entangled states such that local errors cannot corrupt it [38]. According to the threshold theorem, when the system is operated with

errors below the *accuracy threshold*, an arbitrarily good protection against decoherence can be achieved [39–41]. In practice, the requirement to encode *logical qubits* using a redundant number of *physical qubits* imposes a large resource overhead that is challenging to achieve. Besides decoherence of physical qubits, crosstalk [42], frequency crowding [43,44], and leakage out of the computational subspace [45,46] are also the central problems to overcome upon scaling up. For example, the most popular QEC code for planar architecture, the surface code [32,47–50], has an accuracy threshold of approximately 1% and requires only nearest-neighbor interactions, yet only small-distance codes have been recently explored in superconducting circuit architectures based on transmon devices [13–17].

One promising superconducting qubit in the quest toward constructing a fault-tolerant quantum computer is fluxonium [51], due to its long coherence times and high anharmonicity. The circuit consists of three elements in parallel: a capacitor, a Josephson junction, and a superinductor. The inductive shunt eliminates the qubit's offset charge [52], and the large inductance value suppresses its sensitivity to flux noise. Fluxonium can be tuned *in situ* by threading an external magnetic flux through the circuit loop. When this flux bias is at a value equal to half-integer flux quantum, the $|0\rangle \rightarrow |1\rangle$ transition has low frequency, with $\omega_{01}/2\pi$ typically below 1 GHz, which helps reduce the effect from dielectric loss, enhancing the relaxation time T_1. At the same time, the circuit also becomes first-order insensitive to flux noise, resulting in a long coherence time T_2 primarily limited by T_1 for nominally fast dispersive readout. This operating regime is thereby referred to as the *high-coherence regime* [53], with T_2 consistently in the range of a few hundred microseconds in both three-dimensional (3D) [53] and planar [54] experiments. Recent advances in fabrication and cryogenic shielding have elevated the relaxation time T_1 and subsequently the coherence time T_2 to over a millisecond in a 3D device [55].

In addition, fluxonium's large anharmonicity can be exploited to operate high-fidelity single-qubit operations, with a microwave control error of approximately 10^{-4} using an 80-ns-long pulse [55], and fast flux control error of approximately 10^{-3} using a 20-ns-long pulse [54]. High readout fidelity with an error of approximately 10^{-2} using over a hundred of resonator photons has been demonstrated [56,57], while qubit reset with an error of approximately 3×10^{-2} using microwave [54] or approximately 10^{-2} using active feedback [56,58] have been realized. The first experimental implementations of two-qubit gates were based on the interaction between $|1\rangle \rightarrow |2\rangle$ transitions of two capacitively coupled fluxoniums housed in a 3D copper cavity [59,60], where a controlled-phase gate is induced by a microwave pulse applied near these transitions [61]. The resulting gate fidelity is as high as 0.992,

limited by the coherence times of the participating noncomputational states, which are unprotected. In another scheme, an iSWAP gate [62] between two planar capacitively coupled fluxoniums was realized by tuning their computational transitions to be on resonant using fast flux, with corresponding gate fidelity as high as 0.997 [63]. The performance of this gate scheme is intrinsically limited by the lower coherence times away from the flux sweet spot, and its operation may involve additional complications such as spectator errors in large-scale devices. Recently, an fSim gate family was also proposed [64] and implemented [65] using an additional fluxonium as a tunable coupling element, resulting in a gate fidelity as high as 0.9955. This approach comes at the cost of increased design and operational complexity, especially in large-scale devices, whereas the data qubits are essentially fixed frequency. Currently, there is no clear roadmap to construct a fluxonium-based quantum processor with projected performance to surpass state-of-the-art architectures. Combined with the misconception that it is challenging to manipulate and readout low-frequency qubit transitions, and the fear of uncontrollable variability of junction parameters in a multicomponent qubit, this leads to relatively sparse efforts in scaling up the platform.

In this work, we provide the blueprint for a scalable high-performance quantum architecture based on fluxonium qubits. We show that, in principle, this platform will have suppressed crosstalk, reduced design complexity, improved operational efficiency, high-fidelity gates, and resistance to parameter fluctuations. In contrast to previous works, our analysis focuses on scalability, and thus involves a wide range of practical qubit parameters. Interestingly, the envisioned quantum processor has the potential to out scale and out perform its contemporary counterparts even with relatively modest average coherence times, thanks to the qubit's large anharmonicity and favorable selection rules.

First, we discuss the important properties of the qubit on which we develop and explain the proposed parameters as well as our approaches in the rest of the paper. We review the dispersive readout scheme, which involves a coupled fluxonium-resonator system, identifying the advantages in readout multiplexing with fluxoniums, such as a potential reduction of readout crosstalk. In addition, since the qubit frequency is far away from the readout frequency, Purcell filters [66–70] are not required for fast measurements. Then, we show via numerical simulation that single-qubit microwave control can be done in as fast as ten nanoseconds with coherent error below 10^{-6}, with flux driving performing better than charge driving. Together with the lack of Purcell filter requirement, diplexing rf flux control with dc bias will substantially reduce the design complexity of the chip.

The keystone in developing large-scale quantum devices is designing multi-qubit interactions. Since the computational states in fluxonium have long coherence times and high anharmonicity at the fixed half-integer flux quantum bias, the optimal approach is to engineer entangling gates based on the transverse coupling between these states. Meanwhile, it is also important to suppress the spurious static longitudinal ZZ rate, which leads to an always-on entangling operation, and may expand into chip-scale correlated errors [42,71,72]. Here, we propose a multipath coupling scheme, which enables a fast direct exchange interaction rate between the computational states, with $J_{\text{eff}} \sim 10$ MHz, and at the same time negates the static ZZ rate across a wide range of qubit parameters. We numerically demonstrate high-fidelity microwave-activated two-qubit gates based on the cross-resonance [73–76] and differential ac-Stark shift [60,77–79] effects, with coherent gate error as low as 10^{-6}, and consistently below 10^{-2} across the entire range of qubit-qubit detuning. The minimal leakage outside of the computational subspace validates our simple spin-model description. Since these gates involve only high-coherence computational states, gate error due to decoherence is small. Moreover, they can be implemented using the same control lines and microwave electronics for single-qubit gates, improving resource efficiency in scaling up.

Upon advancing to large-scale devices, frequency crowding is a major challenge to overcome. To investigate this problem, we first impose the frequency constraints using our gate simulation results. Then, based on previous studies on Josephson junction nanofabrication, we consider practical frequency dispersion in fluxonium qubits biased at the fixed optimal external flux, and show that the probability of constructing a frequency-collision-free device is close to unity for large-scale chips consisting of over thousands of qubits arranged in a square lattice. In addition, we discuss further error suppression of this platform using the XZZX surface code [80], showing exponential reduction of logical error rate ε_L, with $\varepsilon_L \sim 10^{-7}$ for code distance $d = 11$ and relatively modest average coherence times. Our results also indicate the importance of improving readout and initialization fidelity.

A schematic of the proposed architecture is shown in Fig. 1. The article is structured to explore each component of this platform as follows. We review the important properties of the fluxonium qubit with an emphasis on scalability in Sec. II. In Sec. III, we discuss dispersive measurement of the qubit via an ancilla resonator, reviewing recent results and important considerations upon scaling up. In Sec. IV, we explore single-qubit operations for the proposed range of qubit parameters. We investigate different qubit-qubit coupling schemes in Sec. V, revealing the advantage of the multipath coupling approach. We numerically simulate the cross-resonance controlled-NOT (CNOT) [73–75] and the differential ac-Stark controlled-Z (CZ)
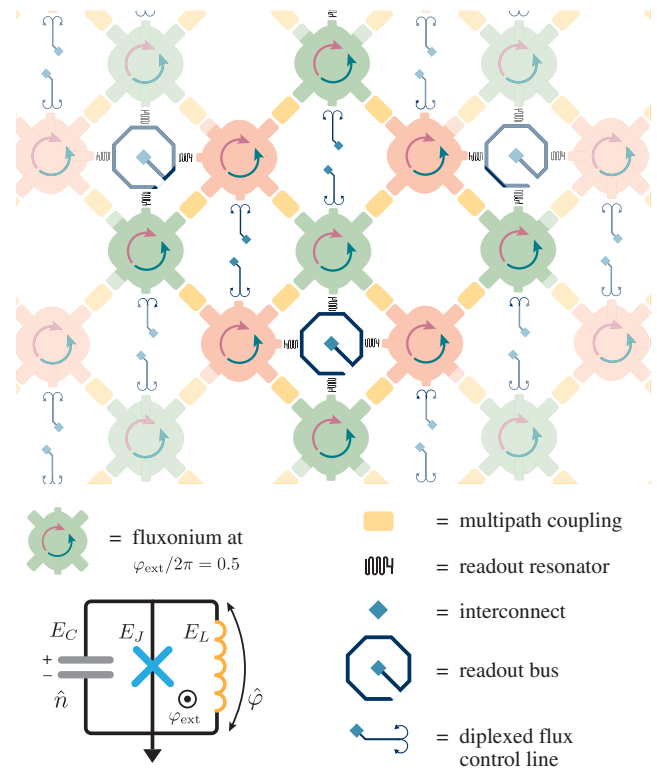

FIG. 1. Blueprint of the proposed fluxonium quantum processor. The qubits are fluxonium circuits biased at half-integer flux quantum, and their lowest eigenstates are symmetric and antisymmetric superpositions of fluxon states corresponding to supercurrents flowing clockwise and anticlockwise in the circuits. The two different colors represent data and ancilla qubits in a surface code lattice. The qubits are readout dispersively via individual coplanar waveguide resonators, four of which are capacitively connected to a common superconducting bus. The diplexed flux lines provide both dc bias and rf controls. These components are connected to electronic instruments via microwave interconnects. The qubit-qubit interaction follows a multipath coupling approach, which allows fast and high-fidelity entangling gates.

[78,79] gates in Sec. VI. After discussing experimentally feasible frequency dispersion of the computational states and relevant frequency allocation constraints, we compute the expected fabrication yield of large-scale devices in Sec. VII. Motivated by these results, we simulate logical error suppression using the XZZX surface code [80] in Sec. VIII. Finally, we provide the roadmap toward constructing a practical fluxonium quantum processor in Sec. IX, and summarize the main ideas of the paper in Sec. X.

II. FLUXONIUM QUBIT

A fluxonium circuit [51] consists of three elements in parallel (Fig. 1, bottom left): a capacitor with charging energy $E_C = e^2/2C$, a Josephson junction with Josephson energy $E_J = I_c\phi_0$, and an inductor with inductive energy

$E_L = \phi_0^2/L$, where we denote I_c as the junction's critical current, and $\phi_0 = \Phi_0/2\pi$ as the reduced flux quantum. Using the irrotational gauge [81,82], the Hamiltonian of the system can be written as

$$\hat{\mathcal{H}}/h = 4E_C\hat{n}^2 - E_J\cos\hat{\varphi} + \frac{1}{2}E_L(\hat{\varphi} + \varphi_{\text{ext}})^2, \quad (1)$$

where $\hat{n}$ is associated with the number of excess Cooper pairs on the capacitive electrodes, and $\hat{\varphi}$ is the superconducting phase twist across the inductor. These two quantum mechanical operators obey the commutation relation $[\hat{\varphi}, \hat{n}] = i$. In the harmonic oscillator basis with creation (annihilation) operator $\hat{b}^\dagger$ ($\hat{b}$), they can be written as

$$\hat{\varphi} = \frac{1}{\sqrt{2}}\left(\frac{8E_C}{E_L}\right)^{1/4}(\hat{b}^\dagger + \hat{b}),$$

$$\hat{n} = \frac{i}{\sqrt{2}}\left(\frac{E_L}{8E_C}\right)^{1/4}(\hat{b}^\dagger - \hat{b}), \quad (2)$$

such that the phase and charge operators resemble the position and momentum operators, respectively. In addition, their relative amplitudes generally depend on the energy ratio E_C/E_L.

We can interpret the Hamiltonian in Eq. (1) as describing the motion of a fictitious particle with kinetic energy proportional to E_C in a potential landscape shaped by E_J and E_L. The potential can be further tuned by applying an external magnetic flux, written in normalized form as $\varphi_{\text{ext}} = 2\pi\Phi_{\text{ext}}/\Phi_0$. For the qubit to be in the fluxonium regime, the energy scales are usually designed to satisfy $2 \leq \{E_J/E_L, E_J/E_C\} \leq 10$. The E_J/E_L ratio determines the number of local wells within the quadratic potential, and the E_J/E_C condition corresponds to the tunneling rate across the wells.

Typically, the inductive energy in fluxonium is $E_L \sim 0.5$ GHz, corresponding to a large inductance of $L \sim 327$ nH. To fulfill this stringent requirement, different strategies have been employed to implement superconducting inductors with impedance surpassing the resistance quantum $R_Q \sim 6.5$ kΩ, commonly referred to as *superinductors*. They are typically constructed based on the phenomenon of kinetic inductance, with experimental realizations including arrays of Josephson junctions [51,83], superconducting nanowires [84–86], or disordered superconductors such as granular aluminum (grAl) [87–90]. Recently, geometric superinductors have also been successfully fabricated and characterized [91,92].

Besides shaping the potential landscape, the superinductor also helps protect the qubit from decoherence. On one hand, the inductive shunt makes the excess charge on the capacitive electrodes continuous [52], nulling the qubit's sensitivity to charge offset. Since fluxonium is inherently insensitive to charge noise, the charging energy E_C may

take arbitrary values, and thus can be used as a flexible tuning knob. On the other hand, the large inductance suppresses the qubit's sensitivity to $1/f$ flux noise [53,93]. Within the scope of this work, we consider the superinductor as an ideal circuit element, assuming that phase slips [83,94,95], cross-Kerr [88], and collective modes effects [96] are negligible.

Circuits with large E_J/E_C ratio are called *heavy fluxonium* [93,97], with the unique property of having long-lived circulating current states called fluxons at certain external fluxes where their wave functions are localized. In this regime, the potential and subsequently the fluxon transition energies are linearly dependent on external flux. Hence, their coherence times T_2 are limited by $1/f$ flux noise to about 5 μs [93], leading to a much higher phase-flip rate compared to bit-flip rate. We thus refer to this regime as *biased-noise*. A fluxonium-biased at half-integer flux quantum values becomes insensitive to flux noise up to first order, and has been shown to have long coherence times [53–55]. We consequently refer to fluxonium qubits operating in this regime to be *high-coherence*.

In this work, we focus on the high-coherence regime with a moderate parameter configuration with $\{E_J, E_C, E_L\} \sim \{4, 1, 1\}$ GHz, which corresponds to a compact qubit that can be reliably fabricated. In addition, these parameters offer key scalability advantages, which we discuss throughout the paper. The transition energy spectrum of the circuit is shown in Fig. 2(a), with transitions from the ground state $|0\rangle$ and first excited state $|1\rangle$ plotted in solid and dashed lines, respectively. Their relative differences indicate the anharmonicity of the system. Energy transitions near $\varphi_{\text{ext}} = 0$ are similar to those of a standard transmon qubit, allowing straightforward device characterization.

When the circuit is biased at the half-integer flux quantum sweet spot $\varphi_{\text{ext}}/2\pi = 0.5$, the two lowest eigenstates correspond to symmetric and antisymmetric superpositions of persistent current states corresponding to supercurrents flowing in the clockwise and counterclockwise directions in the circuit, similar to those found in flux qubits [98–102]. The transition energy is then simply the splitting gap resulting from tunneling of a fictitious particle across the potential barrier, the amplitude of which depends strongly on $\sqrt{E_J/E_C}$ and linearly on E_L [51]. For our proposed circuit parameters, this frequency is $\omega_{01}/2\pi = 0.58$ GHz. Figure 2(b) shows the energy spectrum and wave functions of the first four states at the symmetric flux bias $\varphi_{\text{ext}}/2\pi = 0.5$. Since the quadratic potential well only splits into local ones at sufficiently low frequency, the higher states resemble Fock states in a harmonic oscillator, albeit with high nonlinearity. They are separated from the two lowest states by a large energy gap, with $\omega_{12}/2\pi = 3.39$ GHz. The high anharmonicity helps alleviate state leakage and frequency crowding significantly, as we explore in later sections. Below, we refer to the computational
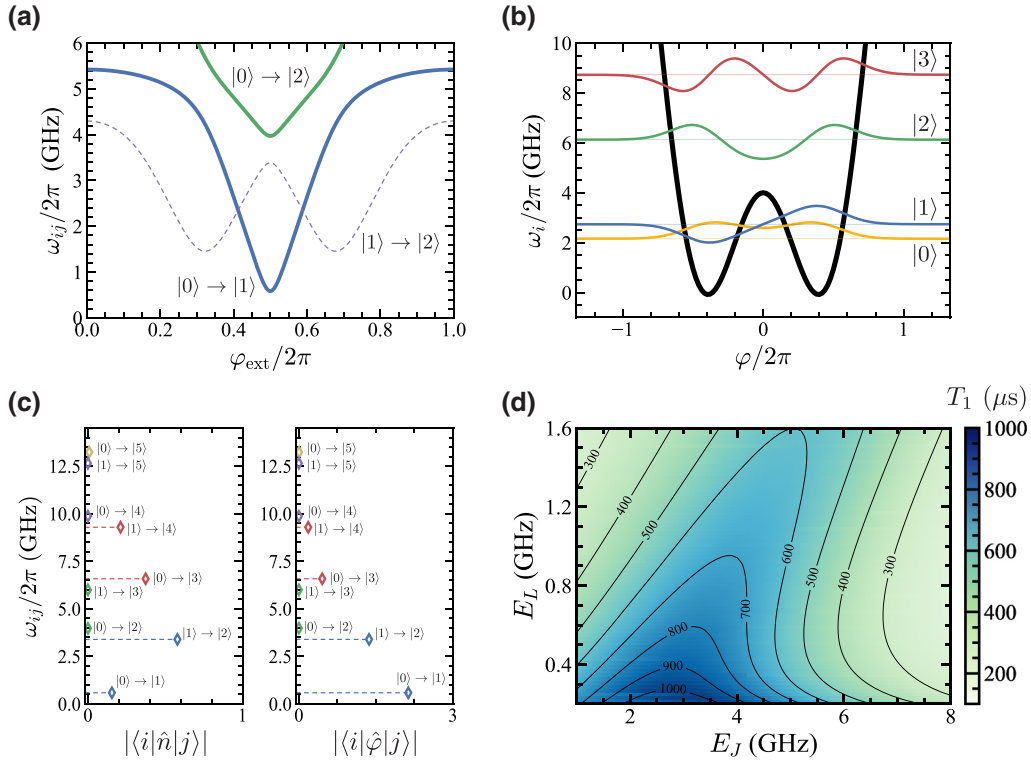
FIG. 2. Fluxonium properties. (a) Transition energy spectrum $\omega_{ij} \equiv \omega_j - \omega_i$ of a fluxonium circuit with $\{E_J, E_C, E_L\} = \{4, 1, 1\}$ GHz. The solid lines are transitions from the ground state $|0\rangle$, and the dashed line is transition $|1\rangle \rightarrow |2\rangle$. (b) Potential well (black) and wave functions in the phase basis corresponding to the first four eigenstates at half-integer flux quantum bias $\varphi_{\text{ext}}/2\pi = 0.5$. (c) Charge and phase matrix elements corresponding to transitions from $|0\rangle$ and $|1\rangle$ at $\varphi_{\text{ext}}/2\pi = 0.5$. The vertical axis shows the corresponding frequencies of these transitions. (d) Estimated energy relaxation times T_1 limited by dielectric loss with loss tangent $\tan\delta_{\text{diel}} = 2 \times 10^{-7}$ at 5 GHz, and quasiparticles in the inductor with normalized density $x_{\text{qp}} = 2 \times 10^{-9}$. The charging energy is $E_C = 1$ GHz.

subspace as the Hilbert space consisting of the $|0\rangle$ and $|1\rangle$ states.

Selection rules in fluxonium can be exploited to engineer novel coupling schemes for quantum information processing purposes. The matrix elements at a half-integer flux quantum bias are shown in Fig. 2(c) and can be summarized as follows. For the computational states, since their wave functions have substantial overlap in the phase basis due to hybridization, the corresponding matrix element $\varphi_{01} \equiv \langle 0|\hat{\varphi}|1\rangle$ is high, while the charge matrix element $n_{01} \equiv \langle 0|\hat{n}|1\rangle$ is substantially smaller. For the noncomputational states, the phase (charge) matrix elements are smaller (larger) than that of the computational states. As a result, charge coupling is preferable if interaction involving higher states is desired, and flux coupling is preferable if interaction involving the computational states is intended. For example, charge coupling was used in the microwave-activated two-qubit controlled-phase gate scheme involving $|1\rangle \rightarrow |2\rangle$ transition [59–61], and flux coupling resulted in strong hybridization of the lowest eigenstates in the fluxonium molecule [103]. In general, charge matrix elements are smaller than phase matrix

elements due to the large inductance in the circuit [$8E_C > E_L$ in Eq. (2)].

While the multilevel aspect of fluxonium can be utilized to engineer novel coupling schemes, certain transitions are forbidden, alleviating spectral crowding problems and suppressing coupling to high-frequency spurious modes. Notably, only transitions with an odd number of excitations are allowed at half-integer flux quantum bias due to parity, $n_{ij} = \varphi_{ij} = 0$ for all $(i + j)_{\text{even}}$. This allows selective coupling to any odd transition without interacting with the nearby even transition. In addition, the high-frequency region of the spectrum resembles that of a harmonic oscillator, so higher-order transitions have vanishing matrix elements. Thus, we can neglect coupling between fluxonium and the surrounding environment beyond 10 GHz.

One of the main challenges in realizing fault-tolerant quantum computation using superconducting qubits is the detrimental effect from nonequilibrium quasiparticles [104], which can be created from photon-assisted processes [105–108] or ionizing radiation sources [109,110]. Once formed, quasiparticles may diffuse to other parts of the device, recombine, or get trapped [111]. They have

been recently found to cause correlated errors in transmon devices [112,113], which will potentially make existing QEC protocols ineffective. The susceptibility of the fluxonium qubit biased at the half-integer flux quantum sweet spot to quasiparticles can be summarized as follows. On one hand, the effect of quasiparticles around the small junction on the $|0\rangle \rightarrow |1\rangle$ transition is suppressed due to destructive interference between electronlike and holelike tunneling events [114–116]. On the other hand, the large phase matrix element φ_{01} leads to strong coupling to quasiparticles in the superinductor, which manifests as inductive loss [117]. In contrast, the $|0\rangle \rightarrow |2\rangle$ transition is sensitive to quasiparticles around the small junction and indifferent to those in the inductors. Thus, it can be included to probe the quasiparticle density in fluxonium circuits [55,118]. Intriguingly, the corresponding quasiparticle density in the inductor was found to be at least an order of magnitude smaller than that around the small junction [55,117].

Considering known decoherence sources, the proposed parameters allow the computational states to have long coherence times. Since the dephasing time T_2 is primarily limited by the relaxation time T_1 here [53–55], we focus on analyzing T_1. To this end, we estimate the energy relaxation time T_1 for fixed charging energy $E_C = 1$ GHz and different E_J, E_L values, using limits imposed by dielectric loss with $\tan \delta_{\text{diel}} = 2 \times 10^{-7}$, corresponding to a transmon with frequency $\omega_{01}/2\pi = 5$ GHz having a relaxation time of 160 μs, and quasiparticles in the inductor with normalized density $x_{\text{qp}} = 2 \times 10^{-9}$, corresponding to a fluxonium qubit with parameters as reported in Ref. [55] having relaxation time $T_1 = 1$ ms at absolute temperature (see Appendix A). The result in Fig. 2(d) shows that while the quality of the surrounding environment may change the absolute T_1 limit, the parameter space around $E_J = 4$ GHz, $E_L = 1$ GHz gives consistently high T_1.

In multi-qubit devices, we propose tuning the qubit frequency by varying the inductive energy E_L from 0.5 to 1.6 GHz, corresponding to qubit frequency $\omega_{01}/2\pi$ in the range [237 − 1163] MHz. As shown in Fig. 2(d), a circuit with E_L varying in this range is expected to have high T_1. We note that although the region $E_J \sim [2 − 4]$ GHz, $E_L < 0.4$ GHz has the highest T_1, the corresponding qubit frequencies are quite low, and hence are not well suited with our proposed gate operations. Moreover, reliable fabrication of a small junction corresponding to $E_J \sim 2$ GHz will be a difficult technical challenge. Thus, we focus on varying the qubit frequency by changing E_L and keeping $E_J = 4$ GHz for scalability. In practice, all three parameters can be fine tuned to vary the qubit frequency ω_{01}. We emphasize the flexibility of our approach: fluxonium circuits with parameters slightly deviating from the ones proposed in this work can still be scaled up favorably following the principles discussed in the following sections. On the other hand, we believe that it is valuable to explore different parameter regimes in the future.

III. READOUT

Dispersive readout in circuit quantum electrodynamics (cQED) architectures offers key advantages in the quest to build quantum computers [119,120]. Since the qubit's transition frequency is far away from that of the resonator, the probability of qubit excitation being converted to cavity photons is negligible. This detuning thus protects the qubit from spontaneous emission [121]. Dispersive readout has also been demonstrated to be fast and to have high fidelity [70], even when multiple qubits are readout simultaneously in a multiplexed fashion [122,123]. Quantum nondemolition (QND) measurement also allows qubit initialization by heralding [124–126] or by active feedback [127,128]. It has thus become the standard technique in modern superconducting quantum information processors [6,31,129]. In this section, we review the dispersive interaction framework in a fluxonium-resonator system and discuss its advantages upon scaling up.

When an atom is off resonantly coupled to a resonator, their dispersive interaction results in a resonator frequency dependent on the state of the qubit, allowing measurement of the latter by probing the former [119,130], as depicted in Fig. 3(a). The generic Hamiltonian describing such a system can be written as [131]

$$\hat{\mathcal{H}}_{\text{sys}}/\hbar = \sum_l \omega_l |l\rangle\langle l| + \sum_j \omega_j \hat{a}_j^\dagger \hat{a}_j$$
$$+ \sum_j \sum_{l,l'} g_{j;l,l'} |l\rangle\langle l'|(\hat{a}_j + \hat{a}_j^\dagger). \quad (3)$$

Here, $\hat{a}^\dagger$ ($\hat{a}$) is the resonator's creation (annihilation) operator, l and j, respectively, indicate the levels of the atom with frequency ω_l and resonator with frequency ω_j. The coupling coefficient $g_{j;l,l'}$ depends on the geometric coupling constant g_j between them and the corresponding matrix element of the qubit, $g_{j;l,l'} = g_j |\langle l|\hat{C}|l'\rangle|$, where $\hat{C} = \hat{n}$ for capacitive coupling and $\hat{C} = \hat{\varphi}$ for inductive coupling.

While selection rules in transmons limit the dispersive interaction to the nearest levels [132], the lack of such rules in fluxonium allows coupling between various qubit transitions and resonator modes. Thus, even for computational frequencies in the range below 1 GHz, the qubit's $|0\rangle \rightarrow |1\rangle$ transition still shifts the resonator via virtual transitions close to the latter's resonance. The dispersive regime is defined for this generic system following the condition $|\omega_{l,l'} - \omega_j| \gg g_{j;l,l'}\sqrt{\langle \hat{a}_j^\dagger \hat{a}_j \rangle + 1}$.

The generic Hamiltonian in Eq. (3) can be simplified to that describing a two-level system dispersively coupled to a single-mode harmonic oscillator with an effective dispersive shift χ_{01}:

$$\hat{\mathcal{H}}_{\text{disp}}/\hbar \approx \omega_{01}|1\rangle\langle 1| + (\omega_R + \chi_{01}|1\rangle\langle 1|)\hat{a}^\dagger \hat{a}, \quad (4)$$
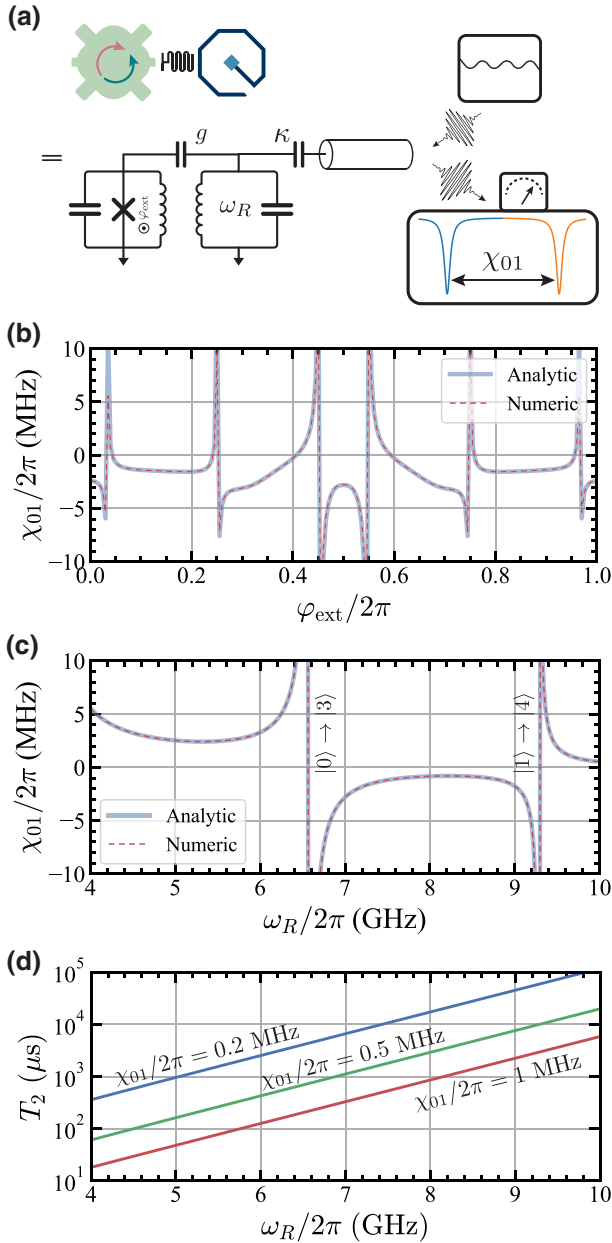
FIG. 3. Dispersive readout. (a) Schematic of a fluxonium qubit coupled to a readout resonator with coupling constant g. The resonator is then coupled to the readout bus with coupling rate κ, allowing measurement of its resonance ω_R, which is shifted slightly from its bare value, depending on the state of the qubit. No Purcell filter is needed. (b) Dispersive shift χ_{01} across one flux period for qubit parameters $\{E_J, E_C, E_L\} = \{4, 1, 1\}$ GHz, resonator frequency $\omega_R/2\pi = 7$ GHz, and capacitive coupling constant $g/2\pi = 100$ MHz. Numerical diagonalization results are the same for $p = 1$ and $p = 10$ photons. (c) Dispersive shift χ_{01} for qubit parameters $\{E_J, E_C, E_L\} = \{4, 1, 1\}$ GHz at flux bias $\varphi_{\text{ext}}/2\pi = 0.5$, corresponding to $\omega_{01}/2\pi \sim 0.58$ GHz, coupling constant $g/2\pi = 100$ MHz, and varying resonator frequency ω_R. (d) Thermal photon dephasing time for the same qubit and resonator parameters in (c), with resonator temperature $T = 50$ mK and dispersive shift $\chi_{01}/2\pi = \{0.2, 0.5, 1\}$ MHz, which can be changed by varying the geometric coupling constant g.

where ω_{01} and $\omega_R \equiv \omega_{j=0}$ are, respectively, the qubit's $|0\rangle \to |1\rangle$ and resonator's resonance frequencies, which are slightly Lamb shifted [133]. The structure of the charge matrix elements as shown in Fig. 2(c), with n_{01} small compared to others, is favorable for qubit-resonator capacitive coupling as the Purcell loss is further suppressed. In addition, capacitive coupling can be experimentally implemented in straightforward fashion, similar to the transmon case. The dispersive shift χ_{01} for qubit-resonator geometric coupling constant $g \equiv g_{j=0}$ can be derived using second-order perturbation theory as [131]

$$\chi_{01} = g^2 \left[\sum_{l \neq 0} |n_{0l}|^2 \frac{2\omega_{0l}}{\omega_{0l}^2 - \omega_R^2} - \sum_{l \neq 1} |n_{1l}|^2 \frac{2\omega_{1l}}{\omega_{1l}^2 - \omega_R^2} \right]. \tag{5}$$

While the fourth-order corrections account for self-Kerr and cross-Kerr interactions, the additional corrections added to the dispersive shift given by Eq. (5) are negligible [131]. In the case where the perturbation approach breaks down, e.g., when the dispersive condition is not satisfied, numerical diagonalization of the coupled system [134] may work best, and has been shown to consistently match experimentally extracted data up to hundreds of photons [56,57].

For fluxonium parameters $\{E_J, E_C, E_L\} = \{4, 1, 1\}$ GHz, we compute the dispersive shift of a cavity due to the qubit's $|0\rangle \to |1\rangle$ transition as a function of the external flux bias φ_{ext} using Eq. (5) with the resonator frequency $\omega_R/2\pi = 7$ GHz and coupling constant $g/2\pi = 100$ MHz, both of which are common for resonators integrated in transmon architectures. For comparison, we numerically diagonalize a fluxonium-resonator system and extract the photon-number-dependent shift $\chi_{01}(p) = (\omega_{p+1,1} - \omega_{p,1}) - (\omega_{p+1,0} - \omega_{p,0})$, where p is the number of resonator photons on average and the second subscript denotes the state of the qubit. As shown in Fig. 3(b), the second-order approximation matches the numerical result perfectly for $p = [1 - 10]$ photons. Therefore, the simple relation given by Eq. (5) can be used to estimate the dispersive shift χ_{01} in most cases, avoiding the resource-intensive task of diagonalizing systems with large Hilbert space. Interestingly, although the qubit frequency goes from approximately 5.5 GHz at zero external flux to approximately 0.58 GHz at half-integer flux quantum bias, the dispersive shift amplitude remains largely within a factor of 2, with $\chi_{01}/2\pi \geq 1$ MHz across almost the entire flux period.

To explore the multiplexing capability of the readout, we simulate the dispersive shift χ_{01} with varying readout frequency as shown in Fig. 3(c) for a qubit with parameters $\{E_J, E_C, E_L\} = \{4, 1, 1\}$ GHz biased at $\varphi_{\text{ext}}/2\pi = 0.5$, corresponding to qubit frequency $\omega_{01}/2\pi \sim 0.58$ GHz. By inspecting Eq. (5) and the selection rules in Fig. 2(c),

we can expect a large shift when the cavity resonance is close to qubit transitions $|0\rangle \rightarrow |3\rangle$ or $|1\rangle \rightarrow |4\rangle$, and a plateau in between, which are confirmed by the simulation results. We obtain $|\chi_{01}|/2\pi \geq 1$ MHz for a nominal coupling constant $g/2\pi = 100$ MHz with the resonator frequency $\omega_R/2\pi$ ranging from 4 to 10 GHz, indicating a fast and flexible readout. In addition, the plateaus imply the same level of dispersive shift when there are fluctuations in qubit parameters. As a result, qubits with similar energy scales can be measured via individual resonators without further design constraints. We note that in addition to the small charge matrix element n_{01}, the qubit frequency $\omega_{01}/2\pi \sim 0.58$ GHz is much lower than the target resonator frequency, so relaxation through the resonator is strongly suppressed. This eliminates the general need for Purcell filters, although the radiative decay limit of a device depends on its specific geometry and structure, as shown in more detail in Appendix A.

Having established the mechanisms behind dispersive measurement in fluxonium systems, we must take into account the following readout design considerations to minimize dephasing effects. In case the resonator frequency is close to the qubit transitions, $|\omega_R - \omega_{\{03,14\}}| \sim g$, the dispersive shift can be large at the expense of short energy relaxation times associated with these transitions due to spontaneous emission [121]. This may lead to dephasing of the computational states due to excitation to higher levels. For example, if the relaxation rate of the $|0\rangle \rightarrow |3\rangle$ transition is close to the resonator's linewidth, $\Gamma_{3\rightarrow 0}/2\pi \approx \kappa/2\pi = 2$ MHz, and the qubit's effective temperature is $T_{\text{eff}}(\omega_{03}) = 50$ mK [135], the excitation rate would follow the principle of detailed balance, $\Gamma_{0\rightarrow 3}/2\pi \sim 10$ kHz, corresponding to a dephasing time $T_\phi \approx 30\,\mu$s for the $|0\rangle$ and $|1\rangle$ states. Therefore, it is best to avoid this scenario to protect the computational subspace from decoherence. A quick estimation to find a suitable readout frequency range is given in Appendix A.

There is inevitable thermal photon dephasing trade-off [135,136] coming from the dispersive interaction with the resonator's fundamental mode, which we compute (see Appendix A) and plot in Fig. 3(d) for a resonator with varying resonance frequency ω_R, using an effective temperature $T_{\text{eff}}(\omega_R) = 50$ mK [135] and resonator linewidth $\kappa/2\pi = 2$ MHz. In general, a resonator with frequency ω_R closer to the $|1\rangle \rightarrow |4\rangle$ transition has a lower thermal photon population, resulting in less dephasing. A compromise between readout signal, which scales with χ_{01} [120] and coherence time, can also be made.

While virtual transitions $|0\rangle \rightarrow |3\rangle$ and $|1\rangle \rightarrow |4\rangle$ give rise to a finite dispersive shift, the matrix elements corresponding to higher-order transitions quickly vanish beyond 10 GHz, as shown in Fig. 2(c). As a result, there is no coupling between the qubit and any higher modes of the readout resonator, and thus no additional dephasing mechanisms associated with those modes. This

justifies reducing the resonator model to a single mode in Eq. (4).

Although the dispersive shift should be reasonably small to reduce effect from thermal photon dephasing, as shown in Fig. 3(d), a large number of resonator photons can be used to improve the signal amplitude substantially [56], allowing strong readout signal for all fluxoniums around the bus. Moving forward, improvement of the cryogenic setup [135,137,138] to lower the resonator's effective temperature will reduce thermal photon population exponentially for a given dispersive shift, enabling better measurement without compromising qubit coherence.

The multiplexed readout platform can be arranged as shown in Fig. 1, with four resonators spaced around a common bus. The dispersive shifts can be engineered to be within a plateau, so fluctuations in qubit frequencies would have negligible effect on readout performance. The resonator frequencies can be spaced sufficiently far apart to suppress off-resonant driving of untargeted resonators, which may lead to additional dephasing of qubits [123]. Since there is no fundamental requirement for Purcell filters to suppress radiative dissipation [66–68], the proposed platform's complexity and design constraints are reduced, leading to better scalability. The geometric coupling constant g can be designed to target a dispersive shift $\chi_{01}/2\pi \sim 1$ MHz, which facilitates fast readout while the coherence times can still be around 1 ms if the resonator frequency is chosen to be higher than 8 GHz, assuming a practical resonator temperature $T = 50$ mK. Notably, Ref. [56] reports a SNR = 3 for a fluxonium system with a dispersive shift of approximately $\chi_{01}/2\pi \sim 1$ MHz using only a few photons in a measurement setup consisting of a Josephson parametric amplifier with 20-dB gain. We expect the readout fidelity of our proposed platform to be similar, with minimal non-QND effect, if the measurement setup is designed to have sufficient measurement efficiency.

IV. SINGLE-QUBIT GATES

Conventionally, single-qubit control in superconducting qubits is implemented by applying a radiation pulse on resonance with the transition frequency of the computational levels. Ideally, qubits consist of only two levels, so arbitrarily short square pulses are technically sufficient to make high-fidelity gates. In practice, quantum systems typically consist of many energy levels, $\hat{\mathcal{H}}_Q/\hbar = \sum_{j=1}^{d-1} \omega_j |j\rangle\langle j|$, and the transition frequencies differ by an amount $\alpha_j = (\omega_{j,j+1} - \omega_{j-1,j})/2\pi$, defined as the anharmonicity. In most cases, the lowest two levels of a quantum system are used as computational basis, and we consider the only relevant term, $\alpha \equiv \alpha_1$. To avoid inadvertently driving other levels, shaping the pulse to reduce its bandwidth is required [139,140].

Intuitively, we expect errors in our operation when the pulse bandwidth approaches α. In the extreme case of a harmonic oscillator, all the transition frequencies are equal, thus we inevitably excite other levels when we apply a resonant drive. In transmons, $\alpha = (\omega_{12} - \omega_{01})/2\pi \approx -E_C$, where E_C is the charging energy, with typical value $E_C \sim 0.25$ GHz. For fluxonium within our proposed parameter regime, $\alpha \sim 3$ GHz, suggesting generally much lower single-qubit gate error using similar control techniques. However, the low qubit frequency implies that fast rotation does not follow the rotating wave approximation (RWA) [141], so the dynamical evolution of the computational subspace may become intractable. In this section, we explore the performance limit of single-fluxonium gates via both charge and flux microwave controls, which are, respectively, coupled capacitively and inductively to the qubit, as shown in the schematic in Fig. 4(a). We focus on X and Y rotations induced by microwave drives, as Z rotations are typically implemented virtually by the control software [142].

First, we simulate single-qubit operations for the proposed fluxonium parameters $\{E_J, E_C, E_L\} = \{4, 1, 1\}$ GHz, corresponding to qubit frequency $\omega_{01}/2\pi \sim 0.58$ GHz at external flux bias $\varphi_{\text{ext}}/2\pi = 0.5$. Since the quantum dynamics in this low-frequency subspace is susceptible to effects from the counter-rotating terms, our approach is to numerically compute the qubit dynamics in the lab frame without assuming RWA, then extract the unitary $\hat{\mathcal{U}}_{\text{total}}(t) = e^{i\phi}\hat{\mathcal{U}}_{\text{comp}}(t)\hat{\mathcal{U}}_{\text{others}}(t)$. Subsequently, we analyze the computational subspace evolution under $\hat{\mathcal{U}}_{\text{comp}}(t)$, disregarding the accumulated global phase ϕ. The dynamics of higher states governed by $\hat{\mathcal{U}}_{\text{others}}(t)$ accounts for finite leakage out of the computational subspace. We present the results for $\{X, Y\}(\pi)$ gates here since they require higher pulse amplitudes for the same gate time compared to other rotation angles, and are thereby more susceptible to errors.

To this end, we couple a microwave pulse to the qubit's charge $\hat{n}$ (or phase $\hat{\varphi}$) degree of freedom, which can be modeled by adding a driving term $\hat{\mathcal{H}}_d/h = \mathcal{E}(t) \times \hat{n}$ (or $\hat{\varphi}$) to the Hamiltonian given by Eq. (1). The pulse can be described as

$$\mathcal{E}(t) = \mathcal{E}_I(t)\cos(\omega_d t) + \mathcal{E}_Q(t)\sin(\omega_d t), \qquad (6)$$

where $\mathcal{E}_I(t)$ and $\mathcal{E}_Q(t)$ are time-dependent amplitudes of the in-phase and quadrature components of the pulse, and ω_d is the drive frequency. First, we apply an on-resonant in-phase pulse, $\omega_d = \omega_{01}$ and $\mathcal{E}_Q(t) = 0$, with gate time $\tau_g = 10$ ns. The cosine envelope is chosen since its ramping is smooth and there is no need for truncation,

$$\mathcal{E}_I(t) = \frac{\epsilon_d}{2}\left[1 - \cos(2\pi t/\tau_g)\right], \qquad (7)$$

where the pulse amplitude ϵ_d is tuned up to implement a π rotation, following the simple relation $\epsilon_d \eta_{01} \tau_g = 0.25$,

(a) Charge drive   Flux drive
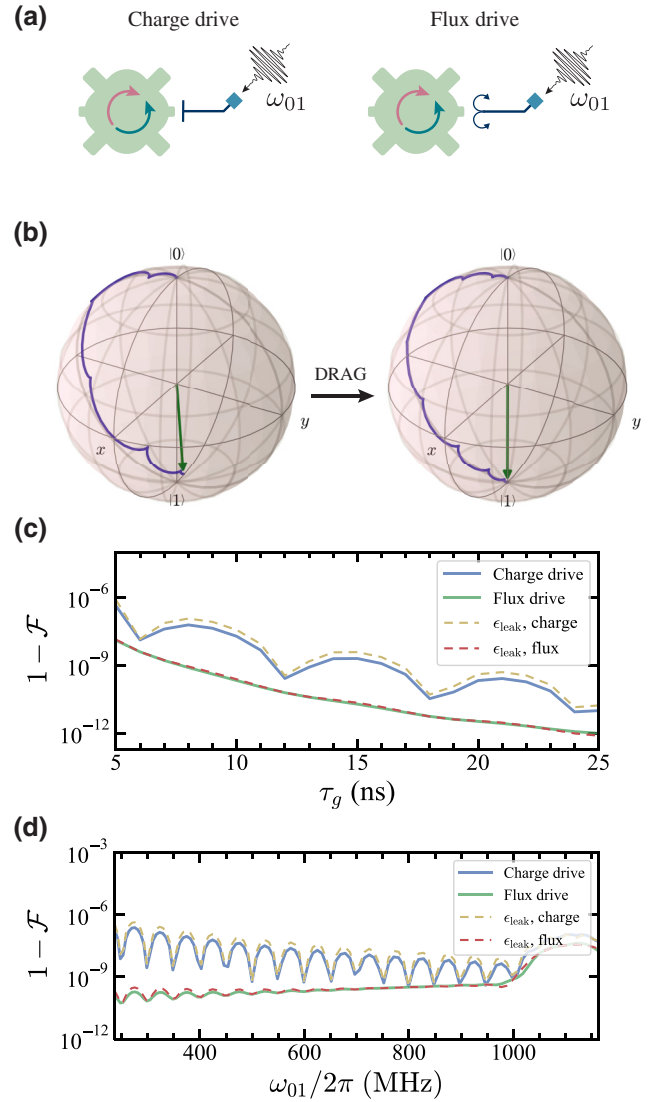
(b)

(c)

(d)

FIG. 4. Single-qubit gate. (a) Schematic showing microwave control of the qubit via charge and flux drives. (b) Trajectory of the qubit vector on the Bloch sphere before and after optimization using DRAG for flux driving with $\tau_g = 10$ ns. (c) Gate error and state leakage for varying gate time for both charge and flux coupling. (d) Gate error and leakage for varying qubit frequency, with gate time $\tau_g = 10$ ns. ω_{01} is changed by varying the inductive energy E_L.

with $\eta_{01} \equiv n_{01}$ for charge driving and $\eta_{01} \equiv \varphi_{01}$ for flux driving (see Appendix C). Our flux driving model is justified by the gauge choice in Eq. (1). The qubit state's trajectory on the Bloch sphere is visualized in Fig. 4(b, left), with its axis tilted due to the fast counter-rotating terms at $2\omega_d$.

This can be corrected using the derivative removal by adiabatic gate (DRAG) technique, which modifies the spectral profile of the pulse [143,144]. Specifically, the three control parameters we have, namely the envelopes $\mathcal{E}_I(t)$, $\mathcal{E}_Q(t)$, and the detuning $\delta = \omega_d - \omega_{01}$, can be tuned

to effectively correct the tilt and improve gate fidelity, similar to the transmon case [145–147]. The first-order correction is implemented by sending a quadrature pulse simultaneously with an amplitude proportional to the time derivative of the in-phase pulse $\mathcal{E}_Q(t) = \lambda \dot{\mathcal{E}}_I(t)$, and adding a small detuning δ. We find that this simple technique suppresses most of the gate error. The corrected trajectory for flux driving is shown in Fig. 4(b, right). Optimization details are discussed in Appendix C.

Next, we sweep the gate time τ_g, optimizing the gate parameters for each instance, then compute the corresponding error $1 - \mathcal{F}$, where the single-qubit gate fidelity $\mathcal{F}$ is defined as [148]

$$\mathcal{F} = \frac{1}{6} \left[\mathrm{Tr}(\hat{\mathcal{U}}^\dagger \hat{\mathcal{U}}) + |\mathrm{Tr}(\hat{\mathcal{U}}^\dagger \hat{\mathcal{U}}_{\mathrm{ideal}})|^2 \right], \tag{8}$$

with $\hat{\mathcal{U}} \equiv \hat{\mathcal{U}}_{\mathrm{comp}}$, which may not be unitary. The result in Fig. 4(c) shows low errors for gate times as fast as $\tau_g = 5$ ns, and the error rate decreases exponentially for longer gate times, with error below 10^{-7} for $\tau_g = 25$ ns in both charge and flux coupling cases. We attribute the residual errors to leakage, $\epsilon_{\mathrm{leak}} = 1 - (P_0 + P_1)$, which are consistent with the simulation results.

By varying the inductive energy E_L from 0.5 to 1.6 GHz with other energy parameters fixed, we can tune the qubit frequency $\omega_{01}/2\pi$ from 237 to 1163 MHz. We numerically simulate the gate error for a $\tau_g = 10$ ns cosine pulse for both charge and flux coupling across this frequency range. The result in Fig. 4(d) shows that the gate error, mainly coming from finite leakage, remains below 10^{-6}. This promises high-fidelity single-qubit operations in a large-scale device constructed from fluxoniums with approximately 1-GHz frequency bandwidth. More importantly, this implies that we can treat the circuit as a quasi-two-level system, especially for longer gate times.

Notably, due to the difference between flux and charge matrix elements discussed in Sec. II, charge coupling requires a stronger drive amplitude to implement the same rotation compared to flux coupling, so there is more leakage to higher levels for this case. Therefore, flux driving is better for operations involving computational states. Another advantage of flux coupling is that an rf flux drive can be combined with the dc flux bias using a diplexer, forming a single control line [149], which is shown as the anchor in Fig. 1. A symmetric flux line helps null parasitic capacitive coupling to the qubit, protecting it from energy decay [150]. A fast-flux control line working at rf frequency has also been demonstrated to be compatible with fluxonium qubit having coherence times exceeding 100 μs [54,65].

Typical microwave control of superconducting qubits involves *IQ* mixing of a low-frequency pulse with a rf carrier tone, which is susceptible to carrier leakage, imperfect sideband suppression, and pulse distortion due to nonideal electronic performance. At the low qubit frequency regime we propose, the computational states can be controlled via microwave pulses synthesized directly from the arbitrary waveform generator (AWG), eliminating the need for *IQ* mixers and rf microwave sources, together with the associated sources of signal instability. This would improve resource efficiency and reduce operational complexity significantly upon upgrading to large-scale devices.

Additionally, operating at low frequency gives us an advantage regarding microwave crosstalk, which is prevalent in superconducting qubit quantum processors. This spurious interaction between qubits and neighboring control lines may come from direct coupling, but is most likely due to radiation generated by an impedance mismatch at wire-bond pads, or coupling to common box modes [151,152]. Interestingly, crosstalk at the frequency range below 1 GHz is substantially smaller than at 5 GHz. This can be attributed to better impedance matching to the wire bonds and disappearance of spurious modes at low frequencies [152]. Such a feature will greatly benefit future quantum processors based on fluxonium qubits. For flux driving, strong inductive coupling between the qubit and its designated control is required due to the former's large inductive shunt. This implies a strong on-off ratio and subsequently lower crosstalk between adjacent control lines and qubits. This feature was recently used to perform qubit control in a two-dimensional (2D) architecture [65], with simultaneous single-qubit gate fidelity as high as $\mathcal{F} = 0.9997$, while the coherence time was maintained at around 100 μs.

V. MULTI-QUBIT COUPLING

In this section, we explore different coupling scenarios and discuss their properties. We show that a multipath coupling technique can be used to statically suppress the spurious ZZ rate across the whole lattice while allowing the computational states to have sufficiently strong interaction for fast entangling gate operations.

A quantum system consisting of two directly coupled fluxonium qubits can be described by the Hamiltonian [61]

$$\hat{\mathcal{H}} = \hat{\mathcal{H}}_A + \hat{\mathcal{H}}_B + \hat{\mathcal{H}}_{\mathrm{coupl}}, \tag{9}$$

where $\hat{\mathcal{H}}_{A,B}$ is the bare (uncoupled) Hamiltonian given by Eq. (1), and the coupling term can be written as $\hat{\mathcal{H}}_{\mathrm{coupl}}/h = J_C \hat{n}_A \hat{n}_B$ for capacitive coupling and $\hat{\mathcal{H}}_{\mathrm{coupl}}/h = -J_L \hat{\varphi}_A \hat{\varphi}_B$ for inductive coupling. Here, $\hat{n}_{A,B}$ and $\hat{\varphi}_{A,B}$ are, respectively, the charge and phase degrees of freedom of qubit A and qubit B. The coupling coefficients are proportional to the mutual circuit element, $J_C = 4e^2 C_M/(C_A C_B)$ [153] and $J_L = (\hbar/2e)^2 L_M/(L_A L_B)$ [134] in the weak coupling regime where $C_M \ll C_A, C_B$ and $L_M \ll L_A, L_B$.

We use the notation $|k_A l_B\rangle$ to indicate states of interacting systems in the rest of this work. The bare states of

TABLE I. Coupled fluxonium parameters.

Qubit	E_J (GHz)	E_C (GHz)	E_L (GHz)	$\omega_{01}/2\pi$ (MHz)
A	4.0	1.0	0.9	499
B	4.0	1.0	1.0	581

TABLE II. Coupled fluxonium parameters for simulation involving sweeping of the qubit-qubit detuning $\Delta = \omega_B - \omega_A$.

Qubit	E_J (GHz)	E_C (GHz)	E_L (GHz)	$\omega_{01}/2\pi$ (MHz)
A	4.0	1.0	0.5	237
B	4.0	1.0	[0.55-1.6]	[264-1163]

uncoupled qubits are denoted as $|k_A l_B\rangle_0$. Here, we focus on using multi-qubit gates based on the interaction between computational states, which causes mixing between $|01\rangle$ and $|10\rangle$. To characterize the level of their hybridization, we compute the normalized cross matrix element defined as

$$\mu_\varphi = \frac{|\langle 00|\hat{\varphi}_A \otimes \hat{I}_B|01\rangle|}{|\langle 00|\hat{\varphi}_A \otimes \hat{I}_B|10\rangle|}. \tag{10}$$

This quantity is zero for the uncoupled system since $_0\langle 00|\hat{\varphi}_A \otimes \hat{I}_B|01\rangle_0 = 0$, and becomes finite due to dressing between the computational states. The normalization form defined by Eq. (10) is chosen such that the corresponding matrix element amplitude is taken into account. For example, the normalized cross matrix element for the charge operator $\hat{n}_A \otimes \hat{I}_B$ can be used to characterize the mixing as well.

As the amplitude of μ_φ does not carry practical information, we can compare it with an equivalent quantity in a system of coupled spins described by the Hamiltonian

$$\hat{\mathcal{H}}_{ss}/\hbar = \frac{1}{2}\omega_A \hat{Z}_A + \frac{1}{2}\omega_B \hat{Z}_B + 2\pi J_{eff}\hat{X}_A \hat{X}_B. \tag{11}$$

For $\omega_A/2\pi = 499$ MHz, $\omega_B/2\pi = 581$ MHz, and $J_{eff} = 10$ MHz, this system has a normalized cross matrix element $\mu_X = 0.11$, where

$$\mu_X = \frac{|\langle 00|\hat{X}_A \otimes \hat{I}_B|01\rangle|}{|\langle 00|\hat{X}_A \otimes \hat{I}_B|10\rangle|}. \tag{12}$$

Fast microwave-entangling gates in coupled transmons system with similar J_{eff} have been demonstrated [31,78], so we use this μ_X value as a reference. More detail on the mapping between coupled spins model and interacting fluxoniums system is discussed in Appendix E.

After diagonalizing the Hamiltonian in Eq. (9) with parameters listed in Table I for varying charge- and flux-coupling constants, we extract μ_φ together with the static longitudinal coupling rate defined as

$$\zeta_{ZZ} = \omega_{|00\rangle} + \omega_{|11\rangle} - \omega_{|10\rangle} - \omega_{|01\rangle}, \tag{13}$$

where $\omega_{|k_A l_B\rangle}$ is the eigenenergy of the two-qubit state $|k_A l_B\rangle$. This static ZZ can be viewed as an always-on entangling operation, leading to errors in both local and nonlocal operations in a large-scale processor [71]. Our

primary goal is thus to enable a sufficiently large exchange interaction characterized by μ_φ, and at the same time to suppress ζ_{ZZ}.

As shown in Fig. 5(a), capacitive coupling results in a large ZZ rate to achieve a level of dressing corresponding to $\mu_\varphi \sim 0.11$. This can be understood as follows. Since the longitudinal coupling is a dispersive effect, interactions between higher levels play an important role. Meanwhile, the charge matrix elements follow $n_{01} < n_{others}$ [Fig. 2(c)], resulting in strong mixing between noncomputational states compared to computational states. This leads to large ζ_{ZZ} in order to reach a desired μ_φ. On the other hand, as shown in Fig. 5(b), inductive coupling gives a rather small ζ_{ZZ} to reach the same μ_φ, because $\varphi_{01} > \varphi_{others}$. Therefore, capacitive coupling does not provide a sufficient exchange interaction between computational states but is better for tuning ZZ, and vice versa for inductive coupling.

Based on these selection rules, we propose a multipath coupling approach that includes an inductive coupling term $-J_L\hat{\varphi}_A\hat{\varphi}_B$ that enables the exchange interaction in the computational states, and a small capacitive coupling term $J_C\hat{n}_A\hat{n}_B$ that can be used to suppress the residual static ZZ. As shown in Fig. 5(c), for qubits with parameters listed in Table I and inductive coupling constant $J_L = 2$ MHz (corresponding to $L_M = 363$ pH), a small capacitive coupling with coefficient $J_C = 11.5$ MHz (corresponding to $C_M = 28$ aF) is needed to make $|\zeta_{ZZ}| = 0$.

Figure 5(d) further shows that even when the fluxonium parameters fluctuate within 10%, the static ZZ rate for a pair of qubits coupled in multipath fashion would remain below 1 kHz, hence the scheme is resilient against parameter fluctuations. Interestingly, ζ_{ZZ} stays close to zero across a wide range of E_L^B [cf. Fig. 16(b, inset)], so the same coupling design parameters can be used for many qubit pairs if ω_{01} is tuned by varying E_L, promising another advantage upon scaling up.

The primary challenge in scaling up this multipath coupling scheme will be to combine the large inductive coupling with $L_M \sim 360$ pH and the small capacitive coupling with $C_M \sim 30$ aF. For the inductive part, the most straightforward approach is to design neighboring qubits to share sections of their superinductors [103]. Since the qubits must be placed next to each other in this case, classical microwave control crosstalk can become significant. Future development of a coupling element [154–156] or an inductive bus analogous to the resonator bus in transmon
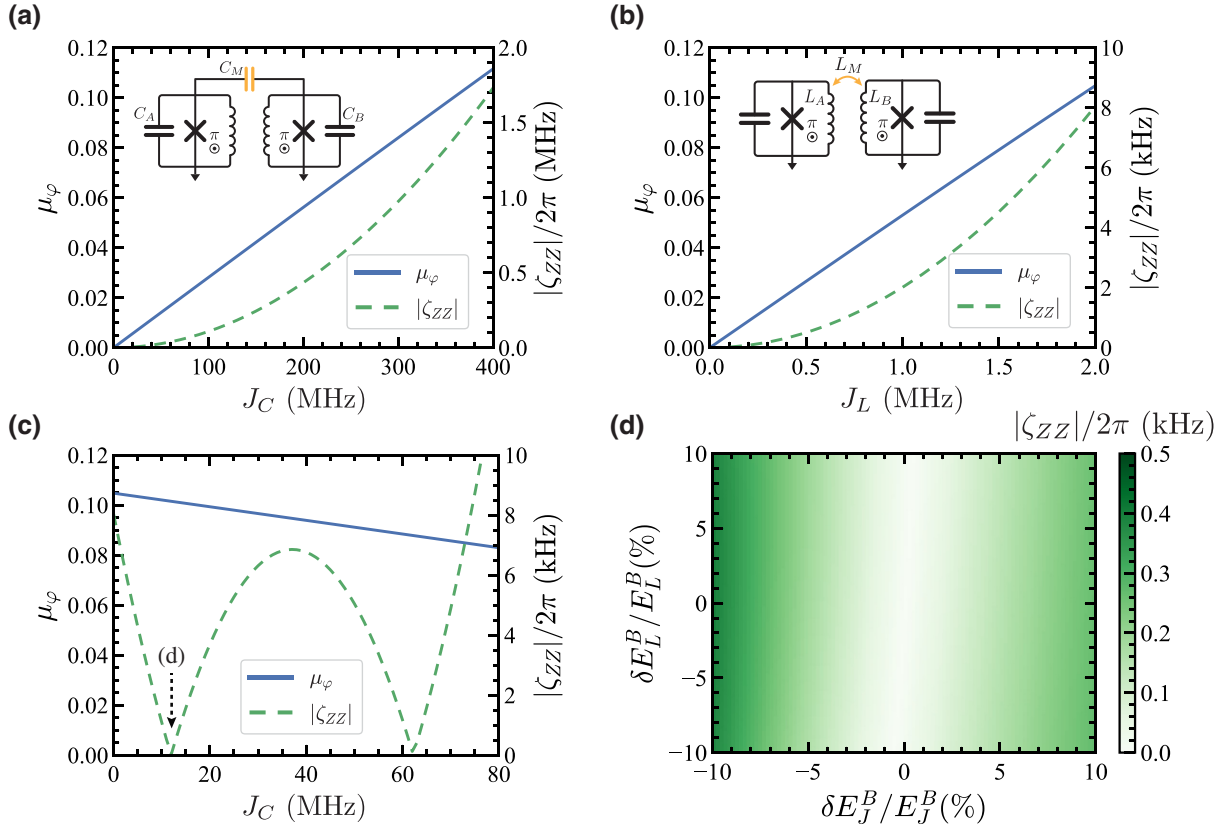
FIG. 5.   Multi-fluxonium coupling for qubit parameters listed in Table I. Normalized matrix element μ_φ and static longitudinal coupling rate ζ_{ZZ} for varying (a) capacitive coupling $\hat{\mathcal{H}}_{\text{coupl}} = J_C \hat{n}_A \hat{n}_B$, (b) inductive coupling $\hat{\mathcal{H}}_{\text{coupl}} = -J_L \hat{\varphi}_A \hat{\varphi}_B$, and (c) multipath coupling $\hat{\mathcal{H}}_{\text{coupl}} = J_C \hat{n}_A \hat{n}_B - J_L \hat{\varphi}_A \hat{\varphi}_B$ with $J_L = 2$ MHz. (d) Variation of static longitudinal coupling rate ζ_{ZZ} due to fluctuations in qubit B's parameters for coupling coefficients $\{J_L, J_C\} = \{2, 11.5\}$ MHz.

architecture [119,157] would be ideal. For the capacitive part, microwave design following standard transmon techniques will be sufficient to realize the required coupling. Since the proposed charging energy E_C parameter corresponds to a small antenna, and the ground plane will screen a large portion of qubit-qubit cross capacitances, it is straightforward to engineer the desired mutual capacitance.

VI. MULTI-QUBIT GATES

In this section, we investigate the performance of two types of microwave-activated entangling operations in the low frequency regimes for $J_L = 2$ MHz and $J_C = 11.5$ MHz to cancel the static ZZ rate, corresponding to $J_{\text{eff}} \approx 11$ MHz in Eq. (11). Having shown that leakage outside the computational subspace is negligible, $\epsilon_{\text{leak}} < 10^{-6}$ for sufficiently long gate time in Sec. IV, and that the static ZZ can be cancelled using multipath coupling in Sec. V, we may reduce the complex multi-fluxonium system to a simpler model describing two coupled spins. We discuss this mapping in more detail in Appendix E, and proceed to use the practical formalism describing two-level systems here, denoting $\omega_A \equiv \omega_{01}^A$ and $\omega_B \equiv \omega_{01}^B$.

The entangling gates we study are the cross-resonance (CR) CNOT [73–75] and differential ac-Stark CZ [78,79] gates, which can be used to implement quantum error correction codes [37,38]. These microwave gates involve only the high-coherence computational states, so the errors resulting from decoherence are small. In addition, they can be readily implemented using the same single-qubit control components on the chip, in this case the rf flux lines, reducing the design and fabrication constraints overhead upon scaling up. We note that, while not explored here, other entangling gates such as the ac-Stark shift [119,157] and the two-photon [158,159] SWAP-like gates are also compatible with our proposed architecture.

A. Cross-resonance controlled-NOT gate

Among various microwave-activated entangling operations, the CR gate has been the most popular for fixed-frequency superconducting qubits. It was first proposed considering a model of two coupled two-level systems [74,160], and subsequently implemented using flux qubits [73,75], followed by its application on transmons [76] with a gate fidelity of 95%. Substantial improvements to the
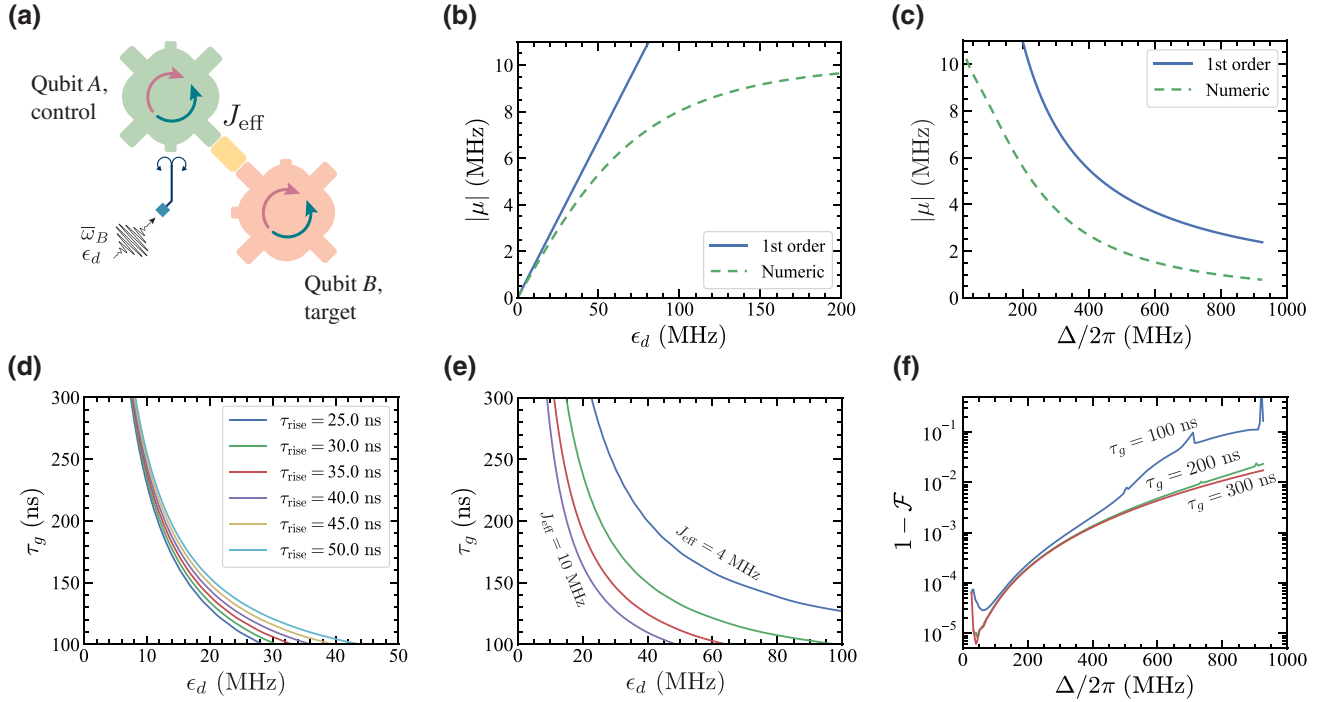
FIG. 6. Cross-resonance gate simulation. Except for plot (e), the coupling coefficients are $J_L = 2$ MHz and $J_C = 11.5$ MHz, corresponding to an effective exchange interaction rate $J_{\text{eff}} \sim 11$ MHz. Qubit parameters are listed in Table I for (b),(d), and (e). Qubit B's inductive energy $E_{L,B}$ is changed to vary the qubit-qubit detuning Δ as listed in Table II for (c),(f). (a) Gate scheme: a microwave pulse applied to qubit A at the dressed frequency $\overline{\omega}_B$ of qubit B will induce an effective ZX interaction, which entangles the qubits. (b) Effective ZX rate μ with varying drive amplitude ϵ_d. (c) Effective ZX rate μ with varying qubit-qubit detuning $\Delta = \omega_B - \omega_A$ for drive amplitude $\epsilon_d = 200$ MHz. (d) CNOT gate time τ_g for varying drive amplitude ϵ_d, with ramping time $\tau_{\text{ramp}} = \{25, 30, 35, 40, 45, 50\}$ ns. (e) CNOT gate time τ_g for varying drive amplitude ϵ_d with different effective exchange interaction strength $J_{\text{eff}} \sim \{4, 6, 8, 10\}$ MHz and gate ramping time $\tau_{\text{ramp}} = 50$ ns. (f) Gate error for varying qubit-qubit detuning Δ with pulse ramping time $\tau_{\text{ramp}} = 50$ ns, and total gate time $\tau_g = \{100, 200, 300\}$ ns.

gate were made using echo sequence [161] and a simultaneous cancellation tone [162], resulting in a gate fidelity of $\mathcal{F} = 99.1\%$. Recent tune-up procedures involving a rotary echo sequence have been used to demonstrate high-fidelity uniformly in a multi-qubit quantum processor [71]. On the theory side, after initial study of the gate [74,160,163], the need to understand and optimize the two-qubit CR interaction in coupled-transmon systems more thoroughly has led researchers to analyze it more rigorously [164–166], with optimal pulse shaping promising to improve the gate even further [167]. Recently, a single-step high-fidelity three-qubit iToffoli entangling gate based on CR interactions has been experimentally demonstrated, providing a more expressive gate set and possible reduction in circuit depth for NISQ algorithms [168].

Figure 6(a) depicts the implementation of the gate. Two coupled spins described by the Hamiltonian in Eq. (11) would have their transition frequencies shifted due to the dressing of the states, $\overline{\omega}_A = \omega_A - 2\pi J_{\text{eff}}/\Delta$, $\overline{\omega}_B = \omega_B + 2\pi J_{\text{eff}}/\Delta$, where $\Delta = \omega_B - \omega_A$ is the frequency detuning between the qubits. If the coupling J_{eff} is finite, a microwave tone applied to qubit A at the frequency of qubit B will excite qubit B, and its evolution pattern will depend

on the state of qubit A. Thus, the qubits can become entangled. Qubit A and qubit B are usually referred to in the literature as the *control* and *target* qubits, respectively [74].

We can approximate the entangling rate at the lowest order as follows. The microwave drive with amplitude ϵ_d induces the CR effect that manifests as [164]

$$\hat{\mathcal{H}}_{\text{CR,eff}}/h = (\epsilon_0 |01\rangle \langle 00| + \epsilon_1 |11\rangle \langle 10|) + \text{h.c.}, \quad (14)$$

where ϵ_0 and ϵ_1 can be viewed as the effective drive amplitudes on the target qubit when the control qubit is in states $|0\rangle$ and $|1\rangle$, respectively. The Hamiltonian in Eq. (14) can be rewritten using operator format to highlight the important ZX term [74,75],

$$\hat{\mathcal{H}}_{\text{CR,eff}}/h = m\hat{I}\hat{X} + \mu\hat{Z}\hat{X}, \quad (15)$$

where the IX coefficient is $m = (\epsilon_0 + \epsilon_1)/2$ in the absence of classical microwave crosstalk, and the ZX amplitude is $\mu = (\epsilon_0 - \epsilon_1)/2$. The effective drive coefficients in Eq. (14) can be approximated to the first order as $\epsilon_0 \approx -(2\pi J_{\text{eff}}/\Delta)\epsilon_d$, $\epsilon_1 \approx (2\pi J_{\text{eff}}/\Delta)\epsilon_d$, which yields $m \approx 0$ and $\mu \approx (2\pi J_{\text{eff}}/\Delta)\epsilon_d$ [164]. We note that in practice,

there is a finite *IX* amplitude from microwave crosstalk or when there is participation from other qubit levels, resulting in $m > 0$. The *ZI* term due to the control qubit's ac-Stark shift is also omitted in Eq. (15). In principle, these single-qubit operators commute with the desired *ZX* term, and hence do not degrade the gate fidelity.

To estimate the gate rate, which dictates how fast the qubits can be entangled, we compute the *ZX* amplitude μ for a pair of coupled fluxoniums with parameters listed in Table I, corresponding to bare qubit frequencies $\omega_A/2\pi = 499$ MHz, $\omega_B/2\pi = 581$ MHz. As mentioned above, we use coupling coefficients $J_L = 2$ MHz and $J_C = 11.5$ MHz, corresponding to an effective spin-spin exchange interaction rate $J_{\text{eff}} \approx 11$ MHz. In addition, we numerically compute the gate rate by applying a continuous microwave tone to qubit *A* at frequency $\overline{\omega}_B$ and extracting the oscillation frequency of qubit *B* [162]. The numerical procedure involves up to five levels in each qubit, which is sufficient to describe the essential dynamics and possible errors.

As shown in Fig. 6(b), the lowest-order estimation $\mu \approx (2\pi J_{\text{eff}}/\Delta)\epsilon_d$ agrees well with the numerically obtained result in the small drive amplitude region, where a perturbation approach is supposed to work well. However, at large drive amplitude, the rate approaches a plateau, indicating a saturated gate rate. Therefore, the gate cannot be made arbitrarily short by simply increasing the drive amplitude.

Next, we explore how the gate rate varies with different qubit-qubit detunings, which is important for large-scale devices. To this end, we fix qubit *A*'s parameters, with its inductive energy $E_{L,A} = 0.5$ GHz, and sweep qubit *B*'s inductive energy $E_{L,B} = [0.55 - 1.6]$ GHz, corresponding to qubit frequencies $\omega_A/2\pi = 237$ MHz and $\omega_B/2\pi = [264 - 1163]$ MHz, as listed in Table II. We repeat the simulation with these parameters, corresponding to qubit-qubit detuning $\Delta/2\pi = [27 - 926]$ MHz, using a large drive amplitude $\epsilon_d = 200$ MHz. Figure 6(c) shows the difference between the first-order approximation and the numerical results, with the latter showing a large but finite gate rate $|\mu| > 5$ MHz at small detuning, and a small gate rate $|\mu| < 1$ MHz as the detuning approaches 1 GHz.

Having established how the drive amplitude ϵ_d and qubit-qubit detuning Δ determine the gate rate, we proceed to calibrate the correct pulse and simulate the performance of the gate. The CR operation can be used to implement a CNOT unitary,

$$\hat{\mathcal{U}}_{\text{CNOT}} = \exp\left[\frac{i\pi}{4}(\hat{Z}\hat{I} + \hat{I}\hat{X} - \hat{Z}\hat{X} - \hat{I}\hat{I})\right]. \quad (16)$$

The *ZI* and *IX* terms commute with *ZX* and can be implemented using single-qubit gates, while the *II* term simply introduces a global phase. Hence, to realize a CNOT gate, we have to apply the CR pulse with time-dependent

amplitude $\mathcal{E}(t)$ for a time τ_g satisfying the condition

$$\int_0^{\tau_g} \mu(t)dt = \frac{\pi}{2}, \quad (17)$$

then add single-qubit gates, which have low errors as discussed in Sec. IV.

In practice, we tune up the gate numerically by initializing the qubit states to be $|00\rangle$ or $|10\rangle$, applying the drive with amplitude ϵ_d as a parameter, and optimizing the conditionality R [78,162], given as

$$R = \frac{1}{2}[(\langle\hat{X}\rangle_0 - \langle\hat{X}\rangle_1)^2 + (\langle\hat{Y}\rangle_0 - \langle\hat{Y}\rangle_1)^2 + (\langle\hat{Z}\rangle_0 - \langle\hat{Z}\rangle_1)^2]^{\frac{1}{2}}, \quad (18)$$

where, for example, $\langle\hat{X}\rangle_0$ is the expectation value of the target qubit's operator $\hat{X}$ when the control qubit is in state $|0\rangle$. R can also be viewed as an entanglement metric, with $R = 0$ for unentangled states and $R = 1$ for maximally entangled states. We can find the correct gate parameters by varying the gate time and amplitude to minimize $|1 - R|$. To avoid microwave leakage and at the same time ensure sufficient drive amplitude, we use a flat-top pulse envelope with cosine ramping at both ends,

$$\mathcal{E}(t) = \begin{cases} \frac{\epsilon_d}{2}\left[1 - \cos\frac{\pi t}{\tau_{\text{ramp}}}\right], & 0 \leq t \leq \tau_{\text{ramp}} \\ \epsilon_d, & \tau_{\text{ramp}} \leq t \leq \tau_g - \tau_{\text{ramp}} \\ \frac{\epsilon_d}{2}\left[1 - \cos\frac{\pi(\tau_g-t)}{\tau_{\text{ramp}}}\right], & \tau_g - \tau_{\text{ramp}} \leq t \leq \tau_g. \end{cases}$$

To tune up the correct parameters, we first compute the corresponding gate time τ_g for varying drive amplitude ϵ_d, with different ramping time τ_g. The results in Fig. 6(d) show that shorter gate time and longer ramping time require stronger drive amplitudes, as expected. We note that in principle, the effective coupling can also be engineered to allow faster gate time for the same drive amplitude, as simulated in Fig. 6(e).

Then, we simulate the performance of the gate by computing its fidelity with varying qubit-qubit detuning as listed in Table II, using pulse ramping time $\tau_{\text{ramp}} = 50$ ns and pulse duration $\tau_g = \{100, 200, 300\}$ ns. We optimize the pulse amplitude at each parameter point using the Nelder-Mead method to estimate the best gate fidelity. Figure 6(f) shows the gate error $1 - \mathcal{F}$, where the average gate fidelity $\mathcal{F}$ is defined for two-qubit gate as [148]

$$\mathcal{F} = \frac{1}{20}\left[\text{Tr}(\hat{\mathcal{U}}^\dagger\hat{\mathcal{U}}) + |\text{Tr}(\hat{\mathcal{U}}^\dagger\hat{\mathcal{U}}_{\text{ideal}})|^2\right]. \quad (19)$$

This shows that the fidelity generally gets worse for large detuning, with gate error ranging from around 10^{-5} at $\Delta/2\pi = 30$ MHz to 10^{-2} at $\Delta/2\pi = 900$ MHz. Since

the gate rate μ saturates steadily for large detuning Δ and strong drive amplitude ϵ_d, we can anticipate the gate to become worse when an appropriate ϵ_d cannot be found. Notably, a slightly longer gate time does not improve the fidelity substantially, so the best approach to achieve better gate fidelity at large detuning would be to increase the coupling rate and induce a higher gate rate for the same drive amplitude [cf. Fig. 6(e)]. Because the static ZZ rate is cancelled via the multipath coupling, stronger coupling should not introduce any adverse effects.

Since the drive frequency in the CR gate scheme is fixed to the target qubit, there can be stringent requirements on adjacent qubits' parameters to avoid frequency collisions. In qubit systems with low anharmonicity, in addition to avoiding the collision of $|0\rangle \to |1\rangle$ transitions between qubits, we also have to take into account quantum dynamics involving $|1\rangle \to |2\rangle$ transitions and multiphoton processes [166]. Our proposed architecture leverages the high anharmonicity of fluxonium to alleviate these requirements. This allows the gate to be reasonably fast with fidelity $\mathcal{F} \sim 0.99$ at large detuning.

B. Differential ac-Stark controlled-Z gate

Another useful two-qubit gate is the CZ gate, which is equivalent to the CNOT gate up to single-qubit rotations. Several microwave-activated CZ gates in superconducting circuit architectures have been implemented, including those utilizing the higher levels in transmons [169,170] or fluxonium [59,60], resonator-induced phase gate [171], parametric gate enabled by second-order nonlinearity [77], and recently based on differential ac-Stark shift of the computational states [78,79].

Here, we explore the CZ gate scheme where the microwave pulses are applied off resonantly to the low-frequency qubits, as depicted in Fig. 7(a). We note that since the static ZZ rate is negated via the multipath coupling, the ZZ interaction discussed in this section is purely dynamical. When the computational states are dressed by the microwave drives with respective amplitudes $\epsilon_{\{A,B\}}$ (which have cyclic frequency unit here), phases $\phi_{\{A,B\}}$, and at a frequency ω_d detuned from the qubit frequencies by $\delta_{\{A,B\}} = \omega_d - \omega_{\{A,B\}}$, a finite qubit-qubit exchange coupling J_{eff} turns on the dynamical ZZ interaction [78,79],

$$\zeta_{ZZ} \approx 4\pi J_{\text{eff}} \frac{\epsilon_A \epsilon_B}{\delta_A \delta_B} \cos(\phi_A - \phi_B), \quad (20)$$

which can be used in combination with single-qubit gates $\hat{I}\hat{Z}$ and $\hat{Z}\hat{I}$ to implement a CZ gate following the relation

$$\hat{\mathcal{U}}_{<sc>cz</sc>} = \exp\left[\frac{i\pi}{4}(\hat{Z}\hat{I} + \hat{I}\hat{Z} - \hat{Z}\hat{Z} - \hat{I}\hat{I})\right]. \quad (21)$$

We estimate the gate rate given by Eq. (20) and compare it with numerically obtained results for a pair of coupled

fluxoniums with parameters listed in Table I, together with coupling coefficients $J_L = 2$ MHz and $J_C = 11.5$ MHz, corresponding to an effective spin-spin exchange interaction rate $J_{\text{eff}} \approx 11$ MHz. When applying two continuous microwave tones at a frequency ω_d with the same phases, $\phi_A = \phi_B$, and amplitudes $\epsilon_A = \epsilon_B$, we simulate the dynamical evolution of the system using the master equation, then compute the phase evolution as $\phi_{ZZ}(t) = \phi_{00}(t) + \phi_{11}(t) - \phi_{01}(t) - \phi_{10}(t)$. Fitting $\phi_{ZZ}(t)$ to a simple linear function of time yields the corresponding ZZ rate.

Figure 7(b) shows excellent agreement between numerically and analytically obtained rates for relatively weak drive amplitudes $\epsilon_A/2\pi = \epsilon_B/2\pi = 10$ MHz. Notably, the analytical solution diverges when the perturbation condition $\epsilon_{A,B} \ll |\delta_{A,B}|$ is violated, specifically when the drive is close the qubits' frequencies. Meanwhile, the numerical result shows high, but finite, ZZ rate in these regions.

To further explore possible gate rates, we perform a two-dimensional sweep as displayed in Fig. 7(c). An induced ZZ rate of over 50 MHz can be reached for $\epsilon_A/2\pi = \epsilon_B/2\pi \geq 100$ MHz, and large drive-qubit detuning can be compensated by higher amplitudes to produce a large ZZ rate. Since we can pick the drive frequency independently from the qubit frequencies, this gate scheme is more versatile compared to the previously discussed CR gate.

It is important to investigate gate performance for large qubit-qubit detunings upon scaling up. To this end, we fix qubit A's parameters and vary qubit B's inductive energy as shown in Table II, apply the microwave drive at frequency $\omega_d/2\pi = \omega_B/2\pi + 50$ MHz, then compute the dynamical ZZ rate for varying qubit-qubit detuning $\Delta = \omega_B - \omega_A$. Interestingly, the dynamical ZZ rate shown in Fig. 7(d) is quite high at large detuning $\Delta/2\pi = 900$ MHz, with $|\zeta_{ZZ}|/2\pi > 1$ MHz for $\epsilon_A/2\pi = 200$ MHz, $\epsilon_B/2\pi = 100$ MHz. This promises a short gate time τ_g even for qubits far detuned from each other.

We proceed to simulate the gate performance by calibrating the appropriate gate parameters and computing the fidelity following Eq. (19). In the first step, we estimate the required amplitudes based on the conditional metric R given by Eq. (18), with the qubits now initialized in the superposition state $|+\rangle_A|+\rangle_B$, where $|+\rangle_A = (|0\rangle_A + |1\rangle_A)/\sqrt{2}$. Since the drive frequency is also an independent parameter in this gate scheme, there are more variables to consider. Thus, in order to simplify the calibration, we first simply use a cosine pulse shape as defined by Eq. (7), sweep the gate time τ_g, and vary the drive frequency ω_d. We employ the Nelder-Mead optimization method with the drive amplitudes $\epsilon_{\{A,B\}}$ as free parameters to estimate the best gate fidelity.

For a pair of coupled fluxoniums with parameters listed in Table I and coupling coefficients $\{J_L, J_C\} = \{2, 11.5\}$ MHz, the gate error $1 - \mathcal{F}$ generally decreases with longer gate time τ_g (and correspondingly longer ramping time), as shown in Fig. 7(e). Notably, larger
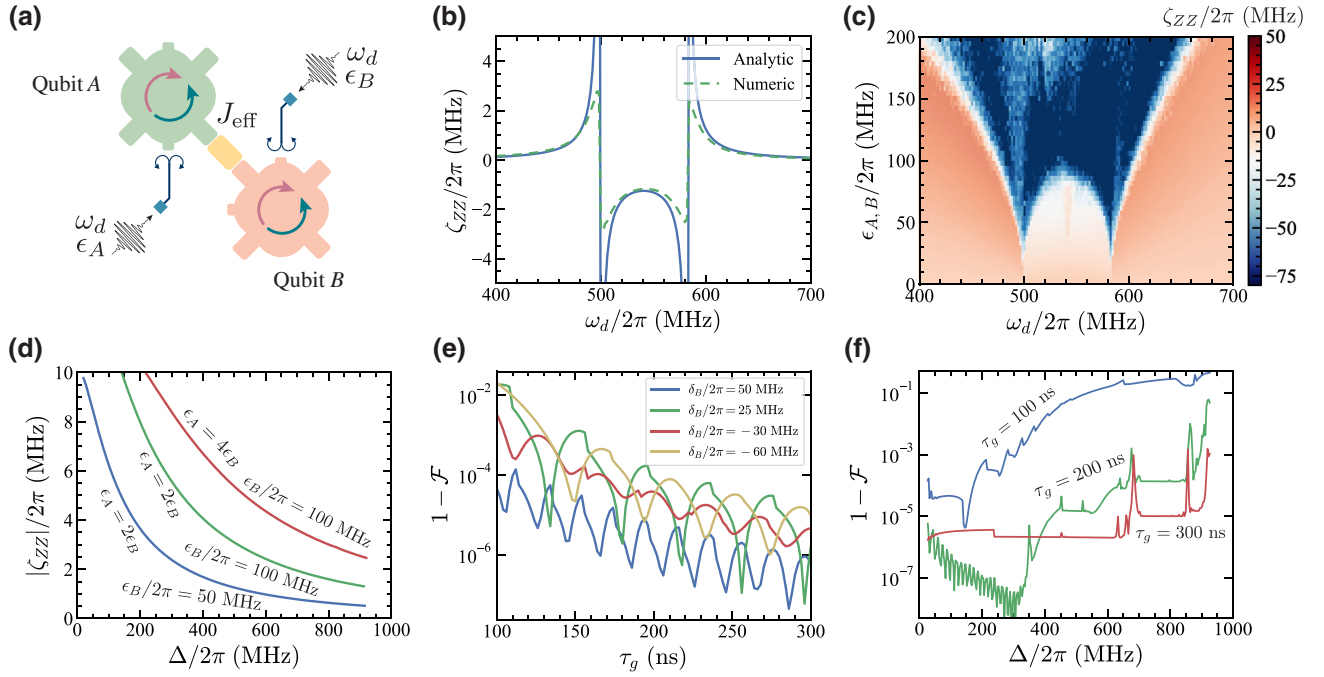
FIG. 7. Differential ac-Stark CZ gate simulation. The coupling coefficients are $\{J_L, J_C\} = \{2, 11.5\}$ MHz, corresponding to an effective exchange interaction rate $J_{eff} \sim 11$ MHz. Qubit parameters with fixed detuning are listed in Table I. Those with varying detuning are listed in Table II. We use $\phi_A = \phi_B$ for all simulations. (a) Gate schematic: microwave tones are applied simultaneously to the qubits off resonantly via individual rf flux lines will induce a dynamical *ZZ* coupling that entangles the qubits. (b) Dynamical *ZZ* rate ζ_{ZZ} with varying drive frequency ω_d for drive amplitudes $\epsilon_A/2\pi = \epsilon_B/2\pi = 10$ MHz. (c) *ZZ* rate for varying drive frequency ω_d and amplitudes $\epsilon_A = \epsilon_B$. (d) *ZZ* rate with varying qubit-qubit detuning for microwave drives applied at $\omega_d/2\pi = \omega_B/2\pi + 50$ MHz. Three sets of amplitudes are chosen: $\{[\epsilon_A = 2\epsilon_B, \epsilon_B/2\pi = 50$ MHz$], [\epsilon_A = 2\epsilon_B, \epsilon_B/2\pi = 100$ MHz$]$, and $[\epsilon_A = 4\epsilon_B, \epsilon_B/2\pi = 100$ MHz$]\}$. (e) Gate error with varying cosine pulse length τ_g, for microwave drives applied at $\omega_d = \omega_B + \Delta_B$, $\Delta_B/2\pi = \{-60, -30, 25, 50\}$ MHz. (f) Gate error for varying qubit-qubit detuning and different gate time $\tau_g = \{100, 200, 300\}$ ns. We use flat-top cosine pulses with ramping time $\tau_{ramp} = \tau_g/2$ for $\tau_g = 100$ ns, and $\tau_{ramp} = \tau_g/3$ for the other gate times. The microwave drives are applied at $\omega_d/2\pi = \omega_B/2\pi + 50$ MHz.

detunings between the drive and the qubit generally correspond to lower gate error. From these results, we attribute the residual gate error to noncommuting single-qubit rotations such as $\hat{X}\hat{I}$ and $\hat{I}\hat{X}$ due to the strong drives. Interestingly, this implies that optimizing the drive frequency and the gate time is important if high-fidelity operation is desired. For example, a 100-ns-long gate has a fidelity as low as approximately 10^{-4} when the pulses are applied at a frequency $\Delta_B/2\pi = 50$ MHz above qubit B.

Finally, we optimize the pulse parameters and evaluate the gate errors for varying qubit-qubit detuning Δ using pulses applied at a frequency 50 MHz above qubit B. For gate time $\tau_g = 100$ ns, we use the ramping time $\tau_{ramp} = \tau_g/2 = 50$ ns, and for $\tau_g = 200, 300$ ns, we use $\tau_{ramp} = \tau_g/3$. The results are shown in Fig. 7(f), with the pulse amplitudes optimized using the Nelder-Mead method at each Δ. For $\tau_g = 100$ ns, we observe an increase in gate error at higher Δ, which can be explained by the lower gate rate, similar to the CR gate case. However, the gate error remains below 10^{-3} up to $\Delta/2\pi = 900$ MHz for 300-ns-long pulses.

A notable source of gate error is finite leakage to higher states due to high-order multiphoton transitions, which manifests as the peaks in Fig. 7(f) (see Appendix F 2). However, since this is typically caused by very large drive amplitudes, the gate error remains below 10^{-2}. It can also be further suppressed by using pulses with lower amplitudes at the cost of longer gate times, as evidenced by the difference between the errors of 200- and 300-ns gates. Thus, we believe that this leakage does not degrade the gate performance significantly. In addition, choosing another drive frequency for the specific qubit parameters should improve the fidelity substantially.

The small coherent gate errors suggest that the fidelity may be limited by decoherence processes. Since the quantum dynamics during the gate only involves the high-coherence computational states, coherence-limited error is expected to be small. As discussed in Appendix F 1, the decoherence-induced error of a 300-ns two-qubit gate is below 10^{-3} for relaxation time $T_1 > 300$ μs and coherence time $T_2 = 2T_1$. For a large-scale fluxonium quantum processor, we expect the average two-qubit gate time to

be ~ 200 ns, and average relaxation time to be approximately 500 μs, resulting in a small average gate error of $1 - \mathcal{F} = 3 \times 10^{-4}$.

One potential hurdle for this type of off-resonant driven interaction is the degradation of coherence times as the drive amplitude increases [78,79], which can be attributed to either unstable electronics, possible interaction with two-level defects [172,173], or an additional noise mechanism in the dressed frame. In the first case, since the qubits are controlled via direct pulses from high-precision AWGs, fluctuation due to *IQ* mixing would be reduced significantly. In the second case, the spectral density of two-level defects in the proposed operating regime has not been rigorously studied, but is likely lower than at the 5-GHz range [53,116]. Future work on the spectroscopy of two-level system defects [172,173] in this frequency range will be needed to confirm the preliminary assessment. Finally, dynamical dephasing can be analyzed and mitigated using advanced techniques such as Floquet theory [174].

VII. FREQUENCY ALLOCATION

A major challenge in engineering superconducting architectures, especially fixed-frequency platforms, is spectral crowding where fluctuations in qubit parameters lead to frequency collisions that degrade the performance of multi-qubit devices and subsequently nanofabrication yield [43]. Our proposed architecture is constructed from fluxonium circuits biased at a fixed external flux to reach high-coherence, so allocating the qubit frequencies in a quantum processor is of central importance in scaling up the platform. In this section, we discuss frequency fluctuation of the computational transition in fluxonium and experimentally feasible dispersion. Based on the gate results in previous sections, we impose a set of frequency constraints and simulate the yield of collision-free large-scale devices.

A. Frequency dispersion of computational states

Superconducting qubit frequencies depend on the tunneling barrier in Josephson junctions, and thus are prone to fluctuation. The degree of randomness is typically characterized by the frequency dispersion σ_f. Although the fluxonium circuit consists of more components compared to transmons, we argue that its frequency dispersion is quite small, so it should scale up more favorably. We treat E_C as a fixed parameter since the capacitive shunt is highly reproducible with modern microwave design and engineering. This has been validated by recent results in transmon studies [44,175]. Since the qubit parameters result in low computational transition frequencies, fluctuations in E_J and E_L correspond to rather small differences in $|0\rangle \rightarrow |1\rangle$ frequencies, as shown in Fig. 8.

Typical junction variations on a device correlate with the positions of the qubits, as the electron-beam angle is
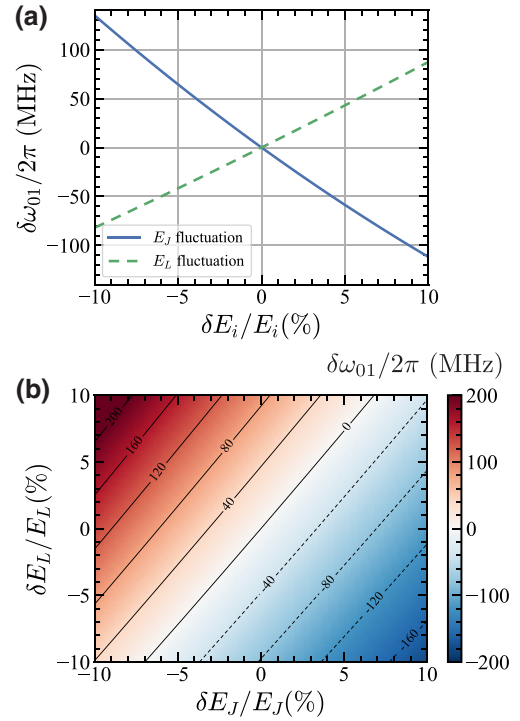

FIG. 8. Frequency dispersion for a fluxonium qubit with parameters $\{E_J, E_C, E_L\} = \{4, 1, 1\}$ GHz. (a) $|0\rangle \rightarrow |1\rangle$ frequency variations resulted from changes in E_L or E_J. (b) Frequency dispersion for both E_L and E_J fluctuations.

not consistent across a big wafer [175], or because the resist thickness is not uniform. In case the superinductor is made from a junction array, this results in E_J and E_L changing in the same way, compensating each other, such that a 2% increase in both parameters corresponds to a frequency shift of only approximately 10 MHz. In addition, variable aging of the metastable tunnel junctions also has the same effect on both E_J and E_L. Hence, systematic frequency variation would be suppressed in fluxoniums.

For random fluctuations of the oxide layer that cause unpredictable changes in E_J and E_L, we consider the parameters separately. With E_J, we can employ a laser annealing technique that has been demonstrated to improve the nanofabrication precision of Josephson junctions to a dispersion of 0.3% [44]. This corresponds to a frequency variation $\sigma_f \lesssim 10$ MHz when only E_J changes. For E_L, if the superinductor is constructed from an array consisting of $N = 100$ junctions [51,83,116], independent fluctuations of individual junctions would reduce the fluctuation in E_L by $\sqrt{N}$ times, or $\delta E_L/E_L \sim 0.2\%$ if each junction fluctuates by 2%. In addition, geometric superinductors have recently been demonstrated to have variation as low as 0.2% as well [92]. This also corresponds to a frequency dispersion $\sigma_f \lesssim 10$ MHz. Therefore, recent advances in Josephson-junction fabrication techniques can be adapted to produce fluxonium devices with frequency dispersion

in the range $\sigma_f \sim 10$ MHz, assuming the worst case of random fluctuations in both E_J and E_L.

B. Frequency constraints and fabrication yield

Spectral crowding leads to frequency collisions of neighboring qubits where control of one qubit affects others. This lowers the probability of successfully fabricating a good multi-qubit device. In the field of nanofabrication, this probability is defined as *yield*. We analyze the yield of our proposed architecture with square-lattice topology in Fig. 1, which has a high number of qubit-qubit connections. Other topologies such as heavy square or heavy hexagon that are used to implement hybrid quantum error correction codes [176] would have fewer connections and subsequently higher yield [44,177].

To avoid collisions, we impose the following constraints on the qubit frequencies, as summarized in Table III. Due to the high anharmonicity of fluxonium in the proposed regime, we consider only the frequencies of computational states.

(a) *High-coherence*: For the qubit to be in the high coherence regime, we target specifically the frequency range from 0.2 to 1.2 GHz. The high relaxation time T_1 is achieved here mainly due to the suppression of dielectric loss at low frequency [53,54].

(b) *Addressability*: To avoid having microwave pulses applied on resonant to qubit i inducing unwanted rotation in a nearest-neighbor qubit j [178,179], we require their $|0\rangle \rightarrow |1\rangle$ transition frequencies to be separated by $|\omega_i - \omega_j|/2\pi \geq 20$ MHz. In addition, we impose an additional constraint to avoid two-photon driving, $|2\omega_i - \omega_j|/2\pi \geq 10$ MHz. This frequency separation is lower since multiphoton processes require higher drive amplitudes. We note that these values are based on previous transmon studies [44], and future experiments on planar fluxonium devices will be needed to pinpoint the lower bound of the constraint.

(c) *High-fidelity entangling gates*: As discussed previously, gate time and fidelity of entangling operations depend on the detuning between the qubit frequencies. Here, we target two-qubit gate errors to be lower than 10^{-2}. To this end, we rely on the gate simulations in Sec. VI and restrict the detuning between the participating qubits' frequencies $|\omega_i - \omega_j|/2\pi$ to be between 20 MHz–1 GHz for both gate schemes. In addition, to avoid inducing two-photon SWAP-like gate [159], we exclude the frequency region $(\omega_i + \omega_j)/2$ from the possible region for driving frequency ω_d. Future work on pulse optimization and advanced calibration of

TABLE III. Frequency collision constraints and definitions. For spectator CR, the drive frequency is on resonance with the target qubit, $\omega_d = \omega_j$.

Constraint	Definition
High-coherence	$0.2 \text{ GHz} \leq \omega_i/2\pi \leq 1.2 \text{ GHz}$
Addressability	$20 \text{ MHz} \leq |\omega_i - \omega_j|/2\pi$
	$10 \text{ MHz} \leq |2\omega_i - \omega_j|/2\pi$
CR gate	$20 \text{ MHz} \leq |\omega_i - \omega_j|/2\pi \leq 1 \text{ GHz}$
CZ gate	$20 \text{ MHz} \leq |\omega_i - \omega_j|/2\pi \leq 1 \text{ GHz}$
	$10 \text{ MHz} \leq |\omega_d - (\omega_i + \omega_j)/2|/2\pi$
Spectator	$20 \text{ MHz} \leq |\omega_d - \omega_k|/2\pi$
	$10 \text{ MHz} \leq |2\omega_d - \omega_k|/2\pi$

gate parameters may reduce the error further, relaxing these restrictions. In such a case, our proposed range can simply be extended to give higher yields.

(d) *Spectator error*: Beyond interaction with qubit j, which participates in an entangling operation, two-qubit gate pulses applied to qubit i can also induce unwanted transitions in a connected qubit k if the drive frequency ω_d is close to its transition frequency ω_k. Since qubit k does not affect the intended operation, this is known as *spectator* error. To avoid collision with spectator qubits, we impose the additional constraints on the drive frequency such that it is sufficiently detuned from the spectating qubits' frequencies, $|\omega_d - \omega_k|/2\pi \geq 20$ MHz and, including two-photon driving, $|2\omega_d - \omega_k|/2\pi \geq 10$ MHz. For the cross-resonance gate, the drive frequency is fixed at the target qubit frequency, $\omega_d = \omega_j$.

The frequency allocation simulation is performed following Ref. [177]. We specify a directed graph based on the square-lattice topology shown in Fig. 1. Each qubit is defined as a node and each pair of qubits is connected via an edge. The orientation of the edge is important for the CR gate, but not for the ac-Stark CZ gate. Then, we find a set of frequencies on these nodes satisfying the conditions defined in Table III. Solution optimization is based on mixed-integer programming, and we use the Gurobi solver with the Pyomo python package [180,181].

We show the yield results based on various qubit-frequency dispersion σ_f in Fig. 9. For the square-lattice topology, the yield based on the ac-Stark effect is considerably higher than the one based on the CR effect since the former does not have a strict constraint on the drive frequency. Even for a large 50×50 cell, the yield is close to unity for frequency dispersion $\sigma_f \leq 40$ MHz.

As the number of qubits in a quantum processor increases, individually optimizing all the frequencies on the chip is resource heavy. Instead, an optimized unit cell is tiled to generate a larger lattice with periodic boundary
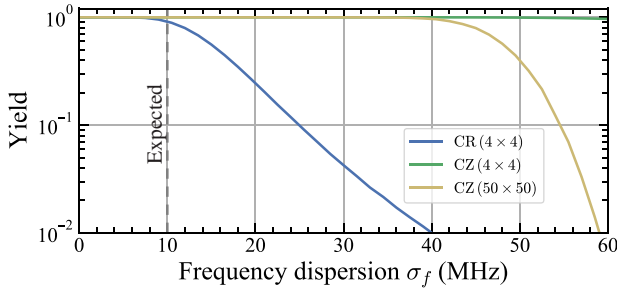
FIG. 9. Fabrication yield with varying qubit-frequency dispersion σ_f for square-lattice topology based on cross-resonance (labeled CR) and differential ac-Stark (labeled CZ) two-qubit gates, with cells consisting of 4×4 and 50×50 qubits. As discussed in the main text, we expect a frequency dispersion of $\sigma_f \sim 10$ MHz if state-of-the-art nanofabrication techniques are employed to construct the processor.

condition. The corresponding yield estimation is given by

$$y = y_{\text{cell}}^{N_{\text{device}}/N_{\text{cell}}}, \qquad (22)$$

where y (y_{cell}) is the yield of the large device (unit cell), and N_{device} (N_{cell}) is the number of qubits in the device (unit cell). Based on the simulation result for size 50×50, a device containing 10^4 fluxonium qubits operated using the ac-Stark CZ gate should have a fabrication yield $y \approx 60\%$ if the average frequency dispersion is $\sigma_f = 42$ MHz, and $y \approx 100\%$ for $\sigma_f < 30$ MHz. Recently, yield simulation in fixed-frequency transmon devices [44] have been successfully fulfilled experimentally, resulting in high-performance quantum processors [182]. This leads us to believe that the flexibility of the ac-Stark CZ gate and the high anharmonicity of the fluxonium qubit shall lead to a high-yield, scalable superconducting platform.

VIII. TOWARD LOGICAL QUBITS

Logical qubits encoded using a QEC code can achieve arbitrarily low error rates as long as the physical error rate is below a certain threshold [39–41]. The local connectivity and high thresholds make surface code [32,47–49] a popular choice for realizing scalable quantum computation [35,36]. In this section, we investigate the performance of the XZZX surface code [80] using fluxonium qubits, as illustrated in Fig. 10. The figure shows the quantum circuit used to measure the stabilizers where an ancilla qubit, initialized in the superposition state $|+\rangle$, is placed at the center of each face. Next, a sequence of CNOT and CZ gates are applied, and finally the ancilla is measured in the X basis. For numerical simulations of the circuit shown in the figure, errors are applied before the gates, after preparation (or reset), before readout, and on idle qubits during these operations.

The error channel for each of these operations is parametrized using the corresponding physical error rate
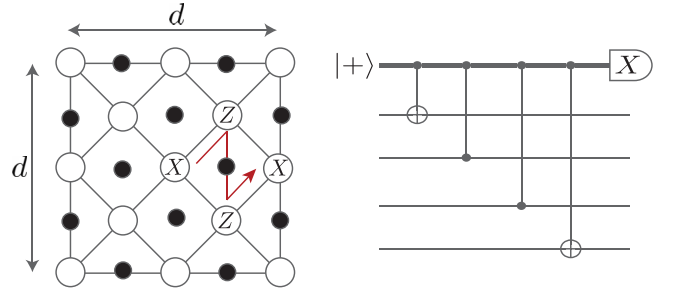

FIG. 10. (Left) Illustration of a regular square XZZX code with distance d where data (ancilla) qubits are shown as open (closed) circles. Each square stabilizer is the multi-qubit Pauli operator $X \otimes Z \otimes Z \otimes X$. The triangular stabilizers on the horizontal boundaries are $X \otimes Z \otimes X$, and the ones on the left (right) vertical boundary are $Z \otimes Z \otimes X$ ($X \otimes Z \otimes Z$). The order in which the qubits are coupled to the ancilla at the center of each face is indicated by the red arrow. (Right) Stabilizer measurement circuit for the XZZX code. The ancilla is prepared in state $|+\rangle$, then coupled to data qubits with CNOT and CZ gates, and finally measured in the X basis.

ε listed in Table IV. We estimate the physical error budget as follows. The readout and reset error values are taken from state-of-the-art experimental implementation in Ref. [56]. The measurement time of fluxonium using quantum-limited parametric amplifiers is 200 ns. Since the reset is performed using feedback, and in principle can be done by heralding [124], we assume its fidelity is limited by the readout fidelity, and state initialization in the physical qubits can be done instantaneously. We expect the average single-qubit gate time on the chip to be 10 ns, and two-qubit CZ gate time to be 200 ns. From these assumptions, we can compute the decoherence-limited gate fidelity, given by Eq. (F2) in Appendix F 1. These are lower than the average coherent gate errors. We also include idle errors in nonparticipating qubits due to decoherence during the operations of participating qubits. Non-Markovian noise sources such as leakage, crosstalk, and correlated errors due to quasiparticles are not taken into account.

TABLE IV. Expected average Pauli errors in the processor for different average relaxation times T_1.

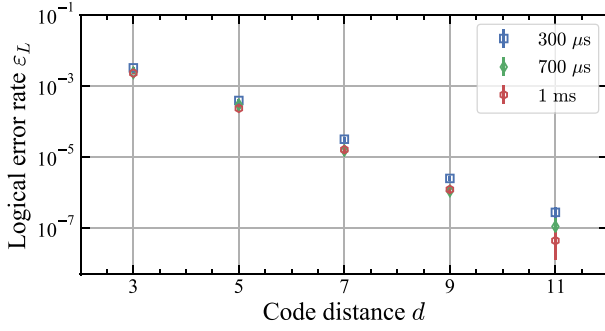| Operation	Error ε		
	300 μs	700 μs	1 ms
2Q CZ	5.3×10^{-4}	2.3×10^{-4}	1.6×10^{-4}
1Q H	1.1×10^{-5}	4.7×10^{-6}	3.3×10^{-6}
Readout	10^{-2}	10^{-2}	10^{-2}
Reset	10^{-2}	10^{-2}	10^{-2}
Idle (2Q)	2.2×10^{-4}	9.5×10^{-5}	6.6×10^{-5}
Idle (1Q)	1.1×10^{-5}	4.7×10^{-6}	3.3×10^{-6}
Idle (R)	2.2×10^{-4}	9.5×10^{-5}	6.6×10^{-5}

FIG. 11. Logical error rates for varying surface code distance d with Pauli errors listed in Table IV. We perform MC simulations involving d rounds of faulty syndrome measurements using the circuit in Fig. 10, on a $d \times d$ XZZX code, also illustrated in the figure. In order to extract error rates in the range shown, $\{1.8 \times 10^5, 1.8 \times 10^5, 1.8 \times 10^6, 1.8 \times 10^7, 10^8\}$ MC simulations are performed for $d = \{3, 5, 7, 9, 11\}$.

To model single-qubit noise, the errors are chosen uniformly at random from the set $\{X, Y, Z\}$, each with probability $\varepsilon/3$ such that the total error probability ε corresponds to the values listed in Table IV. For the two-qubit CZ gate, errors are randomly and uniformly chosen from the set $\{I, X, Y, Z\}^{\otimes 2}/(I, I)$ each with probability $\varepsilon/15$ so that ε corresponds to the error probability for the CZ gate in Table IV. The CNOT gate is applied by sandwiching the CZ gate between two Hadamards, so the error channel for CNOT is composed of error channels of two Hadamards and one CZ.

We run Monte Carlo (MC) simulations for a $d \times d$ XZZX code for varying d, using the depolarizing noise described above for different qubit relaxation times T_1. In each MC simulation, all the stabilizers of the code are measured for d rounds and error correction is performed using a minimum-weight perfect-matching decoder [36,80,183, 184]. Logical error rate is recorded as the ratio of number of MC simulations with a logical error and the total number of MC simulations. Figure 11 shows the numerically obtained logical error rates ε_L as a function of code distance d. We find that ε_L decreases exponentially with d, which indicates that the physical error rates of these operations are below thresholds. In addition, the low logical error rate $\varepsilon_L \sim 10^{-7}$ at code distance $d = 11$ promises reduced resource overhead upon scaling up.

Interestingly, Fig. 11 shows that the logical error rate ε_L is largely independent of the relaxation time for small code distance d. This is because the dominant sources of noise in Table IV are ancilla readout and reset errors, $\varepsilon = 1\%$, which do not depend on qubit relaxation time. This implies that readout error might be the limiting factor in future fluxonium quantum processors. Although numerically estimating the readout fidelity for fluxonium qubits is outside the scope of this work, we hope that our result will stimulate further research in this direction.

IX. THE ROADMAP FORWARD

We have thus far analyzed the advantage of the proposed fluxonium processor by positing certain features deduced from transmon experimental studies. Moving forward, we envision a number of experimental developments needed to realize the proposed architecture and achieve the anticipated performance. These can be classified into four complementary cardinal directions, as shown in Fig. 12. They can be investigated independently in principle, but a *co-design* process will bring up solutions more efficiently. While the main goal is to foster and accelerate fluxonium research, we note that exploring these ideas will also advance the frontiers of superconducting qubit technologies and provide further insights into quantum electrodynamics of complex systems. These crucial steps are listed as follows.

A. Fabrication

(a) *Frequency dispersion.* Although variations in junction parameters have been rigorously characterized recently [44,175,186], side-by-side probing of superinductors and small tunneling junctions corresponding to $E_L \sim [0.5 - 1.6]$ GHz and $E_J \sim 4$ GHz remains to be done. Dispersion and correlations of their normal resistance values are required to pinpoint the expected frequency dispersion σ_f. Variable aging of the tunnel junctions is another critical bit of information for designing large-scale devices.
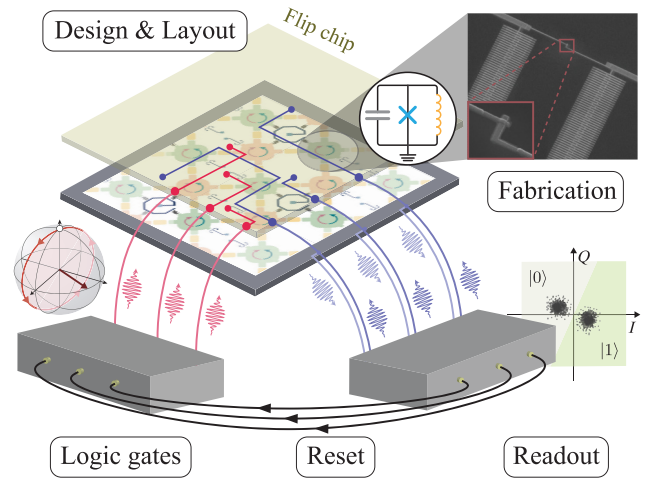

FIG. 12. Directions toward the high-performance fluxonium quantum processor. The research activities are classified into complementary thrusts, which can be carried out preferably in a co-design process. Achieving the performance anticipated in a future device will require advances in fabrication, readout and reset, logic gates implementation, and design and layout engineering. The SEM images show a fluxonium qubit with the superinductor constructed using a bridge-free fabrication technique [185].

Notably, while fluxonium is resilient to fabrication imprecision, novel protected qubits are often sensitive to the symmetry of the device parameters, and will therefore inherit valuable technologies from this line of research.

(b) *Superinductor technology*. Investigations and improvements in superinductor technology are relatively sparse, although it plays an essential role in novel platforms such as the $\cos(2\hat{\varphi})$ [187], the $0 - \pi$ [188], and the bifluxon [189] qubits. So far, resonators made from superinductors have quality factors of up to $Q \sim 10^5$ [88,190], much lower than their coplanar waveguide counterparts. New materials and design strategies to improve their quality, footprint, and reproducibility will add crucial components into the toolbox used to construct robust fluxonium and novel protected qubits. As the proposed regime is sensitive to quasiparticles in the superinductors, research steps should include characterization of the robustness of the element against this noise source, following the developmental trajectory of grAl devices [87,110,191,192].

(c) *Flip-chip technology*. Although small-scale planar devices will work well in the near future, integration of through-Si vias and flip-chip modules is required to increase the qubit count to an ever higher number. To the best of our knowledge, there is currently no fundamental roadblock in aligning current flip-chip technology [193–196] with fluxonium qubits. Progress on this front will streamline the advances in quantum information processing with fluxonium architectures from blueprint to large-scale devices.

B. Readout and reset

(a) *Non-QNDness*. Qubit transitions induced by resonator photons in fluxoniums is currently not well understood, despite recent progress in grAl devices [56,57]. As our proposed parameters are in a different regime, it is a critical to study this effect, possibly with a quantum trajectories experiment to measure the transition rates between relevant eigenlevels when the number of resonator photons increases. Multiple resonators can be used to probe the evolutions of all qubit states simultaneously. This shall allow us to better understand the dynamics and circumvent non-QND processes during the dispersive interaction. As spurious effects have been rigorously identified only recently in transmon devices using resource-intensive numerical simulation [197], we expect similar approaches can also be used to investigate the physics in fluxonium systems in the near future.

(b) *Advanced readout analysis*. As machine-learning techniques have been shown to improve state discrimination in multitransmon devices [198,199], similar approaches can be used to improve the readout fidelity in a fluxonium processor.

(c) *Noise identification, analysis, and mitigation*. High-fidelity readout will enable advanced noise spectroscopy techniques such as deep learning [200] to quantify decoherence rates attributable to the environmental baths. Notably, different transitions in fluxonium are susceptible to decoherence mechanisms such as dielectric loss and quasiparticle tunneling differently. Thus, the qubit can be used as a probe for spatial and temporal correlations corresponding to various noise sources, such as the recent work reported in Ref. [201]. The results can be leveraged to design and fabricate circuitry more resilient to decoherence.

(d) *Multiplexed readout*. After achieving high readout fidelity in individual qubits, multiplexing the measurement of many qubits will likely be straightforward. On the other hand, parallel exploration of the differences between individual and multiplexed readout will accelerate the progress in this direction. We note that although we propose multiplexing the readout of four fluxoniums at a time in this work, a higher number of qubits can be measured at the same time via a single readout bus due to the broad range of finite dispersive shift with respect to resonator frequency.

(e) *Active reset optimization*. Although high-fidelity QND readout allows state preparation by heralding or feedback [56,58,124–126], active initialization by way of microwave driving [54,202,203] will help shorten the execution time of algorithmic quantum circuits or error correction cycles. Optimizing such a technique will further improve the performance of the processor.

C. Design and layout

Upgrading to large-scale devices will require transformative integration of the proposed components into a cross-pollination between fluxonium and flip-chip technology [193–196]. However, we note that near-term small-scale experiments utilizing charge driving or capacitive coupling in planar chips will still perform well at the expense of higher design and operational complexity [204]. As a result, developmental footsteps may correlate with varying degrees of overhead, with proof-of-concept research possibly having non-scalable components.

(a) *Planar device*. First, planar chips consisting of single qubits coupled to co-planar waveguide resonators can be used to benchmark readout fidelity and improve coherence times, in a co-design process together with the fabrication thrust. Charge

driving can be employed to manipulate qubit states. The tradespace consisting of qubit designs and fabrication advances can be optimized to achieve the best average coherence times, with scalability as the central feature.

(b) *Novel microwave components*. In the next steps, the emphasis is to incorporate functional components without degrading coherence. Integration of diplexed flux control will help reduce the footprint of microwave lines. To this end, on-chip diplexers placed near the launching pads can be designed to combine the dc bias with rf signal for each qubit. We note that the future fluxonium device is inevitably susceptible to the compromise between fast control and isolation from the noisy environment. Development of low-frequency filters [205] or circulators [206–209] will be required to break this trade-off. Recently, combined *Z* and *XY* flux control lines were used to perform fast high-fidelity operations in a 2D fluxonium device [65], making an important step forward in this direction.

(c) *Inductive coupling*. Realizing an inductive coupling with $L_M > 100$ pH as part of the multipath coupling scheme will be the stepping stone for future devices with low *ZZ* crosstalk and fast entangling gates, as discussed in Sec. V. This also helps reap the maximal benefits from multi-fluxonium devices. Geometric mutual inductance [210] would likely be too small. Sharing a common section of the superinductors [103] is the most direct method. The best approach from a scalability perspective is to implement an inductive bus similar to the resonator bus in transmon architectures [119,157], which will induce an effective transverse coupling. Another fluxonium qubit mode remaining primarily in its ground state can fulfill the role of such a coupling element, resembling the architectures introduced in Refs. [154,211].

(d) *Flip-chip integration*. Once the proposed components have been successfully incorporated and demonstrated in planar devices, their integration into flip-chip modalities will be straightforward [212]. Such developments must jointly address the aforementioned challenges and at the same time shed light on emerging superinductance, rf flux control, and inductive coupling technologies.

(e) *Quasiparticles mitigation*. Recent experiments in superconducting devices have established the importance of shielding [109,110,192,213] and filtering [106,108] in suppressing detrimental effects from quasiparticles. In addition, vortex [214] and phonon [215] trappings, device material and geometry engineering [216,217], and dynamical techniques [218] have been found to be effective in reducing quasiparticles. Notably, Ref. [219] reports

stable periods during which no quasiparticle is found in the system, which gives hope to fault-tolerant operations using superconducting qubits. Adaptation of these techniques in fluxonium research will play a crucial role in implementing devices with ever better performance.

D. Logic gates

(a) *Single-qubit control*. As shown in Sec. IV, it is possible to operate microwave gates as fast as a few nanoseconds with high fidelity. It is thus interesting to benchmark the performance of single-qubit control as we progress on the designs of various chip components while maintaining sufficient isolation of the qubit from the noisy environment. As mentioned above, breaking the trade-off between fast control and long coherence times may require the development of low-frequency on-chip quantum filters or nonreciprocal components. Meanwhile, a gradiometric design was reported to help stabilize the external flux over long periods of time [192]. This work also introduces a practical technique to initialize a large number of qubits at the sweet spots using a uniform magnetic field.

(b) *Optimizing two-qubit gates*. Since the *ZZ* crosstalk can be completely cancelled by design, stronger coupling between qubits will allow faster gates and subsequently higher fidelity. This leads to lower drive amplitude required to achieve a target gate rate, negating possible dynamical dephasing effects. Utilizing optimal control algorithms such as the gradient ascent pulse engineering (GRAPE) method [220,221] is expected to result in shorter gate times and better fidelity as well. Finally, identifying and mitigating dynamical dephasing at the targeted operating frequency using advanced techniques such as the Floquet framework [222,223] will lead to more robust operations.

(c) *Other multi-qubit gates*. In this work, we focus on the analysis of two types of efficient entangling gates that are frequently used in NISQ applications and quantum error correction encoding. As we have shown that the qubits can be modeled effectively using spin systems, we expect other gate types to be compatible with the proposed architecture. Specifically, we believe that it will be valuable to explore the performance of the fermionic simulation gate family [224] using microwave in this platform.

(d) *Control stack*. In superconducting qubits, quantum operations are typically performed by controlling a microwave setup using increasingly advanced software, the combination of which is generally referred to abstractly as the *control stack*. Since the discussed

CZ gate is sensitive to both amplitudes and phases of the applied microwave tones, stabilizing the drifts of the control signals will play a central role in improving the performance of the processor. In parallel to benchmarking the gate performances at the physical qubits level, we can compare the stability of the control stack working at low frequency versus the more resource-intensive stack for generating microwave pulses at 5-GHz range. Scaling up to large-scale devices will likely involve integration of the microwave control hardware at cryogenic temperature [225]. Similar breakthroughs in microwave electronics' targeting operations at the approximately 1-GHz frequency range with smaller footprints will provide a route toward robust and scalable quantum control.

(e) *Quantifying crosstalk.* As measured in Ref. [152], microwave crosstalk is generally reduced at lower frequency, attributable to better impedance matching and the disappearance of box modes below 5 GHz. It is thus interesting to identify and characterize the main sources of crosstalk in the proposed frequency regime. We also note that since the qubits can be designed to have sufficient detunings, effects from driving neighboring qubits can be further suppressed. Finally, the remaining crosstalk can be tracked and compensated efficiently if we have a robust control stack [72].

(f) *Co-design process.* In near-term small-scale experiments, single- and multi-qubit operations can be carried out without full integration of all the components in the blueprint. For example, devices comprising capacitive couplings and/or charge driving will be sufficient to characterize performance of the gate and compare with theoretical predictions for immediate feedback and improvement [204]. Intertwined in these test experiments are additions of emerging techniques such as flux driving. This co-design process will help ensure steady enhancement of the operations. Stabilizing both flux bias and rf response over long periods of time will be made into a usual routine.

(g) *Quantifying and minimizing errors upon scaling up.* Optimizing the performance of near-term devices will nucleate and foster the development of large-scale processors. Operating these chips will likely involve advanced control stacks that are able to calibrate the optimal parameters autonomously, taking into account spectator errors and residual imperfections in the device. The varying degree of resource overhead and scaling complexity can be empirically quantified at this stage. Another important task is to measure correlated noise using techniques such as non-Markovian tomography [226], and to find the diamond norm using gate set tomography [227], which can be used to rigorously estimate fault-tolerant thresholds [228].

X. SUMMARY

We have discussed the blueprint for a novel architecture based on fluxonium qubits with excellent scaling potential. We show from first principles that the qubits, biased at half-integer flux quantum, would operate as small-footprint fixed-frequency quasi-two-level systems. Forming the backbone of the processor, the qubits in this work have practical parameters and can be fabricated following standard procedures. They are measured dispersively using individual resonators coupled to a common bus, controlled in diplexing fashion, with single-qubit gates in the range of 10 ns having intrinsic errors below 10^{-6} across the computational frequency bandwidth of nearly 1 GHz. Both readout and control crosstalk are expected to be small. The reduced design complexity of these components promises higher resource efficiency in large-scale devices. The multipath coupling approach negates the static ZZ rate completely, while allowing a sufficient exchange coupling rate between the computational states.

We numerically demonstrate fast, high-fidelity two-qubit entangling gates based on the cross-resonance and the differential ac-Stark effects, with gate errors consistently below 10^{-2} for the entire range of proposed qubit parameters, significantly relaxing the frequency allocation constraints in multi-qubit devices with high connectivity. Since the gate schemes are based on an exchange interaction between high-coherence computational states, errors due to decoherence are expected to be low. Notably, our gate simulations are based on a nominal qubit-qubit exchange interaction rate and simple pulses. Future work to optimize the performance of these gates should further improve the fidelity under more stringent conditions, such as large qubit-qubit detuning. Our simple spin model describes the coupled system with excellent consistency, which should initiate more interest in future fluxonium devices.

After discussing practical frequency dispersion of the computational transition expected from recent empirical studies, we explore the platform's scalability by simulating the fabrication yield. Specifically, for a large-scale device consisting of ten thousands of qubits arranged into a square lattice as shown in Fig. 1, we estimate a yield close to unity for frequency dispersion expected from state-of-the-art nanofabrication technology. This allows scaling of the platform to a high number of physical qubits without sacrificing their performance, streamlining the implementation of practical quantum algorithms, and quantum error correction codes. Assuming negligible errors due to non-Markovian noises, we show the exponential suppression of the logical error rate using the XZZX surface code for relatively modest coherence times. The result also reveals

the importance of achieving high fidelity in readout and initialization in fluxonium.

To provide a potential route towards realizing the proposed architecture, we consider a practical roadmap consisting of four complementary directions, each with its own activities and milestones. As experimentalists having to design, characterize, and optimize quantum operations in NISQ devices, we hope that the results and perspectives presented in this paper will, on one hand, hasten further research and development efforts on fluxonium-based quantum architectures, and, on the other hand, motivate similar scalability studies of novel superconducting platforms such as the $\cos(2\hat{\varphi})$ [187,229–233], the bifluxon [189], and the $0 - \pi$ [188,234–237] qubits.

ACKNOWLEDGMENTS

APPENDIX A: DECOHERENCE ANALYSIS

Dielectric loss: The energy relaxation rate for dielectric loss follows the Fermi golden rule as [53,54,116]

$$\Gamma_{01}^{\text{diel}}(\omega_{01}) = \frac{\hbar\omega_{01}^2}{4E_C Q_{\text{diel}}} |\langle 0|\hat{\varphi}|1\rangle|^2 \left[\coth\left(\frac{\hbar\omega_{01}}{2k_B T}\right) + 1 \right].$$

We extract the effective dielectric loss quality factor from transmon and resonator experiments, $Q_{\text{diel}} = 5 \times 10^6$, corresponding to a loss tangent of $\tan\delta_{\text{diel}} = 2 \times 10^{-7}$. For a transmon, this would translate to an energy relaxation time $T_1 = Q/\omega_{01} \approx 160 \, \mu s$ for $\omega_{01}/2\pi = 5$ GHz. The effective temperature of the qubit is assumed to be $T = 20$ mK.

Quasiparticle tunneling: The energy relaxation rate for quasiparticle tunneling across a Josephson junction follows [114,115]

$$\Gamma_{01}^{\text{qp}}(\omega_{01}) = \left| \langle 0| \sin\frac{\hat{\varphi}}{2}|1\rangle \right|^2 \times \frac{8E_J}{\pi\hbar} x_{\text{qp}} \sqrt{\frac{2\Delta_{\text{Al}}}{\hbar\omega_{01}}}, \qquad \text{(A1)}$$

where Δ_{Al} is the superconducting gap for aluminum, and x_{qp} is the quasiparticle density normalized by the density of Cooper pairs.

Since the matrix element is zero for tunneling across the small junction at the symmetric flux bias [116], only the quasiparticles in the inductor affect energy relaxation. For

an array of junctions, the rate can be summed up from individual tunneling events across each junction with index β as [53,115],

$$\Gamma_{01}^{\text{qp}}(\omega_{01}) = \sum_{\beta=0}^{M+1} \left| \langle 0| \sin\frac{\hat{\varphi}_\beta}{2}|1\rangle \right|^2 \frac{8E_{J,\beta}}{\pi\hbar} x_{\text{qp}} \sqrt{\frac{2\Delta}{\hbar\omega_{01}}}$$

$$\approx \left| \langle 0|\frac{\hat{\varphi}}{2}|1\rangle \right|^2 \frac{8E_L}{\pi\hbar} x_{\text{qp}} \sqrt{\frac{2\Delta}{\hbar\omega_{01}}}. \qquad \text{(A2)}$$

We use $x_{\text{qp}} = 5 \times 10^{-9}$, which corresponds to $T_1 = 1$ ms at absolute temperature for a fluxonium qubit as reported in Ref. [55]. The effect of temperature following detailed balance is included Ref. [104], assuming qubit temperature $T = 20$ mK.

The energy relaxation rates are computed for different qubit parameters and added up to give the result shown in Fig. 2(d).

Thermal photon dephasing: We follow the thermal photon dephasing rate given as [241]

$$\Gamma_\phi^{\text{th}} = \frac{\kappa_{\text{tot}}}{2} \text{Re} \left[\sqrt{\left(1 + \frac{i\chi_{01}}{\kappa_{\text{tot}}}\right)^2 + \frac{4i\chi_{01}n_{\text{th}}}{\kappa_{\text{tot}}}} - 1 \right]. \quad \text{(A3)}$$

In the simulation, we use resonator linewidth $\kappa_{\text{tot}}/2\pi = 2$ MHz and resonator temperature $T = 50$ mK, which determines the average thermal photon number as $n_{\text{th}} = [\exp(\hbar\omega_R/k_B T) - 1]^{-1}$.

Radiative (Purcell) loss: We use the following procedure in HFSS to estimate the relaxation rate of the qubit through coupling to the readout resonator, using a sample chip design (not shown). The same approach has been used to predict radiative decay rates in our current transmon processors with reasonable success. Readers interested in other methods may prefer the procedures described in Refs. [116,121].

First, we specify the launcher (blue interconnect in Fig. 1) connecting the readout bus to external circuitry to be a 50-Ohm lump port. The readout resonator's length is designed to give the targeted frequency. It is then coupled to the bus, with their physical separation varied to tune the effective resonator linewidth to be $\kappa/2\pi \sim 2$ MHz. This is computed using the simulated Q values in HFSS.

Then, the antenna pads are designed and simulated to tune the effective charging energy $E_C = 1$ GHz and coupling coefficient $g/2\pi = 100$ MHz with eigenmode solver, using a lump inductance boundary condition. After fixing the geometry for all conductive components, the inductance value is swept such that the eigenfrequency of the lump device's fundamental mode matches the targeted frequency corresponding to the proposed qubit parameters. The simulation extracts the finite Q of this mode.

We compute the matrix elements of the corresponding *LC* circuit by setting the Josephson term in Eq. (1) to 0,
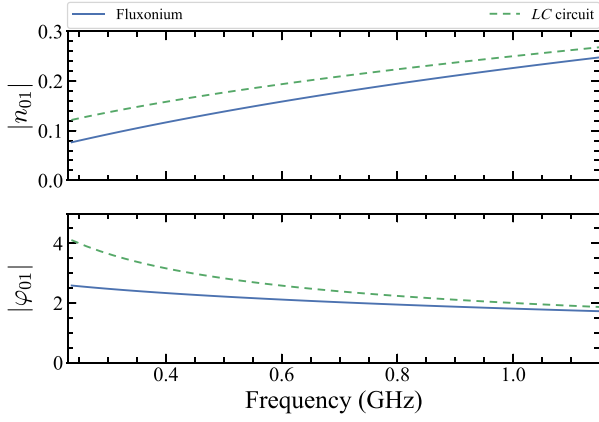
FIG. 13. Comparison between the charge (phase) matrix elements of fluxonium qubits and those of an LC circuit. The fluxonium parameters are the same as proposed in the main text. The LC circuit is given the same charging energy $E_C = 1$ GHz, and its inductive energy E_L is tuned to match the fluxonium's frequency.

and compare them with those of the fluxonium qubit in the proposed regime (see Fig. 13). We simulate $Q \geq 10^7$ for the proposed frequency range. Normalization using the matrix elements gives an estimation of Purcell-limited T_1 greater than 2 ms, well above the expected values shown in Fig. 2(d).

Similarly, Purcell loss of the $|0\rangle \rightarrow |3\rangle$ transition corresponding to qubit parameters $\{E_J, E_C, E_L\} = \{4, 1, 1\}$ GHz can be estimated. However, it is time consuming when we want to modify the readout frequency, and should be used as the final step to check for consistency instead. Alternatively, a faster estimation using the dispersive relation $\Gamma_q = (g/\Delta)^2 \kappa$ can be employed here. This method tends to overestimate the decay rates, but it is reasonably precise close to resonant condition [121], while the higher transitions can be assumed similar to harmonic oscillator modes. Following this approach, a detuning $\Delta/2\pi = 700$ MHz is sufficient to keep $T_\phi \geq 2$ ms, assuming a qubit temperature of $T_{\mathrm{eff}}(\omega_{03}) = 50$ mK. The excitation rate of the $|1\rangle \rightarrow |4\rangle$ transition is substantially smaller for $|4\rangle \rightarrow |1\rangle$ rate similar to that of $|3\rangle \rightarrow |0\rangle$ due to its higher frequency, so the resonator detuning from it can be as small as 200 MHz. Subsequently, the optimal readout frequency for qubit parameters $\{E_J, E_C, E_L\} = \{4, 1, 1\}$ GHz should be between 8 and 9 GHz, depending on the effective temperatures of the qubit and the resonator, to minimize dephasing effects on the qubit due to resonator photons.

APPENDIX B: TIME-DEPENDENT HAMILTONIAN FOR FLUX-DRIVEN GATES

In the presence of a time-dependent external flux threading the loop formed by the superinductor and the small junction in a fluxonium circuit, the correct Hamiltonian is given by Eq. (1) with $\varphi_{\mathrm{ext}} = \varphi_{\mathrm{ext}}(t)$ being a time-dependent function in the inductive term $\frac{1}{2}E_L[\hat{\varphi} + \varphi_{\mathrm{ext}}(t)]^2$ [81,82]. This form corresponds to the choice of the so-called irrotational degrees of freedom. Let $\varphi_{\mathrm{ext}}(t) = \varphi_{\mathrm{ext},\,0} + \delta\varphi_{\mathrm{ext}}(t)$, where $\varphi_{\mathrm{ext},\,0}$ is the static part of the external flux (usually, $\varphi_{\mathrm{ext},\,0} = \pi$) at which the qubit is parked between gate operations and $\delta\varphi_{\mathrm{ext}}(t)$ is the time-dependent correction. Then, we can write the inductive term as

$$
\frac{1}{2}E_L[\hat{\varphi} + \varphi_{\mathrm{ext}}(t)]^2 \\
= \frac{1}{2}E_L[\hat{\varphi} + \varphi_{\mathrm{ext},\,0}]^2 + E_L\delta\varphi_{\mathrm{ext}}(t)\hat{\varphi} + f(t), \quad \text{(B1)}
$$

where $f(t)$ is a time-dependent function in front of the identity operator, which does not affect qubit dynamics and can be disregarded. The second term in the r.h.s. of Eq. (B1) is equivalent to the driving Hamiltonian $\hat{\mathcal{H}}_d/h = \mathcal{E}(t) \times \hat{\varphi}$, which has been used throughout the paper to model gate operations with a flux drive.

Alternatively, the fluxonium Hamiltonian is often written with φ_{ext} placed in the Josephson term according to $-E_J \cos[\hat{\varphi} - \varphi_{\mathrm{ext}}(t)]$. For some time-dependent wave function $\psi(\varphi, t)$ whose evolution follows the Schrödinger equation $i\hbar d\psi/dt = \hat{\mathcal{H}}\psi$, this change of the Hamiltonian amounts to the time-dependent translation transformation

$$
\psi(\varphi, t) = \hat{\mathcal{U}}(t)\psi'(\varphi, t), \quad \text{(B2)}
$$

where the unitary operator is given by

$$
\hat{\mathcal{U}}(t) = \exp\left[i\hat{n}\varphi_{\mathrm{ext}}(t)\right]. \quad \text{(B3)}
$$

The Hamiltonian that describes the time evolution of the transformed wave function $\psi'(\varphi, t)$ according to $i\hbar d\psi'/dt = \hat{\mathcal{H}}'\psi'$ is given by

$$
\hat{\mathcal{H}}' = \hat{\mathcal{U}}^\dagger\hat{\mathcal{H}}\hat{\mathcal{U}} - i\hbar\hat{\mathcal{U}}^\dagger\frac{d\hat{\mathcal{U}}}{dt}. \quad \text{(B4)}
$$

Thus,

$$
\hat{\mathcal{H}}'/h = 4E_C\hat{n}^2 - E_J\cos(\hat{\varphi} - \varphi_{\mathrm{ext}}) + \frac{1}{2}E_L\hat{\varphi}^2 + \frac{\hat{n}}{2\pi}\frac{d\varphi_{\mathrm{ext}}}{dt}. \quad \text{(B5)}
$$

This is the correct form of the fluxonium Hamiltonian in the presence of a generic time-dependent external flux in the Josephson term. The last term ($\propto \hat{n}d\varphi_{\mathrm{ext}}/dt$) is absent only when φ_{ext} is time independent. We note, however, that even for time-dependent fluxes, this residual term is often small and can be neglected. To find the small parameter

controlling such an approximation, we note that this term can be combined with the charging energy as

$$4E_C \left(\hat{n} - \frac{1}{16E_C} \frac{d(\varphi_{\text{ext}}/\pi)}{dt} \right)^2, \tag{B6}$$

so the time derivative of φ_{ext}/π has to be compared with $16E_C$. As an example, let us consider flux-tunable entangling gates, where a typical change in φ_{ext} is smaller than $\pi/10$ [62,63]. For $E_C \sim 1$ GHz, we find that this change has to occur in a time scale much slower than 10 picoseconds for the approximation to be valid. Even for fast flux nonadiabatic gates, it occurs on the time scale of nanoseconds, thus the omission of the last term is justified.

We note that once the term describing the time-dependent part of the external flux in the Hamiltonian has been singled out as $\mathcal{E}(t) \times \hat{\varphi}$, see Eq. (B1), the remaining static part $\varphi_{\text{ext}, 0}$ can be moved between the inductive and Josephson terms by the time-independent gauge transformation without any concern about missing additional terms.

APPENDIX C: SINGLE-QUBIT GATE SIMULATION

We can estimate the required pulse amplitude to rotate the qubit by a certain angle as follows. When subjected to an on-resonant in-phase radiation tone with amplitude $\mathcal{E}_I(t)$, a two-level system with dipole moment η undergoes a Rabi oscillation with frequency equal to $\Omega_r = \eta \mathcal{E}_I(t)$, assuming the rotating wave approximation in the interaction frame. Thus, the qubit vector is rotated by an angle equal to $2\pi \int_0^{\tau_g} \eta \mathcal{E}_I(t) dt$ for gate time τ_g. For a square pulse with constant amplitude $\mathcal{E}_I(t) = \epsilon_d$, a 2π rotation is realized when $\epsilon_d = (\eta \tau_g)^{-1}$, which we use to normalize the drive amplitude for other angles as well. In this work, we focus on π rotations, corresponding to an amplitude factor of 0.5. For the cosine pulse defined in Eq. (7), the time integration reads $\int_0^{\tau_g} \mathcal{E}(t) dt = \epsilon_d \tau_g / 2$, so the amplitude condition for 2π rotation is $\epsilon_d = (\eta \tau_g / 2)^{-1}$. From this relation, we note that the drive amplitude ϵ_d has the unit of frequency.

To simulate a π pulse, the single-qubit gate pulse is first set to these default values: amplitude factor = 0.5, DRAG coefficient $\lambda = 0$, and detuning $\omega_d - \omega_{01} = 0$. Ideally, this corresponds to a π rotation that flips the qubit around X or Y axis, depending on the coupling degree of freedom [cf. Eq. (2)]. In practice, this leads to rotation error for short gate times as shown in Fig. 4.

To correct for the effect from fast rotating terms, we attempt to vary the relative amplitude of the pulse, then the DRAG coefficient λ, and finally the drive-qubit detuning. While keeping the other pulse parameters fixed, we compute the respective gate errors in each sweep. As shown in Fig. 14, turning on a small negative DRAG coefficient suppresses most of the error, while the other approaches only
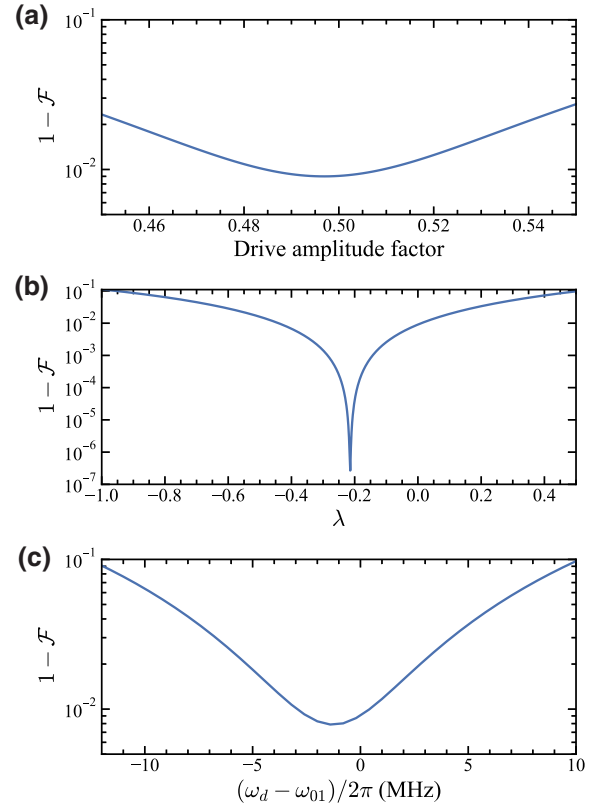

FIG. 14. Single-qubit gate fidelity simulation results for charge driving with $\tau_g = 10$ ns and varying (a) relative drive amplitude factor, (b) DRAG coefficient λ, and (c) drive-qubit detuning. Each sweep is executed with other parameters set to default values: amplitude factor = 0.5, $\lambda = 0$, $\omega_d - \omega_{01} = 0$.

suppress it within one order of magnitude. This validates the intuition that adding a DRAG quadrature component would reshape the spectral profile of the pulse, improving the precision of the operation. To optimize the gate, we use all three parameters as free variables and minimize the error using the Nelder-Mead method.

APPENDIX D: HAMILTONIANS OF COUPLED CIRCUITS

In this Appendix, we derive the Hamiltonians describing the system of two fluxonium circuits coupled via a mutual circuit element as shown in Fig. 15. Our approach follows the *node flux* method [153] and utilizes matrix notations [242]. Here, the node fluxes are denoted as ϕ_n, the branch fluxes as Φ_n, and the normalized flux across a branch as φ_n. The circuit variables have subscripts A and B, and the coupling element has subscript M. We note that the node fluxes as defined here are equal to the branch fluxes across the inductors due to the common ground node having $\phi_0 = 0$, $\phi_1 = \Phi_A$ and $\phi_2 = \Phi_B$.
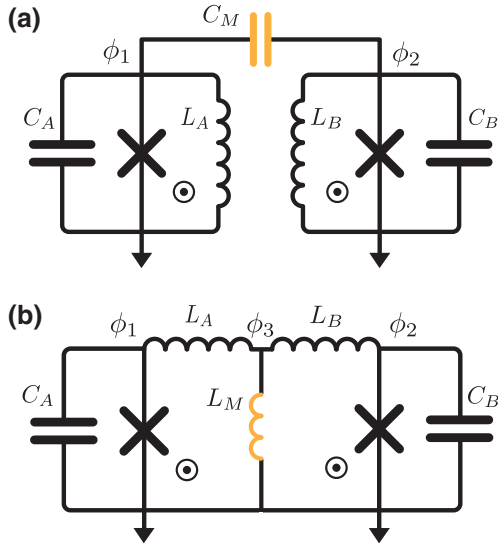
FIG. 15. Circuit schematic for (a) capacitively and (b) inductively coupled fluxoniums. $C_{A,B}$ and $L_{A,B}$ are approximately the shunting capacitance and inductance of the qubits, respectively. The coupling is enabled by the mutual elements C_M and L_M.

The circuit with capacitive coupling can be described by the Lagrangian $\mathcal{L} = \mathcal{T}(\dot{\phi}_1, \dot{\phi}_2) - \mathcal{V}(\phi_1, \phi_2)$,

$$\mathcal{L} = \frac{1}{2}C_A\dot{\phi}_1^2 + \frac{1}{2}C_B\dot{\phi}_2^2 + \frac{1}{2}C_M(\dot{\phi}_1 - \dot{\phi}_2)^2$$
$$- \frac{1}{2L_A}\phi_1^2 - \frac{1}{2L_B}\phi_2^2 + E_{JA}\cos\left[\frac{2\pi}{\Phi_o}(\phi_1 + \Phi_{\text{ext},A})\right]$$
$$+ E_{JB}\cos\left[\frac{2\pi}{\Phi_o}(\phi_2 + \Phi_{\text{ext},B})\right], \tag{D1}$$

with the closure branches containing the Josephson junctions. We note that here, the external fluxes are included in the Josephson energy terms for convenience, and can be switched to the inductive term to conform to the irrotational gauge, as discussed in Appendix B. The charge variables can be found following the relation $q_n \equiv \partial\mathcal{L}/\partial\dot{\phi}_n$. In matrix form, the node charge variables read $\mathbf{q} = \mathbf{C}\dot{\boldsymbol{\phi}}$, or more explicitly,

$$\begin{bmatrix} q_1 \\ q_2 \end{bmatrix} = \begin{bmatrix} C_A + C_M & -C_M \\ -C_M & C_B + C_M \end{bmatrix}\begin{bmatrix} \dot{\phi}_1 \\ \dot{\phi}_2 \end{bmatrix}. \tag{D2}$$

The Hamiltonian can be found via the Legendre transformation, giving

$$\mathcal{H} = \frac{1}{2}\mathbf{q}^T\mathbf{C}^{-1}\mathbf{q} + \mathcal{V}(\phi_1, \phi_2). \tag{D3}$$

The inverse capacitance matrix can be written as

$$\mathbf{C}^{-1} = \frac{1}{\det(\mathbf{C})}\begin{bmatrix} C_B + C_M & C_M \\ C_M & C_A + C_M \end{bmatrix}, \tag{D4}$$

which, in the small coupling limit $C_M \ll C_1, C_2$, gives us the approximate Hamiltonian

$$\mathcal{H} = \frac{1}{2C_A}q_1^2 + \frac{1}{2C_A}q_2^2 + \frac{C_M}{C_AC_B}q_1q_2$$
$$+ \frac{1}{2L_A}\phi_1^2 + \frac{1}{2L_B}\phi_2^2 - E_{JA}\cos\left[\frac{2\pi}{\Phi_o}(\phi_1 + \Phi_{\text{ext},A})\right]$$
$$- E_{JB}\cos\left[\frac{2\pi}{\Phi_o}(\phi_2 + \Phi_{\text{ext},B})\right]. \tag{D5}$$

In the final step, the variables are promoted to quantum operators,

$$q \rightarrow \hat{q} = 2e\hat{n},$$
$$\Phi \rightarrow \hat{\Phi} = \frac{\hbar}{2e}\hat{\varphi}, \tag{D6}$$

to give the Hamiltonian

$$\hat{\mathcal{H}} = \hat{\mathcal{H}}_A + \hat{\mathcal{H}}_B + 4e^2\frac{C_M}{C_AC_B}\hat{n}_A\hat{n}_B. \tag{D7}$$

In the inductive coupling circuit, we define the spanning tree to include the inductors, and the closure branches to go through the Josephson junctions. The Langrangian is then given as

$$\mathcal{L} = \mathcal{T} - \mathcal{V}_L - \mathcal{V}_J = \frac{1}{2}C_A\dot{\phi}_1^2 + \frac{1}{2}C_B\dot{\phi}_2^2$$
$$- \frac{(\phi_1 - \phi_3)^2}{2L_A} - \frac{(\phi_2 - \phi_3)^2}{2L_B} - \frac{\phi_3^2}{2L_M}$$
$$+ E_{JA}\cos\left[\frac{2\pi}{\Phi_o}(\phi_1 + \Phi_{\text{ext},A})\right]$$
$$+ E_{JB}\cos\left[\frac{2\pi}{\Phi_o}(\phi_2 + \Phi_{\text{ext},B})\right]. \tag{D8}$$

Since the circuit in Fig. 15(b) has two active nodes, the number of degrees of freedom in the circuit should be limited to two. This can be readily confirmed by inspecting Lagrange's equation of motion for ϕ_3. To reduce the number of variables in the Lagrangian, a possible approach is to use Kirchhoff's circuit law,

$$\frac{\phi_3}{L_M} = \frac{\phi_1 - \phi_3}{L_A} + \frac{\phi_2 - \phi_3}{L_B}, \tag{D9}$$

which can also be obtained from the equation of motion

$$\frac{d}{dt}\frac{\partial\mathcal{L}}{\partial\dot{\phi}_3} = \frac{\partial\mathcal{L}}{\partial\phi_3} = 0. \tag{D10}$$

Denoting $x_{A,B} = L_M/L_{A,B} \ll 1$ in the small coupling limit, we can express ϕ_3 as a function of ϕ_1 and ϕ_2,

$$\phi_3 = \frac{x_A\phi_1 + x_B\phi_2}{1 + x_A + x_B}. \tag{D11}$$

This allows the inductive potential $\mathcal{V}_L$ to be rewritten as

$$\begin{aligned}
\mathcal{V}_L(\phi_1, \phi_2) &= \frac{1}{1 + x_A + x_B} \\
&\times \left[\frac{(1+x_B)\phi_1^2}{2L_A} + \frac{(1+x_A)\phi_2^2}{2L_B} - \frac{L_M}{L_AL_B}\phi_1\phi_2 \right] \\
&\approx \frac{\phi_1^2}{2L_A} + \frac{\phi_2^2}{2L_B} - \frac{L_M}{L_AL_B}\phi_1\phi_2.
\end{aligned} \tag{D12}$$

The Hamiltonian is then found via Legendre transformation [see Eq. (D3)],

$$\begin{aligned}
\mathcal{H} &= \frac{1}{2C_A}q_1^2 + \frac{1}{2C_A}q_2^2 + \frac{1}{2L_A}\phi_1^2 + \frac{1}{2L_B}\phi_2^2 \\
&\quad - \frac{L_M}{L_AL_B}\phi_1\phi_2 - E_{JA}\cos\left[\frac{2\pi}{\Phi_o}(\phi_1 + \Phi_{\text{ext},A})\right] \\
&\quad - E_{JB}\cos\left[\frac{2\pi}{\Phi_o}(\phi_2 + \Phi_{\text{ext},B})\right].
\end{aligned} \tag{D13}$$

Finally, the circuit degrees of freedom can be promoted to quantum operators. We note that in the small coupling limit, the node fluxes are approximately equal to the branch fluxes across the inductors [cf. Eq. (D12)]. The resulting Hamiltonian is thus given as

$$\hat{\mathcal{H}} = \hat{\mathcal{H}}_A + \hat{\mathcal{H}}_B - \left(\frac{\hbar}{2e}\right)^2 \frac{L_M}{L_AL_B}\hat{\varphi}_A\hat{\varphi}_B. \tag{D14}$$

An inductive energy $E_L = 1$ GHz within the range of our proposed parameters corresponds to an inductance of $L = 163$ nH. Assuming a typical critical current density of 500 nA/μm^2, such an inductor can be constructed using an array of approximately 200 of 0.2×4 μm^2 Josephson junctions. The desired coupling inductance of $L_M = 363$ pH can thus be reached or even surpassed easily if two inductive loops share a single designated mutual junction, the size of which can be varied to control the coupling strength. The same strategy can be used for other types of superinductors made from TiN or grAl.

APPENDIX E: COUPLED SYSTEMS MAPPING

We describe the mapping between an effective model of two coupled spins and a realistic system of two inductively coupled fluxonium qubits as follows. We sweep the coupling constants J_{eff} and J_L in both models up to 10 MHz,
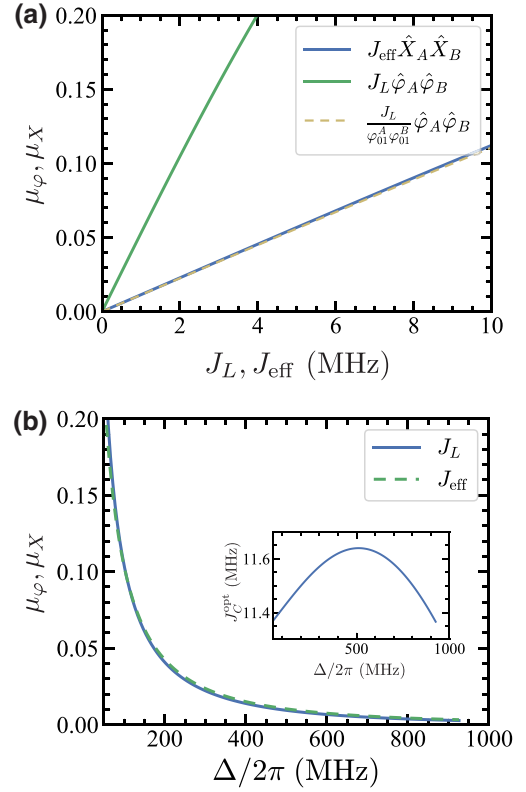

FIG. 16. Mapping between full model and simple model. (a) Level of mixing specified by μ_X, μ_φ with respect to coupling coefficients J_L and J_{eff}. The pair of fluxoniums have a small capacitive coupling to cancel the static ZZ rate. (b) Level of mixing specified by μ for varying qubit-qubit detuning as specified in Table II. (Inset) A small capacitive coupling J_C is optimized at each detuning to cancel static ZZ.

and then compute the respective normalized cross matrix elements μ_X, μ_φ, where

$$\mu_X = \frac{\langle 00|\hat{X}_A \otimes \hat{I}_B|01\rangle}{\langle 00|\hat{X}_A \otimes \hat{I}_B|10\rangle},$$

$$\mu_\varphi = \frac{\langle 00|\hat{\varphi}_A \otimes \hat{I}_B|01\rangle}{\langle 00|\hat{\varphi}_A \otimes \hat{I}_B|10\rangle}.$$

Since $|\varphi_{01}| \approx 2.5$ for the proposed qubit parameters, the coupling term $\hat{\mathcal{H}}_{\text{coupl}}/h = -J_L\hat{\varphi}_A\hat{\varphi}_B$ in the multi-fluxonium system produces more mixing for the same coupling coefficient compared to the coupled-spin model described by the Hamiltonian in Eq. (11) with $\hat{\mathcal{H}}_{\text{coupl}}/h = J_{\text{eff}}\hat{X}_A\hat{X}_B$, as shown in Fig. 16(a). To match the level of mixing amplitude, we lower the coupling J_L by a factor equivalent to $\varphi_{01}^A\varphi_{01}^B$, which produces a close match.

In other words, for linking the mixing level of a specific spin-spin coupling constant J_{eff}, the required inductive coupling constant is $J_L \sim J_{\text{eff}}/\varphi_{01}^A\varphi_{01}^B$. For example, to reach $J_{\text{eff}} = 10$ MHz in the coupled spin model, we need an
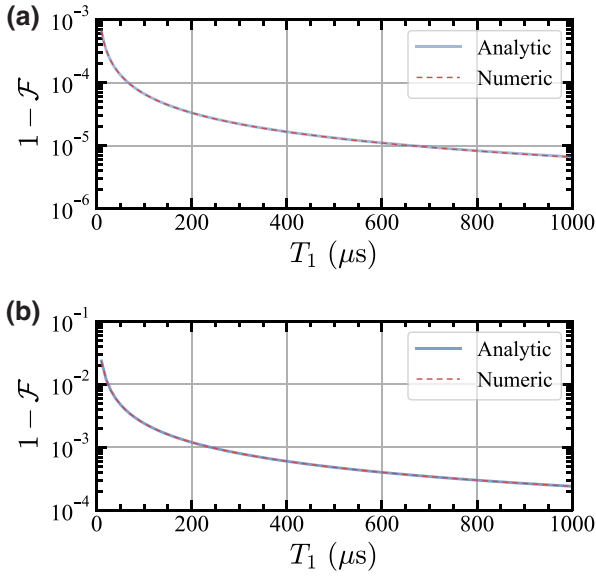
FIG. 17. (a) Single-qubit and (b) two-qubit gate errors due to finite relaxation time T_1. The single-qubit pulse is 20-ns long, and the two-qubit pulses used to implement a CZ gate are 300-ns long.

inductive coupling $J_L \approx 2$ MHz in the coupled fluxonium system.

To explore the consistency of this mapping, we compute μ_φ with $J_L \approx 2$ MHz and μ_X with $J_{\text{eff}} = J_L\varphi_{01}^A\varphi_{01}^B$ for varying qubit parameters as listed in Table II. To tune fluxonium B's frequency, E_L is changed from 0.55 to 1.6 GHz while other parameters are fixed, which corresponds to detuning $\Delta/2\pi$ from 27 to 926 MHz. The results in Fig. 16(b) validate our mapping approach between the complex multilevel coupled fluxonium system and the far simpler coupled spin model. Interestingly, the optimal J_C to completely cancel the static ZZ at each detuning is mostly fixed at approximately 11.5 MHz. This promises negligible quantum crosstalk even when the qubit parameters deviate from targeted values.

APPENDIX F: EXTENDED ERROR BUDGET

1. Decoherence errors

With single- and two-qubit unitary error as low as 10^{-6}, we turn to estimate the gate fidelity limited by decoherence. We assume that the qubit decays at rate Γ_1 and dephases at rate Γ_ϕ, where these rates are related to the relaxation time T_1 and decoherence time T_2 as $\Gamma_1 = (T_1)^{-1}$, $\Gamma_\phi = (T_2)^{-1} - (2T_1)^{-1}$. A Pauli transfer matrix (PTM) of a single-qubit decoherence channel for duration
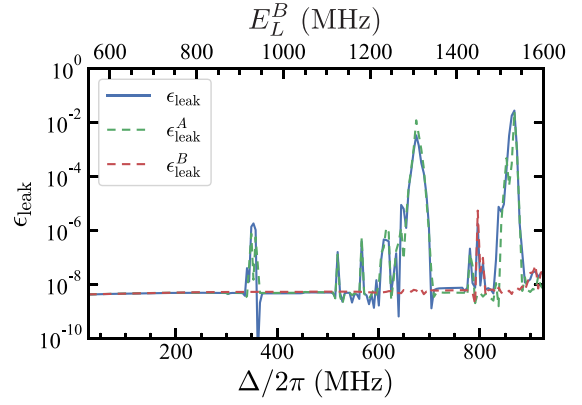

FIG. 18. Leakage to higher states when microwave drives are used to implement a 200-ns CZ gate. The corresponding gate fidelity is plotted in Fig. 7(f).

τ is given as [243]

$$
\mathcal{E}(\tau) = \begin{pmatrix} 1 & 0 & 0 & 0 \\ 0 & e^{-(\Gamma_1/2+\Gamma_\phi)\tau} & 0 & 0 \\ 0 & 0 & e^{-(\Gamma_1/2+\Gamma_\phi)\tau} & 0 \\ 0 & 0 & 0 & e^{-\Gamma_1\tau} \end{pmatrix}.
\tag{F1}
$$

In the absence of non-Markovian errors such as leakage and crosstalks, the PTM of a Pauli-twirled N-qubit channel is simply given by the tensor product $\mathcal{E}^{\otimes N}$. The process fidelity limited by decoherence can thus be written as

$$
\begin{aligned}
\mathcal{F}_p &= \frac{1}{2^N}\text{Tr}[\mathcal{E}^{\otimes N}] \\
&= \frac{1}{2^N}\prod_{i=1}^{N}\left(1 + e^{\Gamma_1^{(i)}\tau} + 2e^{-(\Gamma_1^{(i)}/2+\Gamma_2^{(i)})\tau}\right),
\end{aligned}
\tag{F2}
$$

where $\Gamma_1^{(i)}$ and $\Gamma_\phi^{(i)}$ denote the energy relaxation and pure dephasing rates of qubit i, respectively.

To validate Eq. (F2), we simulate the process fidelity using the Lindblad master equation,

$$
\frac{d\hat{\rho}}{dt} = -i[\hat{\mathcal{H}}_{\text{sys}}, \hat{\rho}] + \sum_\alpha\left(\hat{L}_\alpha\hat{\rho}\hat{L}_\alpha^\dagger - \frac{1}{2}[\hat{L}_\alpha^\dagger\hat{L}_\alpha, \hat{\rho}]\right),
\tag{F3}
$$

where $\hat{\rho}$ is the density matrix of the initial state, $\hat{\mathcal{H}}_{\text{sys}}$ is the Hamiltonian describing the evolution of the system without decoherence, and $\hat{L}_1 = \sqrt{\Gamma_1}|0\rangle\langle 1|$, $\hat{L}_\phi = \sqrt{\Gamma_\phi/2}(|0\rangle\langle 0| - |1\rangle\langle 1|)$ describes the relaxation and pure dephasing processes, respectively. Since only the computational subspace is involved in the proposed gate schemes in this work, we only take into account the decoherence of $|0\rangle$ and $|1\rangle$ states. To construct the process matrix for single- and two-qubit gates, we prepare 2^{2N} initial states,

evolve them under $\hat{\mathcal{H}}_{\text{sys}}$, together with $\hat{L}_1 = \sqrt{\Gamma_1}|0\rangle\langle 1|$. We include only energy relaxation process since it is not clear what currently accounts for pure dephasing time in high-coherence fluxonium, and T_2 is primarily limited by T_1 [53–55].

The dynamical simulation then gives us 2^{2N} output density matrices, which are then analyzed and, together with the input states, converted to a PTM $\mathcal{R}$ using the maximum-likelihood estimation method [76]. The process fidelity is defined as $\mathcal{F}_p = \text{Tr}(\mathcal{R}^{\dagger}_{\text{ideal}}\mathcal{R})/(2^{2N})$, from which we can compute the gate fidelity, $\mathcal{F} = (2^N \times \mathcal{F}_p + 1)/(2^N + 1)$. Figure 17 shows the results from both analytical calculation and numerical simulation for a 20-ns-long single-qubit gate and a 300-ns-long CZ two-qubit gate. The perfect match between the analytical and numerical curves convinces us that Eq. (F2) provides an excellent estimation of decoherence-limited fidelity.

2. CZ gate leakage errors

As discussed in Sec. VI, we observe spikes in the CZ gate errors at certain detuning Δ, corresponding to specific drive frequency ω_d. We attribute this to leakage outside of the computational subspace via high-order processes. To confirm this, we numerically compute the leakage defined as $1 - (P_{|00\rangle} + P_{|01\rangle} + P_{|10\rangle} + P_{|11\rangle})$ using the optimal drive amplitudes given by the Nelder-Mead optimization, as discussed in Sec. VI.

In addition, we simulate the dynamics of each qubit when driven separately. Intuitively, since the drive frequency is far detuned from qubit A, the required drive amplitude for qubit A is much higher, $\epsilon_A \gg \epsilon_B$. Therefore, qubit A is more likely to have leakage. Indeed, this is confirmed by the results shown in Fig. 18.

The most direct mitigation technique is to find a better drive frequency, which would help (i) reduce the required drive amplitude on qubit A to induce the necessary ZZ rate, and (ii) avoid the bad frequency region. Nevertheless, the gate fidelity is still high when this high-order leakage is present, with $\epsilon_{\text{leak}} \approx 10^{-2}$ in the worst case. Another approach is to use a longer pulse, at the cost of having error due to decoherence. Since the coherence time of the qubit can be in the range of milliseconds, a good compromise can be made between the two sources of errors to have good gate fidelity following this approach.

[1] A. W. Harrow and A. Montanaro, Quantum computational supremacy, Nature **549**, 203 (2017).

[2] A. Montanaro, Quantum algorithms: An overview, npj Quantum Inf. **2**, 1 (2016).

[3] J. Biamonte, P. Wittek, N. Pancotti, P. Rebentrost, N. Wiebe, and S. Lloyd, Quantum machine learning, Nature **549**, 195 (2017).

[4] E. Altman, *et al.*, Quantum Simulators: Architectures and Opportunities, PRX Quantum **2**, 017003 (2021).

[5] M. H. Devoret and R. J. Schoelkopf, Superconducting circuits for quantum information: An outlook, Science **339**, 1169 (2013).

[6] F. Arute, K. Arya, R. Babbush, D. Bacon, J. C. Bardin, R. Barends, R. Biswas, S. Boixo, F. G. S. L. Brandao, and D. A. Buell, *et al.*, Quantum supremacy using a programmable superconducting processor, Nature **574**, 505 (2019).

[7] Y. Wu, W.-S. Bao, S. Cao, F. Chen, M.-C. Chen, X. Chen, T.-H. Chung, H. Deng, Y. Du, D. Fan, M. Gong, C. Guo, and C. Guo, *et al.*, Strong Quantum Computational Advantage using a Superconducting Quantum Processor, Phys. Rev. Lett. **127**, 180501 (2021).

[8] N. Ofek, A. Petrenko, R. Heeres, P. Reinhold, Z. Leghtas, B. Vlastakis, Y. Liu, L. Frunzio, S. Girvin, and L. Jiang, *et al.*, Extending the lifetime of a quantum bit with error correction in superconducting circuits, Nature **536**, 441 (2016).

[9] L. Hu, Y. Ma, W. Cai, X. Mu, Y. Xu, W. Wang, Y. Wu, H. Wang, Y. P. Song, C.-L. Zou, S. M. Girvin, L.-M. Duan, and L. Sun, Quantum error correction and universal gate set operation on a binomial bosonic logical qubit, Nat. Phys. **15**, 503 (2019).

[10] P. Campagne-Ibarcq, A. Eickbusch, S. Touzard, E. Zalys-Geller, N. E. Frattini, V. V. Sivak, P. Reinhold, S. Puri, S. Shankar, and R. J. Schoelkopf, *et al.*, Quantum error correction of a qubit encoded in grid states of an oscillator, Nature **584**, 368 (2020).

[11] A. Grimm, N. E. Frattini, S. Puri, S. O. Mundhada, S. Touzard, M. Mirrahimi, S. M. Girvin, S. Shankar, and M. H. Devoret, Stabilization and operation of a Kerr-cat qubit, Nature **584**, 205 (2020).

[12] J. M. Gertler, B. Baker, J. Li, S. Shirol, J. Koch, and C. Wang, Protecting a bosonic qubit with autonomous quantum error correction, Nature **590**, 243 (2021).

[13] C. K. Andersen, A. Remm, S. Lazar, S. Krinner, N. Lacroix, G. J. Norris, M. Gabureac, C. Eichler, and A. Wallraff, Repeated quantum error detection in a surface code, Nat. Phys. **16**, 875 (2020).

[14] J. F. Marques, B. M. Varbanov, M. S. Moreira, H. Ali, N. Muthusubramanian, C. Zachariadis, F. Battistel, M. Beekman, N. Haider, W. Vlothuizen, A. Bruno, B. M. Terhal, and L. DiCarlo, Logical-qubit operations in an error-detecting surface code, Nat. Phys. **18**, 80 (2021).

[15] Google Quantum AI, Exponential suppression of bit or phase errors with cyclic error correction, Nature **595**, 3832021.

[16] S. Krinner, N. Lacroix, A. Remm, A. Di Paolo, E. Genois, C. Leroux, C. Hellings, S. Lazar, F. Swiadek, and J. Herrmann, *et al.*, Realizing repeated quantum error correction in a distance-three surface code, Nature **605**, 669 (2022).

[17] Y. Zhao, Y. Ye, H.-L. Huang, Y. Zhang, D. Wu, H. Guan, Q. Zhu, Z. Wei, T. He, S. Cao, *et al.* Realization of an Error-Correcting Surface Code with Superconducting Qubits, Phys. Rev. Lett. **129**, 030501 (2022).

[18] U. L. Heras, A. Mezzacapo, L. Lamata, S. Filipp, A. Wallraff, and E. Solano, Digital Quantum Simulation of Spin Systems in Superconducting Circuits, Phys. Rev. Lett. **112**, 200501 (2014).

[19] Y. Salathé, M. Mondal, M. Oppliger, J. Heinsoo, P. Kurpiers, A. Potočnik, A. Mezzacapo, U. Las Heras, L. Lamata, E. Solano, S. Filipp, and A. Wallraff, Digital Quantum Simulation of Spin Models with Circuit Quantum Electrodynamics, Phys. Rev. X **5**, 021027 (2015).

[20] R. Barends, A. Shabani, L. Lamata, J. Kelly, A. Mezzacapo, U. Las Heras, R. Babbush, A. G. Fowler, B. Campbell, and Y. Chen, *et al.*, Digitized adiabatic quantum computing with a superconducting circuit, Nature **534**, 222 (2016).

[21] J. I. Colless, V. V. Ramasesh, D. Dahlen, M. S. Blok, M. E. Kimchi-Schwartz, J. R. McClean, J. Carter, W. A. de Jong, and I. Siddiqi, Computation of Molecular Spectra on a Quantum Processor with an Error-Resilient Algorithm, Phys. Rev. X **8**, 011021 (2018).

[22] S. McArdle, X. Yuan, and S. Benjamin, Error-Mitigated Digital Quantum Simulation, Phys. Rev. Lett. **122**, 180501 (2019).

[23] M. S. Blok, V. V. Ramasesh, T. Schuster, K. O'Brien, J. M. Kreikebaum, D. Dahlen, A. Morvan, B. Yoshida, N. Y. Yao, and I. Siddiqi, Quantum Information Scrambling on a Superconducting Qutrit Processor, Phys. Rev. X **11**, 021010 (2021).

[24] F. Arute, K. Arya, R. Babbush, D. Bacon, J. C. Bardin, R. Barends, A. Bengtsson, S. Boixo, M. Broughton, and B. B. Buckley, *et al.*, Observation of separated dynamics of charge and spin in the Fermi-Hubbard model (2020), ArXiv:2010.07965.

[25] C. Neill, T. McCourt, X. Mi, Z. Jiang, M. Y. Niu, W. Mruczkiewicz, I. Aleiner, F. Arute, K. Arya, and J. Atalaya, *et al.*, Accurately computing the electronic properties of a quantum ring, Nature **594**, 508 (2021).

[26] X. Mi, M. Ippoliti, C. Quintana, A. Greene, Z. Chen, J. Gross, F. Arute, K. Arya, J. Atalaya, and R. Babbush, *et al.*, Time-crystalline eigenstate order on a quantum processor, Nature **601**, 531 (2022).

[27] A. Kandala, A. Mezzacapo, K. Temme, M. Takita, M. Brink, J. M. Chow, and J. M. Gambetta, Hardware-efficient variational quantum eigensolver for small molecules and quantum magnets, Nature **549**, 242 (2017).

[28] F. Arute, K. Arya, R. Babbush, D. Bacon, J. C. Bardin, R. Barends, S. Boixo, M. Broughton, and B. B. Buckley, *et al.*, Hartree-Fock on a superconducting qubit quantum computer, Science **369**, 1084 (2020).

[29] J. Preskill, Quantum computing in the NISQ era and beyond, Quantum **2**, 79 (2018).

[30] A. Kandala, K. Temme, A. D. Córcoles, A. Mezzacapo, J. M. Chow, and J. M. Gambetta, Error mitigation extends the computational reach of a noisy quantum processor, Nature **567**, 491 (2019).

[31] A. Hashim, R. K. Naik, A. Morvan, J.-L. Ville, B. Mitchell, J. M. Kreikebaum, M. Davis, E. Smith, C. Iancu, K. P. O'Brien, I. Hincks, J. J. Wallman, J. Emerson, and I. Siddiqi, Randomized Compiling for Scalable Quantum Computing on a Noisy Superconducting Quantum Processor, Phys. Rev. X **11**, 041039 (2021).

[32] A. G. Fowler, M. Mariantoni, J. M. Martinis, and A. N. Cleland, Surface codes: Towards practical large-scale quantum computation, Phys. Rev. A **86**, 032324 (2012).

[33] D. Stilck França and R. García-Patrón, Limitations of optimization algorithms on noisy quantum devices, Nat. Phys. **17**, 1221 (2021).

[34] P. W. Shor, in *Proceedings of 37th Conference on Foundations of Computer Science* (1996), p. 56.

[35] A. Kitaev, Fault-tolerant quantum computation by anyons, Ann. Phys. (N. Y) **303**, 2 (2003).

[36] E. Dennis, A. Kitaev, A. Landahl, and J. Preskill, Topological quantum memory, J. Math. Phys. **43**, 4452 (2002).

[37] E. T. Campbell, B. M. Terhal, and C. Vuillot, Roads towards fault-tolerant universal quantum computation, Nature **549**, 172 (2017).

[38] B. M. Terhal, Quantum error correction for quantum memories, Rev. Mod. Phys. **87**, 307 (2015).

[39] D. Aharonov and M. Ben-Or, in *Proceedings of the Twenty-Ninth Annual ACM Symposium on Theory of Computing*, STOC '97 (Association for Computing Machinery, New York, NY, USA, 1997), p. 176.

[40] E. Knill, R. Laflamme, and W. H. Zurek, Resilient quantum computation: Error models and thresholds, Proc. R. Soc. London Ser. A: Math., Phys. Eng. Sci. **454**, 365 (1998).

[41] J. Preskill, Reliable quantum computers, Proc. R. Soc. London Ser. A: Math., Phys. Eng. Sci. **454**, 385 (1998).

[42] M. Sarovar, T. Proctor, K. Rudinger, K. Young, E. Nielsen, and R. Blume-Kohout, Detecting crosstalk errors in quantum information processors, Quantum **4**, 321 (2020).

[43] M. Brink, J. M. Chow, J. Hertzberg, E. Magesan, and S. Rosenblatt, in *2018 IEEE International Electron Devices Meeting (IEDM)* (2018), p. 6.1.1.

[44] J. B. Hertzberg, E. J. Zhang, S. Rosenblatt, E. Magesan, J. A. Smolin, J.-B. Yau, V. P. Adiga, M. Sandberg, M. Brink, J. M. Chow, and J. S. Orcutt, Laser-annealing Josephson junctions for yielding scaled-up superconducting quantum processors, npj Quantum Inf. **7**, 1 (2021).

[45] B. M. Varbanov, F. Battistel, B. M. Tarasinski, V. P. Ostroukh, T. E. O'Brien, L. DiCarlo, and B. M. Terhal, Leakage detection for a transmon-based surface code, npj Quantum Inf. **6**, 1 (2020).

[46] M. McEwen, *et al.*, Removing leakage-induced correlated errors in superconducting quantum error correction, Nat. Commun. **12**, 1 (2021).

[47] S. B. Bravyi and A. Y. Kitaev, Quantum codes on a lattice with boundary (1998), ArXiv:quant-ph/9811052.

[48] A. G. Fowler, A. M. Stephens, and P. Groszkowski, High-threshold universal quantum computation on the surface code, Phys. Rev. A **80**, 052312 (2009).

[49] D. S. Wang, A. G. Fowler, and L. C. L. Hollenberg, Surface code quantum computing with error rates over 1%, Phys. Rev. A **83**, 020302 (2011).

[50] A. G. Fowler, A. C. Whiteside, and L. C. L. Hollenberg, Towards Practical Classical Processing for the Surface Code, Phys. Rev. Lett. **108**, 180501 (2012).

[51] V. E. Manucharyan, J. Koch, L. I. Glazman, and M. H. Devoret, Fluxonium: Single Cooper-pair circuit free of charge offsets, Science **326**, 113 (2009).

[52] J. Koch, V. Manucharyan, M. H. Devoret, and L. I. Glazman, Charging Effects in the Inductively Shunted Josephson Junction, Phys. Rev. Lett. **103**, 217004 (2009).

[53] L. B. Nguyen, Y.-H. Lin, A. Somoroff, R. Mencia, N. Grabon, and V. E. Manucharyan, High-Coherence Fluxonium Qubit, Phys. Rev. X **9**, 041041 (2019).

[54] H. Zhang, S. Chakram, T. Roy, N. Earnest, Y. Lu, Z. Huang, D. K. Weiss, J. Koch, and D. I. Schuster, Universal Fast-Flux Control of a Coherent, Low-Frequency Qubit, Phys. Rev. X **11**, 011010 (2021).

[55] A. Somoroff, Q. Ficheux, R. A. Mencia, H. Xiong, R. V. Kuzmin, and V. E. Manucharyan, Millisecond coherence in a superconducting qubit (2021), ArXiv:2103.08578.

[56] D. Gusenkova, M. Spiecker, R. Gebauer, M. Willsch, D. Willsch, F. Valenti, N. Karcher, L. Grünhaupt, I. Takmakov, P. Winkel, D. Rieger, A. V. Ustinov, N. Roch, W. Wernsdorfer, K. Michielsen, O. Sander, and I. M. Pop, Quantum Nondemolition Dispersive Readout of a Superconducting Artificial Atom using Large Photon Numbers, Phys. Rev. Appl. **15**, 064030 (2021).

[57] I. Takmakov, P. Winkel, F. Foroughi, L. Planat, D. Gusenkova, M. Spiecker, D. Rieger, L. Grünhaupt, A. Ustinov, W. Wernsdorfer, I. Pop, and N. Roch, Minimizing the Discrimination Time for Quantum States of an Artificial Atom, Phys. Rev. Appl. **15**, 064029 (2021).

[58] R. Gebauer, N. Karcher, D. Gusenkova, M. Spiecker, L. Grünhaupt, I. Takmakov, P. Winkel, L. Planat, N. Roch, W. Wernsdorfer, A. V. Ustinov, M. Weber, M. Weides, I. M. Pop, and O. Sander, State preparation of a fluxonium qubit with feedback from a custom FPGA-based platform, AIP Conf. Proc., 12020.

[59] Q. Ficheux, L. B. Nguyen, A. Somoroff, H. Xiong, K. N. Nesterov, M. G. Vavilov, and V. E. Manucharyan, Fast Logic with Slow Qubits: Microwave-Activated Controlled-Z Gate on Low-Frequency Fluxoniums, Phys. Rev. X **11**, 021026 (2021).

[60] H. Xiong, Q. Ficheux, A. Somoroff, L. B. Nguyen, E. Dogan, D. Rosenstock, C. Wang, K. N. Nesterov, M. G. Vavilov, and V. E. Manucharyan, Arbitrary controlled-phase gate on fluxonium qubits using differential ac Stark shifts, Phys. Rev. Res. **4**, 023040 (2022).

[61] K. N. Nesterov, I. V. Pechenezhskiy, C. Wang, V. E. Manucharyan, and M. G. Vavilov, Microwave-activated controlled-*Z* gate for fixed-frequency fluxonium qubits, Phys. Rev. A **98**, 030301 (2018).

[62] Y. Chen, K. N. Nesterov, V. E. Manucharyan, and M. G. Vavilov, Fast flux entangling gate for fluxonium circuits (2021), ArXiv:2110.00632.

[63] F. Bao, *et al.*, Fluxonium: An Alternative Qubit Platform for High-Fidelity Operations, Phys. Rev. Lett. **129**, 010502 (2022).

[64] I. Moskalenko, I. Besedin, I. Simakov, and A. Ustinov, Tunable coupling scheme for implementing two-qubit gates on fluxonium qubits, Appl. Phys. Lett. **119**, 194001 (2021).

[65] I. N. Moskalenko, I. A. Simakov, N. N. Abramov, D. O. Moskalev, A. A. Pishchimova, N. S. Smirnov, E. V. Zikiy, I. A. Rodionov, and I. S. Besedin, High fidelity two-qubit gates on fluxoniums using a tunable coupler, (2022), arXiv preprint ArXiv:2203.16302.

[66] M. D. Reed, B. R. Johnson, A. A. Houck, L. DiCarlo, J. M. Chow, D. I. Schuster, L. Frunzio, and R. J. Schoelkopf, Fast reset and suppressing spontaneous emission of a superconducting qubit, Appl. Phys. Lett. **96**, 203110 (2010).

[67] E. Jeffrey, D. Sank, J. Y. Mutus, T. C. White, J. Kelly, R. Barends, Y. Chen, Z. Chen, B. Chiaro, A. Dunsworth, A. Megrant, P. J. J. O'Malley, C. Neill, P. Roushan, A. Vainsencher, J. Wenner, A. N. Cleland, and J. M. Martinis, Fast Accurate State Measurement with Superconducting Qubits, Phys. Rev. Lett. **112**, 190504 (2014).

[68] E. A. Sete, J. M. Martinis, and A. N. Korotkov, Quantum theory of a bandpass Purcell filter for qubit readout, Phys. Rev. A **92**, 012325 (2015).

[69] N. T. Bronn, Y. Liu, J. B. Hertzberg, A. D. Córcoles, A. A. Houck, J. M. Gambetta, and J. M. Chow, Broadband filters for abatement of spontaneous emission in circuit quantum electrodynamics, Appl. Phys. Lett. **107**, 172601 (2015).

[70] T. Walter, P. Kurpiers, S. Gasparinetti, P. Magnard, A. Potčnik, Y. Salathé, M. Pechal, M. Mondal, M. Oppliger, C. Eichler, and A. Wallraff, Rapid High-Fidelity Single-Shot Dispersive Readout of Superconducting Qubits, Phys. Rev. Appl. **7**, 054020 (2017).

[71] N. Sundaresan, I. Lauer, E. Pritchett, E. Magesan, P. Jurcevic, and J. M. Gambetta, Reducing Unitary and Spectator Errors in Cross Resonance with Optimized Rotary Echoes, PRX Quantum **1**, 020318 (2020).

[72] A. Winick, J. J. Wallman, and J. Emerson, Simulating and Mitigating Crosstalk, Phys. Rev. Lett. **126**, 230502 (2021).

[73] P. C. de Groot, J. Lisenfeld, R. N. Schouten, S. Ashhab, A. Lupaşcu, C. J. P. M. Harmans, and J. E. Mooij, Selective darkening of degenerate transitions demonstrated with two superconducting quantum bits, Nat. Phys. **6**, 763 (2010).

[74] C. Rigetti and M. Devoret, Fully microwave-tunable universal gates in superconducting qubits with linear couplings and fixed transition frequencies, Phys. Rev. B **81**, 134507 (2010).

[75] J. M. Chow, A. D. Córcoles, J. M. Gambetta, C. Rigetti, B. R. Johnson, J. A. Smolin, J. R. Rozen, G. A. Keefe, M. B. Rothwell, M. B. Ketchen, and M. Steffen, Simple All-Microwave Entangling Gate for Fixed-Frequency Superconducting Qubits, Phys. Rev. Lett. **107**, 080502 (2011).

[76] J. M. Chow, J. M. Gambetta, A. D. Córcoles, S. T. Merkel, J. A. Smolin, C. Rigetti, S. Poletto, G. A. Keefe, M. B. Rothwell, J. R. Rozen, M. B. Ketchen, and M. Steffen, Universal Quantum Gate Set Approaching Fault-Tolerant Thresholds with Superconducting Qubits, Phys. Rev. Lett. **109**, 060501 (2012).

[77] A. Noguchi, A. Osada, S. Masuda, S. Kono, K. Heya, S. P. Wolski, H. Takahashi, T. Sugiyama, D. Lachance-Quirion, and Y. Nakamura, Fast parametric two-qubit gates with suppressed residual interaction using the second-order nonlinearity of a cubic transmon, Phys. Rev. A **102**, 062408 (2020).

[78] B. K. Mitchell, R. K. Naik, A. Morvan, A. Hashim, J. M. Kreikebaum, B. Marinelli, W. Lavrijsen, K. Nowrouzi, D. I. Santiago, and I. Siddiqi, Hardware-Efficient Microwave-Activated Tunable Coupling between Superconducting Qubits, Phys. Rev. Lett. **127**, 200502 (2021).

[79] K. X. Wei, E. Magesan, I. Lauer, S. Srinivasan, D. F. Bogorin, S. Carnevale, G. A. Keefe, Y. Kim, D. Klaus, W. Landers, N. Sundaresan, C. Wang, E. J.

Zhang, M. Steffen, O. E. Dial, D. C. McKay, and A. Kandala, Quantum crosstalk cancellation for fast entangling gates and improved multi-qubit performance (2021), ArXiv:2106.00675.

[80] J. P. Bonilla Ataides, D. K. Tuckett, S. D. Bartlett, S. T. Flammia, and B. J. Brown, The XZZX surface code, Nat. Commun. **12**, 1 (2021).

[81] X. You, J. A. Sauls, and J. Koch, Circuit quantization in the presence of time-dependent external flux, Phys. Rev. B **99**, 174512 (2019).

[82] R.-P. Riwar and D. P. DiVincenzo, Circuit quantization with time-dependent magnetic fields for realistic geometries, npj Quantum Inf. **8**, 1 (2022).

[83] N. A. Masluk, I. M. Pop, A. Kamal, Z. K. Minev, M. H. Devoret, and Microwave characterization of josephson junction arrays, Implementing a Low Loss Superinductance, Phys. Rev. Lett. **109**, 137002 (2012).

[84] A. Shearrow, G. Koolstra, S. J. Whiteley, N. Earnest, P. S. Barry, F. J. Heremans, D. D. Awschalom, E. Shirokoff, and D. I. Schuster, Atomic layer deposition of titanium nitride for quantum circuits, Appl. Phys. Lett. **113**, 212601 (2018).

[85] T. M. Hazard, A. Gyenis, A. Di Paolo, A. T. Asfaw, S. A. Lyon, A. Blais, and A. A. Houck, Nanowire Superinductance Fluxonium Qubit, Phys. Rev. Lett. **122**, 010504 (2019).

[86] D. Niepce, J. Burnett, and J. Bylander, High Kinetic Inductance NbN Nanowire Superinductors, Phys. Rev. Appl. **11**, 044014 (2019).

[87] L. Grünhaupt, N. Maleeva, S. T. Skacel, M. Calvo, F. Levy-Bertrand, A. V. Ustinov, H. Rotzinger, A. Monfardini, G. Catelani, and I. M. Pop, Loss Mechanisms and Quasiparticle Dynamics in Superconducting Microwave Resonators made of Thin-Film Granular Aluminum, Phys. Rev. Lett. **121**, 117001 (2018).

[88] N. Maleeva, L. Grünhaupt, T. Klein, F. Levy-Bertrand, O. Dupre, M. Calvo, F. Valenti, P. Winkel, F. Friedrich, W. Wernsdorfer, A. V. Ustinov, H. Rotzinger, A. Monfardini, M. V. Fistul, and I. M. Pop, Circuit quantum electrodynamics of granular aluminum resonators, Nat. Commun. **9**, 1 (2018).

[89] L. Grünhaupt, M. Spiecker, D. Gusenkova, N. Maleeva, S. T. Skacel, I. Takmakov, F. Valenti, P. Winkel, H. Rotzinger, W. Wernsdorfer, A. V. Ustinov, and I. M. Pop, Granular aluminium as a superconducting material for high-impedance quantum circuits, Nat. Mater. **18**, 816 (2019).

[90] P. Kamenov, W.-S. Lu, K. Kalashnikov, T. DiNapoli, M. T. Bell, and M. E. Gershenson, Granular Aluminum Meandered Superinductors for Quantum Circuits, Phys. Rev. Appl. **13**, 054051 (2020).

[91] M. Peruzzo, A. Trioni, F. Hassani, M. Zemlicka, and J. M. Fink, Surpassing the Resistance Quantum with a Geometric Superinductor, Phys. Rev. Appl. **14**, 044055 (2020).

[92] M. Peruzzo, F. Hassani, G. Szep, A. Trioni, E. Redchenko, M. Žemlička, and J. M. Fink, Geometric Superinductance Qubits: Controlling Phase Delocalization across a Single Josephson Junction, PRX Quantum **2**, 040341 (2021).

[93] Y.-H. Lin, L. B. Nguyen, N. Grabon, J. San Miguel, N. Pankratova, and V. E. Manucharyan, Demonstration of Protection of a Superconducting Qubit from Energy Decay, Phys. Rev. Lett. **120**, 150503 (2018).

[94] I. M. Pop, I. Protopopov, F. Lecocq, Z. Peng, B. Pannetier, O. Buisson, and W. Guichard, Measurement of the effect of quantum phase slips in a Josephson junction chain, Nat. Phys. **6**, 589 (2010).

[95] V. E. Manucharyan, N. A. Masluk, A. Kamal, J. Koch, L. I. Glazman, and M. H. Devoret, Evidence for coherent quantum phase slips across a Josephson junction array, Phys. Rev. B **85**, 024521 (2012).

[96] G. Viola and G. Catelani, Collective modes in the fluxonium qubit, Phys. Rev. B **92**, 224511 (2015).

[97] N. Earnest, S. Chakram, Y. Lu, N. Irons, R. K. Naik, N. Leung, L. Ocola, D. A. Czaplewski, B. Baker, J. Lawrence, J. Koch, and D. I. Schuster, Realization of a Λ System with Metastable States of a Capacitively Shunted Fluxonium, Phys. Rev. Lett. **120**, 150504 (2018).

[98] J. Mooij, T. Orlando, L. Levitov, L. Tian, C. H. Van der Wal, and S. Lloyd, Josephson persistent-current qubit, Science **285**, 1036 (1999).

[99] T. P. Orlando, J. E. Mooij, L. Tian, C. H. van der Wal, L. S. Levitov, S. Lloyd, and J. J. Mazo, Superconducting persistent-current qubit, Phys. Rev. B **60**, 15398 (1999).

[100] J. R. Friedman, V. Patel, W. Chen, S. Tolpygo, and J. E. Lukens, Quantum superposition of distinct macroscopic states, Nature **406**, 43 (2000).

[101] C. H. Van Der Wal, A. Ter Haar, F. Wilhelm, R. Schouten, C. Harmans, T. Orlando, S. Lloyd, and J. Mooij, Quantum superposition of macroscopic persistent-current states, Science **290**, 773 (2000).

[102] I. Chiorescu, Y. Nakamura, C. J. P. M. Harmans, and J. E. Mooij, Coherent quantum dynamics of a superconducting flux qubit, Science **299**, 1869 (2003).

[103] A. Kou, W. C. Smith, U. Vool, R. T. Brierley, H. Meier, L. Frunzio, S. M. Girvin, L. I. Glazman, and M. H. Devoret, Fluxonium-Based Artificial Molecule with a Tunable Magnetic Moment, Phys. Rev. X **7**, 031037 (2017).

[104] L. Glazman and G. Catelani, Bogoliubov quasiparticles in superconducting qubits, SciPost Phys. Lect. Notes (2021).

[105] K. Serniak, M. Hays, G. de Lange, S. Diamond, S. Shankar, L. D. Burkhart, L. Frunzio, M. Houzet, and M. H. Devoret, Hot Nonequilibrium Quasiparticles in Transmon Qubits, Phys. Rev. Lett. **121**, 157701 (2018).

[106] K. Serniak, S. Diamond, M. Hays, V. Fatemi, S. Shankar, L. Frunzio, R. Schoelkopf, and M. Devoret, Direct Dispersive Monitoring of Charge Parity in Offset-Charge-Sensitive Transmons, Phys. Rev. Appl. **12**, 014052 (2019).

[107] M. Houzet, K. Serniak, G. Catelani, M. H. Devoret, and L. I. Glazman, Photon-Assisted Charge-Parity Jumps in a Superconducting Qubit, Phys. Rev. Lett. **123**, 107704 (2019).

[108] S. Diamond, V. Fatemi, M. Hays, H. Nho, P. D. Kurilovich, T. Connolly, V. R. Joshi, K. Serniak, L. Frunzio, L. I. Glazman, and M. H. Devoret, Distinguishing parity-switching mechanisms in a superconducting qubit (2022).

[109] A. P. Vepsäläinen, A. H. Karamlou, J. L. Orrell, A. S. Dogra, B. Loer, F. Vasconcelos, D. K. Kim, A. J. Melville,

B. M. Niedzielski, J. L. Yoder, S. Gustavsson, J. A. Formaggio, B. A. VanDevender, and W. D. Oliver, Impact of ionizing radiation on superconducting qubit coherence, Nature **584**, 551 (2020).

[110] L. Cardani, F. Valenti, N. Casali, G. Catelani, T. Charpentier, M. Clemenza, I. Colantoni, A. Cruciani, G. D'Imperio, and L. Gironi, *et al.*, Reducing the impact of radioactivity on quantum circuits in a deep-underground facility, Nat. Commun. **12**, 1 (2021).

[111] C. Wang, Y. Y. Gao, I. M. Pop, U. Vool, C. Axline, T. Brecht, R. W. Heeres, L. Frunzio, M. H. Devoret, and G. Catelani, *et al.*, Measurement and control of quasiparticle dynamics in a superconducting qubit, Nat. Commun. **5**, 1 (2014).

[112] C. D. Wilen, S. Abdullah, N. A. Kurinsky, C. Stanford, L. Cardani, G. D'Imperio, C. Tomei, L. Faoro, L. B. Ioffe, C. H. Liu, A. Opremcak, B. G. Christensen, J. L. DuBois, and R. McDermott, Correlated charge noise and relaxation errors in superconducting qubits, Nature **594**, 369 (2021).

[113] M. McEwen, L. Faoro, K. Arya, A. Dunsworth, T. Huang, S. Kim, B. Burkett, A. Fowler, F. Arute, and J. C. Bardin, *et al.*, Resolving catastrophic error bursts from cosmic rays in large arrays of superconducting qubits, Nat. Phys. **18**, 107 (2022).

[114] G. Catelani, J. Koch, L. Frunzio, R. J. Schoelkopf, M. H. Devoret, and L. I. Glazman, Quasiparticle Relaxation of Superconducting Qubits in the Presence of Flux, Phys. Rev. Lett. **106**, 077002 (2011).

[115] G. Catelani, R. J. Schoelkopf, M. H. Devoret, and L. I. Glazman, Relaxation and frequency shifts induced by quasiparticles in superconducting qubits, Phys. Rev. B **84**, 064517 (2011).

[116] I. M. Pop, K. Geerlings, G. Catelani, R. J. Schoelkopf, L. I. Glazman, and M. H. Devoret, Coherent suppression of electromagnetic dissipation due to superconducting quasiparticles, Nature **508**, 369 (2014).

[117] U. Vool, I. M. Pop, K. Sliwa, B. Abdo, C. Wang, T. Brecht, Y. Y. Gao, S. Shankar, M. Hatridge, G. Catelani, M. Mirrahimi, L. Frunzio, R. J. Schoelkopf, L. I. Glazman, and M. H. Devoret, Non-Poissonian Quantum Jumps of a Fluxonium Qubit due to Quasiparticle Excitations, Phys. Rev. Lett. **113**, 247001 (2014).

[118] L. B. Nguyen, *Toward the Fluxonium Quantum Processor*, Ph.D. thesis, University of Maryland, College Park (2020).

[119] A. Blais, J. Gambetta, A. Wallraff, D. I. Schuster, S. M. Girvin, M. H. Devoret, and R. J. Schoelkopf, Quantum-information processing with circuit quantum electrodynamics, Phys. Rev. A **75**, 032329 (2007).

[120] A. Blais, A. L. Grimsmo, S. M. Girvin, and A. Wallraff, Circuit quantum electrodynamics, Rev. Mod. Phys. **93**, 025005 (2021).

[121] A. A. Houck, J. A. Schreier, B. R. Johnson, J. M. Chow, J. Koch, J. M. Gambetta, D. I. Schuster, L. Frunzio, M. H. Devoret, S. M. Girvin, and R. J. Schoelkopf, Controlling the Spontaneous Emission of a Superconducting Transmon Qubit, Phys. Rev. Lett. **101**, 080502 (2008).

[122] Y. Chen, D. Sank, P. O'Malley, T. White, R. Barends, B. Chiaro, J. Kelly, E. Lucero, M. Mariantoni, A. Megrant,

C. Neill, A. Vainsencher, J. Wenner, Y. Yin, A. N. Cleland, and J. M. Martinis, Multiplexed dispersive readout of superconducting phase qubits, Appl. Phys. Lett. **101**, 182601 (2012).

[123] J. Heinsoo, C. K. Andersen, A. Remm, S. Krinner, T. Walter, Y. Salathé, S. Gasparinetti, J.-C. Besse, A. Potočnik, A. Wallraff, and C. Eichler, Rapid High-Fidelity Multiplexed Readout of Superconducting Qubits, Phys. Rev. Appl. **10**, 034040 (2018).

[124] J. E. Johnson, C. Macklin, D. H. Slichter, R. Vijay, E. B. Weingarten, J. Clarke, and I. Siddiqi, Heralded State Preparation in a Superconducting Qubit, Phys. Rev. Lett. **109**, 050506 (2012).

[125] D. Ristè, J. G. van Leeuwen, H.-S. Ku, K. W. Lehnert, and L. DiCarlo, Initialization by Measurement of a Superconducting Quantum Bit Circuit, Phys. Rev. Lett. **109**, 050507 (2012).

[126] Y. Salathé, P. Kurpiers, T. Karg, C. Lang, C. K. Andersen, A. Akin, S. Krinner, C. Eichler, and A. Wallraff, Low-Latency Digital Signal Processing for Feedback and Feedforward in Quantum Computing and Communication, Phys. Rev. Appl. **9**, 034011 (2018).

[127] D. Ristè, C. C. Bultink, K. W. Lehnert, and L. DiCarlo, Feedback Control of a Solid-State Qubit using High-Fidelity Projective Measurement, Phys. Rev. Lett. **109**, 240502 (2012).

[128] P. Campagne-Ibarcq, E. Flurin, N. Roch, D. Darson, P. Morfin, M. Mirrahimi, M. H. Devoret, F. Mallet, and B. Huard, Persistent Control of a Superconducting Qubit by Stroboscopic Measurement Feedback, Phys. Rev. X **3**, 021008 (2013).

[129] P. Jurcevic, A. Javadi-Abhari, L. S. Bishop, I. Lauer, D. F. Bogorin, M. Brink, L. Capelluto, O. Günlük, T. Itoko, and N. Kanazawa, *et al.*, Demonstration of quantum volume 64 on a superconducting quantum computing system, Quantum Sci. Technol. **6**, 025020 (2021).

[130] A. Wallraff, D. I. Schuster, A. Blais, L. Frunzio, J. Majer, M. H. Devoret, S. M. Girvin, and R. J. Schoelkopf, Approaching Unit Visibility for Control of a Superconducting Qubit with Dispersive Readout, Phys. Rev. Lett. **95**, 060501 (2005).

[131] G. Zhu, D. G. Ferguson, V. E. Manucharyan, and J. Koch, Circuit QED with fluxonium qubits: Theory of the dispersive regime, Phys. Rev. B **87**, 024510 (2013).

[132] J. Koch, T. M. Yu, J. Gambetta, A. A. Houck, D. I. Schuster, J. Majer, A. Blais, M. H. Devoret, S. M. Girvin, and R. J. Schoelkopf, Charge-insensitive qubit design derived from the Cooper pair box, Phys. Rev. A **76**, 042319 (2007).

[133] D. I. Schuster, A. Wallraff, A. Blais, L. Frunzio, R.-S. Huang, J. Majer, S. M. Girvin, and R. J. Schoelkopf, ac Stark Shift and Dephasing of a Superconducting Qubit Strongly Coupled to a Cavity Field, Phys. Rev. Lett. **94**, 123602 (2005).

[134] W. C. Smith, A. Kou, U. Vool, I. M. Pop, L. Frunzio, R. J. Schoelkopf, and M. H. Devoret, Quantization of inductively shunted superconducting circuits, Phys. Rev. B **94**, 144507 (2016).

[135] F. Yan, D. Campbell, P. Krantz, M. Kjaergaard, D. Kim, J. L. Yoder, D. Hover, A. Sears, A. J. Kerman, T. P.

Orlando, S. Gustavsson, and W. D. Oliver, Distinguishing Coherent and Thermal Photon Noise in a Circuit Quantum Electrodynamical System, Phys. Rev. Lett. **120**, 260504 (2018).

[136] G. Zhang, Y. Liu, J. J. Raftery, and A. A. Houck, Suppression of photon shot noise dephasing in a tunable coupling superconducting qubit, npj Quantum Inf. **3**, 1 (2017).

[137] J.-H. Yeh, J. LeFebvre, S. Premaratne, F. C. Wellstood, and B. S. Palmer, Microwave attenuators for use with quantum devices below 100 mK, J. Appl. Phys. **121**, 224501 (2017).

[138] J.-H. Yeh, Y. Huang, R. Zhang, S. Premaratne, J. LeFebvre, F. C. Wellstood, and B. S. Palmer, Hot electron heatsinks for microwave attenuators below 100 mK, Appl. Phys. Lett. **114**, 152602 (2019).

[139] C. Bauer, R. Freeman, T. Frenkiel, J. Keeler, and A. Shaka, Gaussian pulses, J. Magn. Reson. (1969) **58**, 442 (1984).

[140] M. Steffen, J. M. Martinis, and I. L. Chuang, Accurate control of Josephson phase qubits, Phys. Rev. B **68**, 224518 (2003).

[141] P. Krantz, M. Kjaergaard, F. Yan, T. P. Orlando, S. Gustavsson, and W. D. Oliver, A quantum engineer's guide to superconducting qubits, Appl. Phys. Rev. **6**, 021318 (2019).

[142] D. C. McKay, C. J. Wood, S. Sheldon, J. M. Chow, and J. M. Gambetta, Efficient Z gates for quantum computing, Phys. Rev. A **96**, 022330 (2017).

[143] F. Motzoi, J. M. Gambetta, P. Rebentrost, and F. K. Wilhelm, Simple Pulses for Elimination of Leakage in Weakly Nonlinear Qubits, Phys. Rev. Lett. **103**, 110501 (2009).

[144] J. M. Gambetta, F. Motzoi, S. T. Merkel, and F. K. Wilhelm, Analytic control methods for high-fidelity unitary operations in a weakly nonlinear oscillator, Phys. Rev. A **83**, 012308 (2011).

[145] E. Lucero, J. Kelly, R. C. Bialczak, M. Lenander, M. Mariantoni, M. Neeley, A. D. O'Connell, D. Sank, H. Wang, M. Weides, J. Wenner, T. Yamamoto, A. N. Cleland, and J. M. Martinis, Reduced phase error through optimized control of a superconducting qubit, Phys. Rev. A **82**, 042339 (2010).

[146] J. M. Chow, L. DiCarlo, J. M. Gambetta, F. Motzoi, L. Frunzio, S. M. Girvin, and R. J. Schoelkopf, Optimized driving of superconducting artificial atoms for improved single-qubit gates, Phys. Rev. A **82**, 040305 (2010).

[147] Z. Chen, et al., Measuring and Suppressing Quantum State Leakage in a Superconducting Qubit, Phys. Rev. Lett. **116**, 020501 (2016).

[148] L. H. Pedersen, N. M. Møller, and K. Mølmer, Fidelity of quantum operations, Phys. Lett. A **367**, 47 (2007).

[149] R. Manenti, E. A. Sete, A. Q. Chen, S. Kulshreshtha, J.-H. Yeh, F. Oruc, A. Bestwick, M. Field, K. Jackson, and S. Poletto, Full control of superconducting qubits with combined on-chip microwave and flux lines, Appl. Phys. Lett. **119**, 144001 (2021).

[150] M. Hatridge, R. Vijay, D. H. Slichter, J. Clarke, and I. Siddiqi, Dispersive magnetometry with a quantum limited squid parametric amplifier, Phys. Rev. B **83**, 134501 (2011).

[151] J. Wenner, M. Neeley, R. C. Bialczak, M. Lenander, E. Lucero, A. D. O'Connell, D. Sank, H. Wang, M. Weides, A. N. Cleland, and J. M. Martinis, Wirebond crosstalk and cavity modes in large chip mounts for superconducting qubits, Supercond. Sci. Technol. **24**, 065001 (2011).

[152] S. Huang, B. Lienhard, G. Calusine, A. Vepsäläinen, J. Braumüller, D. K. Kim, A. J. Melville, B. M. Niedzielski, J. L. Yoder, B. Kannan, T. P. Orlando, S. Gustavsson, and W. D. Oliver, Microwave Package Design for Superconducting Quantum Processors, PRX Quantum **2**, 020306 (2021).

[153] M. H. Devoret, et al., Quantum fluctuations in electrical circuits, Les Houches, Session LXIII **7**, 133 (1995).

[154] Y. Chen, et al., Qubit Architecture with High Coherence and Fast Tunable Coupling, Phys. Rev. Lett. **113**, 220502 (2014).

[155] F. Yan, P. Krantz, Y. Sung, M. Kjaergaard, D. L. Campbell, T. P. Orlando, S. Gustavsson, and W. D. Oliver, Tunable Coupling Scheme for Implementing High-Fidelity Two-Qubit Gates, Phys. Rev. Appl. **10**, 054062 (2018).

[156] C. Leroux, A. Di Paolo, and A. Blais, Superconducting Coupler with Exponentially Large On:Off Ratio, Phys. Rev. Appl. **16**, 064062 (2021).

[157] J. Majer, J. M. Chow, J. M. Gambetta, J. Koch, B. R. Johnson, J. A. Schreier, L. Frunzio, D. I. Schuster, A. A. Houck, A. Wallraff, A. Blais, M. H. Devoret, S. M. Girvin, and R. J. Schoelkopf, Coupling superconducting qubits via a cavity bus, Nature **449**, 443 (2007).

[158] S. Poletto, J. M. Gambetta, S. T. Merkel, J. A. Smolin, J. M. Chow, A. D. Córcoles, G. A. Keefe, M. B. Rothwell, J. R. Rozen, D. W. Abraham, C. Rigetti, and M. Steffen, Entanglement of Two Superconducting Qubits in a Waveguide Cavity via Monochromatic Two-Photon Excitation, Phys. Rev. Lett. **109**, 240505 (2012).

[159] K. N. Nesterov, Q. Ficheux, V. E. Manucharyan, and M. G. Vavilov, Proposal for Entangling Gates on Fluxonium Qubits via a Two-Photon Transition, PRX Quantum **2**, 020345 (2021).

[160] G. S. Paraoanu, Microwave-induced coupling of superconducting qubits, Phys. Rev. B **74**, 140504 (2006).

[161] A. D. Córcoles, J. M. Gambetta, J. M. Chow, J. A. Smolin, M. Ware, J. Strand, B. L. T. Plourde, and M. Steffen, Process verification of two-qubit quantum gates by randomized benchmarking, Phys. Rev. A **87**, 030301 (2013).

[162] S. Sheldon, E. Magesan, J. M. Chow, and J. M. Gambetta, Procedure for systematically tuning up cross-talk in the cross-resonance gate, Phys. Rev. A **93**, 060302 (2016).

[163] P. C. de Groot, S. Ashhab, A. Lupaşcu, L. DiCarlo, F. Nori, C. J. P. M. Harmans, and J. E. Mooij, Selective darkening of degenerate transitions for implementing quantum controlled-NOT gates, New J. Phys. **14**, 073038 (2012).

[164] V. Tripathi, M. Khezri, and A. N. Korotkov, Operation and intrinsic error budget of a two-qubit cross-resonance gate, Phys. Rev. A **100**, 012301 (2019).

[165] E. Magesan and J. M. Gambetta, Effective hamiltonian models of the cross-resonance gate, Phys. Rev. A **101**, 052308 (2020).

[166] M. Malekakhlagh, E. Magesan, and D. C. McKay, First-principles analysis of cross-resonance gate operation, Phys. Rev. A **102**, 042605 (2020).

[167] S. Kirchhoff, T. Keßler, P. J. Liebermann, E. Assémat, S. Machnes, F. Motzoi, and F. K. Wilhelm, Optimized cross-resonance gate for coupled transmon systems, Phys. Rev. A **97**, 042348 (2018).

[168] Y. Kim, A. Morvan, L. B. Nguyen, R. K. Naik, C. Jünger, L. Chen, J. M. Kreikebaum, D. I. Santiago, and I. Siddiqi, High-fidelity three-qubit iToffoli gate for fixed-frequency superconducting qubits, Nat. Phys. **18**, 783 (2022).

[169] J. M. Chow, J. M. Gambetta, A. W. Cross, S. T. Merkel, C. Rigetti, and M. Steffen, Microwave-activated conditional-phase gate for superconducting qubits, New J. Phys. **15**, 115012 (2013).

[170] S. Krinner, P. Kurpiers, B. Royer, P. Magnard, I. Tsitsilin, J.-C. Besse, A. Remm, A. Blais, and A. Wallraff, Demonstration of an All-Microwave Controlled-Phase Gate between Far-Detuned Qubits, Phys. Rev. Appl. **14**, 044039 (2020).

[171] H. Paik, A. Mezzacapo, M. Sandberg, D. T. McClure, B. Abdo, A. D. Córcoles, O. Dial, D. F. Bogorin, B. L. T. Plourde, M. Steffen, A. W. Cross, J. M. Gambetta, and J. M. Chow, Experimental Demonstration of a Resonator-Induced Phase Gate in a Multiqubit Circuit-QED System, Phys. Rev. Lett. **117**, 250502 (2016).

[172] A. Schneider, J. Braumüller, L. Guo, P. Stehle, H. Rotzinger, M. Marthaler, A. V. Ustinov, and M. Weides, Local sensing with the multilevel ac Stark effect, Phys. Rev. A **97**, 062334 (2018).

[173] M. Carroll, S. Rosenblatt, P. Jurcevic, I. Lauer, and A. Kandala, Dynamics of superconducting qubit relaxation times (2021), ArXiv:2105.15201.

[174] Z. Huang, P. S. Mundada, A. Gyenis, D. I. Schuster, A. A. Houck, and J. Koch, Engineering Dynamical Sweet Spots to Protect Qubits from $1/f$ Noise, Phys. Rev. Appl. **15**, 034065 (2021).

[175] J. M. Kreikebaum, K. P. O'Brien, A. Morvan, and I. Siddiqi, Improving wafer-scale Josephson junction resistance variation in superconducting quantum coherent circuits, Supercond. Sci. Technol. **33**, 06LT02 (2020).

[176] C. Chamberland, G. Zhu, T. J. Yoder, J. B. Hertzberg, and A. W. Cross, Topological and Subsystem Codes on Low-Degree Graphs with Flag Qubits, Phys. Rev. X **10**, 011022 (2020).

[177] A. Morvan, L. Chen, J. M. Larson, D. I. Santiago, and I. Siddiqi, Optimizing frequency allocation for fixed-frequency superconducting quantum processors, Phys. Rev. Res. **4**, 023079 (2022).

[178] J. Kelly, *et al.*, Optimal Quantum Control using Randomized Benchmarking, Phys. Rev. Lett. **112**, 240504 (2014).

[179] Y. Sung, L. Ding, J. Braumüller, A. Vepsäläinen, B. Kannan, M. Kjaergaard, A. Greene, G. O. Samach, C. McNally, D. Kim, A. Melville, B. M. Niedzielski, M. E. Schwartz, J. L. Yoder, T. P. Orlando, S. Gustavsson, and W. D. Oliver, Realization of High-Fidelity CZ and ZZ-free iSWAP Gates with a Tunable Coupler, Phys. Rev. X **11**, 021058 (2021).

[180] W. E. Hart, J.-P. Watson, and D. L. Woodruff, Pyomo: Modeling and solving mathematical programs in python, Math. Prog. Comput. **3**, 219 (2011).

[181] M. L. Bynum, G. A. Hackebeil, W. E. Hart, C. D. Laird, B. L. Nicholson, J. D. Siirola, J.-P. Watson, and D. L. Woodruff, *Pyomo–Optimization Modeling in Python* Vol. 67 (Springer Science & Business Media, Cham, Switzerland, 2021), 3rd ed.

[182] E. J. Zhang, S. Srinivasan, N. Sundaresan, D. F. Bogorin, Y. Martin, J. B. Hertzberg, J. Timmerwilke, E. J. Pritchett, J.-B. Yau, and C. Wang, *et al.*, High-performance superconducting quantum processors via laser annealing of transmon qubits, Sci. Adv. **8**, eabi6690 (2022).

[183] J. Edmonds, Paths, trees, and flowers, Can. J. Math. **17**, 449 (1965).

[184] V. Kolmogorov, Blossom V: A new implementation of a minimum cost perfect matching algorithm, Math. Prog. Comput. **1**, 43 (2009).

[185] F. Lecocq, I. M. Pop, Z. Peng, I. Matei, T. Crozes, T. Fournier, C. Naud, W. Guichard, and O. Buisson, Junction fabrication by shadow evaporation without a suspended bridge, Nanotechnology **22**, 315302 (2011).

[186] A. Osman, J. Simon, A. Bengtsson, S. Kosen, P. Krantz, D. P. Lozano, M. Scigliuzzo, P. Delsing, J. Bylander, and A. Fadavi Roudsari, Simplified Josephson-junction fabrication process for reproducibly high-performance superconducting qubits, Appl. Phys. Lett. **118**, 064002 (2021).

[187] W. C. Smith, M. Villiers, A. Marquet, J. Palomo, M. R. Delbecq, T. Kontos, P. Campagne-Ibarcq, B. Douçot, and Z. Leghtas, Magnifying Quantum Phase Fluctuations with Cooper-Pair Pairing, Phys. Rev. X **12**, 021002 (2022).

[188] A. Gyenis, P. S. Mundada, A. Di Paolo, T. M. Hazard, X. You, D. I. Schuster, J. Koch, A. Blais, and A. A. Houck, Experimental Realization of a Protected Superconducting Circuit Derived from the 0–π Qubit, PRX Quantum **2**, 010339 (2021).

[189] K. Kalashnikov, W. T. Hsieh, W. Zhang, W.-S. Lu, P. Kamenov, A. Di Paolo, A. Blais, M. E. Gershenson, and M. Bell, Bifluxon: Fluxon-Parity-Protected Superconducting Qubit, PRX Quantum **1**, 010307 (2020).

[190] R. Kuzmin, R. Mencia, N. Grabon, N. Mehta, Y.-H. Lin, and V. E. Manucharyan, Quantum electrodynamics of a superconductor–insulator phase transition, Nat. Phys. **15**, 930 (2019).

[191] F. Valenti, F. Henriques, G. Catelani, N. Maleeva, L. Grünhaupt, U. von Lüpke, S. T. Skacel, P. Winkel, A. Bilmes, A. V. Ustinov, J. Goupy, M. Calvo, A. Benoît, F. Levy-Bertrand, A. Monfardini, and I. M. Pop, Interplay between Kinetic Inductance, Nonlinearity, and Quasiparticle Dynamics in Granular Aluminum Microwave Kinetic Inductance Detectors, Phys. Rev. Appl. **11**, 054087 (2019).

[192] D. Gusenkova, F. Valenti, M. Spiecker, S. Günzler, P. Paluch, D. Rieger, L.-M. Pioraş-Ţimbolmaş, L. P. Zârbo, N. Casali, I. Colantoni, A. Cruciani, S. Pirro, L. Cardani, A. Petrescu, W. Wernsdorfer, P. Winkel, and I. M. Pop, Operating in a deep underground facility improves the locking of gradiometric fluxonium qubits at the sweet spots, Appl. Phys. Lett. **120**, 054001 (2022).

[193] M. Vahidpour, W. O'Brien, J. T. Whyland, J. Angeles, J. Marshall, D. Scarabelli, G. Crossman, K. Yadav, Y. Mohan, C. Bui, V. Rawat, R. Renzas, N. Vodrahalli,

A. Bestwick, and C. Rigetti, Superconducting through-silicon vias for quantum integrated circuits (2017), ArXiv:1708.02226.

[194] D. Rosenberg, D. Kim, R. Das, D. Yost, S. Gustavsson, D. Hover, P. Krantz, A. Melville, L. Racz, G. O. Samach, S. J. Weber, F. Yan, J. L. Yoder, A. J. Kerman, and W. D. Oliver, 3D integrated superconducting qubits, npj Quantum Inf. **3,** 1 (2017).

[195] C. Conner, A. Bienfait, H.-S. Chang, M.-H. Chou, É. Dumur, J. Grebel, G. Peairs, R. Povey, H. Yan, and Y. Zhong, *et al.*, Superconducting qubits in a flip-chip architecture, Appl. Phys. Lett. **118,** 232602 (2021).

[196] S. Kosen, *et al.*, Building blocks of a flip-chip integrated superconducting quantum processor, Quantum Sci. Technol. **7,** 035018 (2022).

[197] R. Shillito, A. Petrescu, J. Cohen, J. Beall, M. Hauru, M. Ganahl, A. G. M. Lewis, G. Vidal, and A. Blais, Dynamics of transmon ionization, https://arxiv.org/abs/2203.11235 (2022).

[198] E. Magesan, J. M. Gambetta, A. D. Córcoles, and J. M. Chow, Machine Learning for Discriminating Quantum Measurement Trajectories and Improving Readout, Phys. Rev. Lett. **114,** 200501 (2015).

[199] B. Lienhard, A. Vepsäläinen, L. C. Govia, C. R. Hoffer, J. Y. Qiu, D. Ristè, M. Ware, D. Kim, R. Winik, A. Melville, B. Niedzielski, J. Yoder, G. J. Ribeill, T. A. Ohki, H. K. Krovi, T. P. Orlando, S. Gustavsson, and W. D. Oliver, Deep-Neural-Network Discrimination of Multiplexed Superconducting-Qubit States, Phys. Rev. Appl. **17,** 014024 (2022).

[200] D. F. Wise, J. J. Morton, and S. Dhomkar, Using Deep Learning to Understand and Mitigate the Qubit Noise Environment, PRX Quantum **2,** 010316 (2021).

[201] M. Spiecker, P. Paluch, N. Drucker, S. Matityahu, D. Gusenkova, N. Gosling, S. Günzler, D. Rieger, I. Takmakov, F. Valenti, P. Winkel, R. Gebauer, O. Sander, G. Catelani, A. Shnirman, A. V. Ustinov, W. Wernsdorfer, Y. Cohen, and I. M. Pop, A quantum Szilard engine for two-level systems coupled to a qubit (2022).

[202] K. W. Murch, U. Vool, D. Zhou, S. J. Weber, S. M. Girvin, and I. Siddiqi, Cavity-Assisted Quantum Bath Engineering, Phys. Rev. Lett. **109,** 183602 (2012).

[203] P. Magnard, P. Kurpiers, B. Royer, T. Walter, J.-C. Besse, S. Gasparinetti, M. Pechal, J. Heinsoo, S. Storz, A. Blais, and A. Wallraff, Fast and Unconditional All-Microwave Reset of a Superconducting Qubit, Phys. Rev. Lett. **121,** 060502 (2018).

[204] K. N. Nesterov, C. Wang, V. E. Manucharyan, and M. G. Vavilov, Controlled-NOT gates for fluxonium qubits via selective darkening of transitions (2022), ArXiv:2202.04583.

[205] S. Kono, K. Koshino, D. Lachance-Quirion, A. F. van Loo, Y. Tabuchi, A. Noguchi, and Y. Nakamura, Breaking the trade-off between fast control and long lifetime of a superconducting qubit, Nat. Commun. **11,** 1 (2020).

[206] B. Abdo, M. Brink, and J. M. Chow, Gyrator Operation using Josephson Mixers, Phys. Rev. Appl. **8,** 034009 (2017).

[207] C. Müller, S. Guan, N. Vogt, J. H. Cole, and T. M. Stace, Passive On-Chip Superconducting Circulator using a Ring of Tunnel Junctions, Phys. Rev. Lett. **120,** 213602 (2018).

[208] A. Rosario Hamann, C. Müller, M. Jerger, M. Zanner, J. Combes, M. Pletyukhov, M. Weides, T. M. Stace, and A. Fedorov, Nonreciprocity Realized with Quantum Nonlinearity, Phys. Rev. Lett. **121,** 123601 (2018).

[209] D. T. Le, C. Müller, R. Navarathna, A. Fedorov, and T. M. Stace, Operating a passive on-chip superconducting circulator: Device control and quasiparticle effects, Phys. Rev. Res. **3,** 043211 (2021).

[210] M. W. Johnson, M. H. Amin, S. Gildert, T. Lanting, F. Hamze, N. Dickson, R. Harris, A. J. Berkley, J. Johansson, and P. Bunyk, *et al.*, Quantum annealing with manufactured spins, Nature **473,** 194 (2011).

[211] A. Niskanen, K. Harrabi, F. Yoshihara, Y. Nakamura, S. Lloyd, and J. S. Tsai, Quantum coherent tunable coupling of superconducting qubits, Science **316,** 723 (2007).

[212] I. Siddiqi, Engineering high-coherence superconducting qubits, Nat. Rev. Mater. **6,** 875 (2021).

[213] R. Gordon, C. Murray, C. Kurter, M. Sandberg, S. Hall, K. Balakrishnan, R. Shelby, B. Wacaser, A. Stabile, and J. Sleight, *et al.*, Environmental radiation impact on lifetimes and quasiparticle tunneling rates of fixed-frequency transmon qubits, Appl. Phys. Lett. **120,** 074002 (2022).

[214] I. Nsanzineza and B. L. T. Plourde, Trapping a Single Vortex and Reducing Quasiparticles in a Superconducting Resonator, Phys. Rev. Lett. **113,** 117002 (2014).

[215] F. Henriques, F. Valenti, T. Charpentier, M. Lagoin, C. Gouriou, M. Martínez, L. Cardani, M. Vignati, L. Grünhaupt, and D. Gusenkova, *et al.*, Phonon traps reduce the quasiparticle density in superconducting circuits, Appl. Phys. Lett. **115,** 212601 (2019).

[216] K. Karatsu, A. Endo, J. Bueno, P. De Visser, R. Barends, D. Thoen, V. Murugesan, N. Tomita, and J. Baselmans, Mitigation of cosmic ray effect on microwave kinetic inductance detector arrays, Appl. Phys. Lett. **114,** 032601 (2019).

[217] C. Kurter, C. Murray, R. Gordon, B. Wymore, M. Sandberg, R. Shelby, A. Eddins, V. Adiga, A. Finck, and E. Rivera, *et al.*, Quasiparticle tunneling as a probe of Josephson junction barrier and capacitor material in superconducting qubits, npj Quantum Inf. **8,** 1 (2022).

[218] S. Gustavsson, F. Yan, G. Catelani, J. Bylander, A. Kamal, J. Birenbaum, D. Hover, D. Rosenberg, G. Samach, and A. P. Sears, *et al.*, Suppressing relaxation in superconducting qubits by quasiparticle pumping, Science **354,** 1573 (2016).

[219] E. T. Mannila, P. Samuelsson, S. Simbierowicz, J. Peltonen, V. Vesterinen, L. Grönberg, J. Hassel, V. F. Maisi, and J. Pekola, A superconductor free of quasiparticles for seconds, Nat. Phys., 12021.

[220] N. Khaneja, T. Reiss, C. Kehlet, T. Schulte-Herbrüggen, and S. J. Glaser, Optimal control of coupled spin dynamics, design of nmr pulse sequences by gradient ascent algorithms, J. Magn. Reson. **172,** 296 (2005).

[221] P. De Fouquieres, S. Schirmer, S. Glaser, and I. Kuprov, Second order gradient ascent pulse engineering, J. Magn. Reson. **212,** 412 (2011).

[222] J. H. Shirley, Solution of the Schrödinger equation with a Hamiltonian periodic in time, Phys. Rev. **138,** B979 (1965).

[223] C. Weitenberg and J. Simonet, Tailoring quantum gases by Floquet engineering, Nat. Phys. **17**, 1342 (2021).

[224] I. D. Kivlichan, J. McClean, N. Wiebe, C. Gidney, A. Aspuru-Guzik, G. K.-L. Chan, and R. Babbush, Quantum Simulation of Electronic Structure with Linear Depth and Connectivity, Phys. Rev. Lett. **120**, 110501 (2018).

[225] C. Yan, J. Hassel, V. Vesterinen, J. Zhang, J. Ikonen, L. Grönberg, J. Goetz, and M. Möttönen, A low-noise on-chip coherent microwave source, Nat. Electron. **4**, 885 (2021).

[226] G. White, F. Pollock, L. Hollenberg, K. Modi, and C. Hill, Non-Markovian Quantum Process Tomography, PRX Quantum **3**, 020344 (2022).

[227] R. Blume-Kohout, J. K. Gamble, E. Nielsen, K. Rudinger, J. Mizrahi, K. Fortier, and P. Maunz, Demonstration of qubit operations below a rigorous fault tolerance threshold with gate set tomography, Nat. Commun. **8**, 1 (2017).

[228] R. Kueng, D. M. Long, A. C. Doherty, and S. T. Flammia, Comparing Experiments to the Fault-Tolerance Threshold, Phys. Rev. Lett. **117**, 170502 (2016).

[229] L. B. Ioffe and M. V. Feigel'man, Possible realization of an ideal quantum computer in Josephson junction array, Phys. Rev. B **66**, 224503 (2002).

[230] B. Douçot, M. V. Feigel'man, and L. B. Ioffe, Topological Order in the Insulating Josephson Junction Array, Phys. Rev. Lett. **90**, 107003 (2003).

[231] S. Gladchenko, D. Olaya, E. Dupont-Ferrier, B. Douçot, L. B. Ioffe, and M. E. Gershenson, Superconducting nanocircuits for topologically protected qubits, Nat. Phys. **5**, 48 (2008).

[232] M. T. Bell, J. Paramanandam, L. B. Ioffe, and M. E. Gershenson, Protected Josephson Rhombus Chains, Phys. Rev. Lett. **112**, 167001 (2014).

[233] W. C. Smith, A. Kou, X. Xiao, U. Vool, and M. H. Devoret, Superconducting circuit protected by two-Cooper-pair tunneling, npj Quantum Inf. **6**, 1 (2020).

[234] P. Brooks, A. Kitaev, and J. Preskill, Protected gates for superconducting qubits, Phys. Rev. A **87**, 052306 (2013).

[235] J. M. Dempster, B. Fu, D. G. Ferguson, D. I. Schuster, and J. Koch, Understanding degenerate ground states of a protected quantum circuit in the presence of disorder, Phys. Rev. B **90**, 094518 (2014).

[236] P. Groszkowski, A. D. Paolo, A. L. Grimsmo, A. Blais, D. I. Schuster, A. A. Houck, and J. Koch, Coherence properties of the 0–π qubit, New J. Phys. **20**, 043053 (2018).

[237] A. D. Paolo, A. L. Grimsmo, P. Groszkowski, J. Koch, and A. Blais, Control and coherence time enhancement of the 0–π qubit, New J. Phys. **21**, 043002 (2019).

[238] J. Johansson, P. Nation, F. Nori, QuTiP: An open-source python framework for the dynamics of open quantum systems, Comput. Phys. Commun. **183**, 1760 (2012).

[239] J. Johansson, P. Nation, F. Nori, QuTiP 2: A python framework for the dynamics of open quantum systems, Comput. Phys. Commun. **184**, 1234 (2013).

[240] B. Li, S. Ahmed, S. Saraogi, N. Lambert, F. Nori, A. Pitchford, and N. Shammah, Pulse-level noisy quantum circuits with QuTiP, Quantum **6**, 630 (2022).

[241] C. Rigetti, J. M. Gambetta, S. Poletto, B. L. T. Plourde, J. M. Chow, A. D. Córcoles, J. A. Smolin, S. T. Merkel, J. R. Rozen, G. A. Keefe, M. B. Rothwell, M. B. Ketchen, and M. Steffen, Superconducting qubit in a waveguide cavity with a coherence time approaching 0.1 ms, Phys. Rev. B **86**, 100506 (2012).

[242] S. Rasmussen, K. Christensen, S. Pedersen, L. Kristensen, T. Bækkegaard, N. Loft, and N. Zinner, Superconducting Circuit Companion—An Introduction with Worked Examples, PRX Quantum **2**, 040204 (2021).

[243] H. Dawkins, J. Wallman, and J. Emerson, Combining T_1 and T_2 estimation with randomized benchmarking and bounding the diamond distance, Phys. Rev. A **102**, 022220 (2020).